

**NAVAL POSTGRADUATE SCHOOL
MONTEREY, CALIFORNIA**



THESIS

19971009 018

DTIC QUALITY INSPECTED 2

**CHARACTERIZATION OF OSCR HF RADAR DATA
IN MONTEREY BAY**

by

Kimberley F. Boyer

March, 1997

Thesis Advisor:

Jeffrey D. Paduan

Second Reader:

Leslie K. Rosenfeld

Approved for public release; distribution is unlimited.

REPORT DOCUMENTATION PAGE

Form Approved
OMB No. 0704-0188

Public reporting burden for this collection of information is estimated to average 1 hour per response, including the time for reviewing instruction, searching existing data sources, gathering and maintaining the data needed, and completing and reviewing the collection of information. Send comments regarding this burden estimate or any other aspect of this collection of information, including suggestions for reducing this burden, to Washington headquarters Services, Directorate for Information Operations and Reports, 1215 Jefferson Davis Highway, Suite 1204, Arlington, VA 22202-4302, and to the Office of Management and Budget, Paperwork Reduction Project (0704-0188) Washington DC 20503.

1. AGENCY USE ONLY (Leave blank)		2. REPORT DATE March 1997	3. REPORT TYPE AND DATES COVERED Master's Thesis
4. TITLE AND SUBTITLE Characterization of OSCAR HF Radar Data in Monterey Bay			5. FUNDING NUMBERS
6. AUTHOR(s) Kimberley Frances Boyer			
7. PERFORMING ORGANIZATION NAME AND ADDRESS Naval Postgraduate School, Monterey CA 93943-5000			8. PERFORMING ORGANIZATION REPORT NUMBER
9. SPONSORING/MONITORING AGENCY NAME(S) AND ADDRESS(ES)			10. SPONSORING/MONITORING AGENCY REPORT NUMBER
11. SUPPLEMENTARY NOTES The views expressed in this thesis are those of the author and do not reflect the official policy or position of the Department of Defense or the U.S. Government.			
12a. DISTRIBUTION/AVAILABILITY STATEMENT Approved for public release; distribution is unlimited.			12b. DISTRIBUTION CODE
13. ABSTRACT(maximum 200 words) A 53-hour long record of surface current data from the OSCAR HF radar system was gathered over Monterey Bay on 6-8 May, 1995. In this study, OSCAR data is evaluated with regard to semi-diurnal (M2) and diurnal (K1) tidal period fluctuations, the seabreeze, seabreeze influenced flow, and both standard and canonical-day mean flow patterns. The OSCAR data is considered on its own and in comparison to similar data types previously gathered by CODAR, a previously established Monterey Bay HF radar system. Two of three CODAR sites were co-located with the two OSCAR sites. Internal wave influence is observed in the M2 tidal constituent analysis and the seabreeze greatly influences fluctuations of the K1 tidal period. Results from analysis of OSCAR data replicated or reinforced data and results from the CODAR system. Initial OSCAR data appears not to have been significantly affected by possible distortion of the phased-array beam patterns. However, contamination of OSCAR returns by simultaneous activation of the CODAR systems is apparent in the data.			
14. SUBJECT TERMS OSCAR, CODAR, SeaSonde, Remote Sensing, HF Radar, Monterey Bay, Tides, Surface Currents, Internal Waves, Sea Breeze			15. NUMBER OF PAGES 105
			16. PRICE CODE
17. SECURITY CLASSIFICATION OF REPORT Unclassified	18. SECURITY CLASSIFICATION OF THIS PAGE Unclassified	19. SECURITY CLASSIFICATION OF ABSTRACT Unclassified	20. LIMITATION OF ABSTRACT UL

NSN 7540-01-280-5500

Standard Form 298 (Rev. 2-89)
Prescribed by ANSI Std. Z39-18 298-102

Approved for public release; distribution is unlimited.

**CHARACTERIZATION OF OSCR HF RADAR DATA
IN MONTEREY BAY**

Kimberley F. Boyer
Lieutenant, United States Navy
B.S., United States Naval Academy, 1988

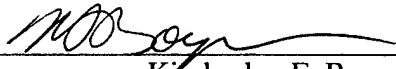
Submitted in partial fulfillment of the
requirements for the degree of

**MASTER OF SCIENCE IN METEOROLOGY AND PHYSICAL
OCEANOGRAPHY**

from the

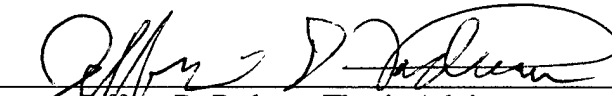
**NAVAL POSTGRADUATE SCHOOL
March 1997**

Author:

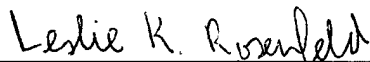


Kimberley F. Boyer

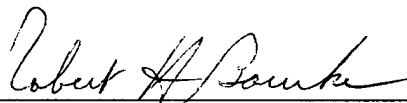
Approved by:



Jeffrey D. Paduan, Thesis Advisor



Leslie K. Rosenfeld, Second Reader



Robert H. Bourke, Chairman,
Department of Oceanography

#

ABSTRACT

A 53-hour long record of surface current data from the OSCAR HF radar system was gathered over Monterey Bay on 6-8 May, 1995. In this study, OSCAR data is evaluated with regard to semidiurnal (M2) and diurnal (K1) tidal period fluctuations, the seabreeze, seabreeze influenced flow, and both standard and canonical-day mean flow patterns. The OSCAR data is considered on its own and in comparison to similar data types previously gathered by CODAR, a previously established Monterey Bay HF radar system. Two of three CODAR sites were co-located with the two OSCAR sites.

Internal wave influence is observed in the M2 tidal constituent analysis and the seabreeze greatly influences fluctuations of the K1 tidal period. Results from analysis of OSCAR data replicated or reinforced data and results from the CODAR system. Initial OSCAR data appears not to have been significantly affected by possible distortion of the phased-array beam patterns. However, contamination of OSCAR returns by simultaneous activation of the CODAR systems is apparent in the data.

TABLE OF CONTENTS

I. INTRODUCTION.....	1
A. GENERAL	1
B. HF RADAR	1
1. Resonant Backscatter from Ocean Waves.....	2
2. OSCAR.....	3
3. CODAR	3
II. DATA AND METHODS.....	9
A. LOCATION.....	9
B. PROCESSING.....	9
1. Spectral.....	9
2. Radial Vectors	10
a. Contamination.....	10
3. Total Vectors	12
a. Mathematical Calculation.....	12
b. Filtering	14
4. Vector Averages.....	15
a. Daily Averages	15
b. Canonical Day Average.....	15
III. TIDAL PERIOD FLUCTUATIONS.....	41
A. BACKGROUND.....	41
1. Tidal Constituents.....	41
B. HARMONIC ANALYSIS	42
C. OBSERVATIONS.....	44
1. Elliptical Description and Definition.....	44
2. M2 Constituent.....	44
a. Descriptive	44
b. Current Rotation	45
c. Division of Tidal Periods.....	45
3. K1 Constituent.....	46
a. Descriptive	46
b. Current Rotation	46
c. Division of Tidal Periods.....	47
D. ANALYSIS	47
1. Semidiurnal Cycle	47
2. Internal Tide Indications	47
a. Ellipses	47
b. Direction of Rotation	48
c. Amplitude.....	48
d. Direction of Flow	48

e. Influence of Generation Site.....	48
3. Diurnal Cycle.....	49
IV. SEABREEZE	65
A. BACKGROUND.....	65
1. Sea/Land Breeze Dynamics.....	65
B. Local Topography.....	65
C. Data.....	66
D. Analysis.....	66
1. Station Description and Comparison.....	66
2. Canonical Day Winds.....	67
3. Wind and Current at MBARI M1	67
a. Characterization.....	67
b. Observational Analysis.....	68
c. Statistical Analysis	68
d. Interpretation.....	69
4. Seabreeze and K1 Tidal Component.....	70
V. CONCLUSIONS AND RECOMMENDATIONS.....	85
A. CONCLUSIONS.....	85
1. System Evaluation.....	85
B. RECOMMENDATIONS.....	86
LIST OF REFERENCES.....	89
INITIAL DISTRIBUTION LIST	93

ACKNOWLEDGEMENT

I wish to thank my thesis advisor, Dr. Jeffrey Paduan, for his hours of support, patient listening, and the effort of tactfully pointing me in the proper direction. I am grateful to him, as well as both Drs. Leslie Rosenfeld and Robert Bourke, for posing astute questions which provoked additional insight.

My deepest gratitude belongs to Mr. Michael Cook of the Naval Postgraduate School Oceanography Department. His expertise in computer programming and the various analysis tools we used were essential to my successful completion. Not only did he provide me with technical support, but also with a great deal of moral support.

Finally, I wish to thank my extended family, the Monterey Bay H.O.G. chapter, especially Peter and Rachel Braccio, Don and Trena Tannahill, Dave Butters, Craig Bramhall, and Ron Oswald. They kept me afloat with a realization of the Jimmy Buffet lyrics: "If we weren't all crazy, we would go insane."

I. INTRODUCTION

A. GENERAL

The importance of our coastal waters is immense. Even before the shift of the military's interest to littoral zones, these areas played a dominating role in the fisheries, tourism, recreation and real estate industries. Today, following the end of the cold war, the U.S. Navy is focusing tactics and technology towards operation in shallow waters. Thus, understanding and observations of littoral-zone characteristics and processes are more greatly needed than ever before.

Oceanographers have made extreme progress over the past few decades in their ability to study the complicated flow structures near the coast, especially with satellite instrumentation. Products, such as Sea Surface Temperature (SST) imagery from the Advanced Very High Resolution Radiometer (AVHRR), make it possible to visualize the two dimensional front and eddy structures and, sometimes, to infer the direction of current motion. However, these space-based sensors have limiting factors that make them unsuitable for continuous or detailed coastal study. One limitation, the lack or degradation of coverage during cloudy periods, is particularly detrimental to the study of the littoral zone. Furthermore, these sensors measure ocean temperature, color, or microwave backscatter patterns, but they do not measure, directly, ocean currents.

Fortunately, technologies not as affected by weather have also seen progress. One of these technologies, high frequency radar, is capable of measuring currents. This paper evaluates the performance of a type of high frequency (HF) radar known as Ocean Surface Current Radar (OSCR) over a 53-hour period from Monterey Bay, California. Included in the evaluation is a discussion of data processing. Also included is an examination of the data with regards to expected tidal and seabreeze characteristics based on prior results from a different type of high frequency radar network.

B. HF RADAR

The use of the HF radar band (3-30 MHz) to measure surface currents remotely is proving to be an effective and informative tool. Traditionally, surface current measurements are taken by employing either Lagrangian or Eulerian methods based on drifting buoys or fixed current meters, respectively. With these, the observations are either tempo-

rally or spatially incomplete, or both. They are also time and labor intensive, and can be very costly in terms of ship time or satellite tracking costs. HF radar measurements represent shore-based remote sensing systems. Once installed, they provide relatively constant spatial and temporal coverage with minimal additional investment. More importantly, HF radar measurements provide the only method to obtain continuous two-dimensional maps of surface currents over broad coastal areas. In recent years, the coastal region of Monterey Bay has been instrumented with two types of HF radar (CODAR and SeaSonde), collectively known as Coastal Ocean Dynamics Applications Radars (CODAR; the distinction between the two CODAR types will be provided later). These instruments are installed at three locations around Monterey Bay. Data from these systems are collected and shared by members of the Monterey Bay HF Radar Consortium¹ and a number of CODAR-based results have recently been published (Paduan and Rosenfeld, 1996; Melton, 1995; Foster, 1993; Neal, 1992; and Paduan et al., 1995). Presently, the CODAR data management occurs as part of the ONR-funded real time environmental monitoring system known as REINAS. This is operated by UC Santa Cruz and NPS. Throughout 4-8 May, 1995, the OSCR system was deployed around Monterey Bay with the intention of comparing the two HF radar systems. The specifics of this installation will be discussed later. First, a review of the operational principals behind the use of HF radar by both systems is presented, followed by brief descriptions of OSCR and CODAR, to aid in comprehension of the data processing and evaluations performed.

1. Resonant Backscatter from Ocean Waves

HF radar systems utilize high frequency radio frequencies transmitted from coastal antennae to measure the surface currents. A peak radar energy return results from resonant backscattering of the energy by waves whose wavelengths are one half that of the transmitted beam (Bragg scattering). In the HF band, these resonant scatterers are short (3m-6m) surface gravity waves. Over deep water, the phase speed of these waves is known. Therefore, a Doppler analysis of the returned frequency indicates the dynamic influence of the surface current superposed on the known velocity of the reflecting wave train. Figure 1 shows an illustration of this method from Barrick et al. (1977). An actual spectrum collected by the OSCR system is shown in Figure 2. The dashed lines indicate the "no current" Bragg frequencies. Δf measures the Doppler shift of the Bragg peaks pro-

¹ The Monterey Bay HF Radar consortium consists of members from the Naval Postgraduate School (NPS), UC Santa Cruz, CODAR Ocean Sensors, LTD., Stanford University, Monterey Bay Aquarium Research Institute, United States Coast Guard, and National Oceanographic and Atmospheric Administration.

duced by the current (Graber et al., 1996). The depth to which this current measurement is effective is dependent on the radar frequency. The radar wavelength, λ , divided by 8π , results in the approximate depth measured (Stewart and Joy, 1974). Since OSCAR and some types of CODAR systems operate at 25.4 MHz, the Bragg wavelength, $\lambda/2$, is approximately 3 m and the measurement depth is approximately 1 m.

2. OSCAR

In the OSCAR system, a four element transmit antenna illuminates a 90 degree region, centered on the look direction of the antenna, with radar pulses. A linear phased-array antenna, scanning at high azimuthal resolution, receives the backscattering of the signal. The system samples for five minutes and can provide data every 20 minutes. With a longer array, a larger base is available for direction differentiation. The OSCAR antenna array is productive at lengths ranging from approximately 50 to 100 m in length, with maximum resolution at 100 m for the reason described above. The standard OSCAR configuration has a sixteen element phased array spread over approximately 80 m. (Iverson, 1996)

Each HF radar station produces data in the form of radial vectors using the Bragg resonance phenomenon described above. These are measurements of current speeds, throughout the area of coverage, that are either directly toward or away from the station. Using two stations, a master and a slave, the combination of the radial signals produce total current speed and direction vectors with cited accuracy of 4 to 5 cm/sec and $\pm 10^\circ$ according to manufacturer's information. Chapman et al. (1996) suggest that the uncertainties in OSCAR-derived current observations are closer to 8 cm/sec. The deployment of OSCAR around Monterey Bay is presented in Chapter II.

3. CODAR

CODAR uses the same principles as OSCAR to determine the current direction and speed. The primary difference is in its antenna design and associated software. Instead of a digitally steered linear array of antennas, it uses direction finding techniques. A pair of orthogonally mounted cross looped antennas mounted on a monopole antenna are employed. Each of the two looped antennas, as well as the monopole antenna, have known beam patterns in relationship to the look angle. The direction from which the return signal arrives is determined by the ratio of the three antenna strengths according to the method of Lipa and Barrick (1983).

The three CODAR systems deployed around the bay consist of two newer Sea-Sonde systems operating at approximately 12.5 MHz and one older CODAR system

operating at 25.4 MHz. The SeaSondes are located at Pt. Pinos (near Monterey) and the Long Marine Laboratory in Santa Cruz, California. The older CODAR is located at the Monterey Bay Aquarium Research Institute (MBARI) in Moss Landing, California (Figure 3). Two of the differences between the older and newer systems are the type of signal used and the timing of the data collection and production. The SeaSonde uses Frequency Modulated Continuous Wave (FMCW) transmit technology vice pulsed transmissions. It continuously samples and can provide weighted averages at an hourly rate. The older CODAR takes samples over 30 minutes and provides data every two hours. The impacts of the different frequencies used by each system are discussed in a later section.

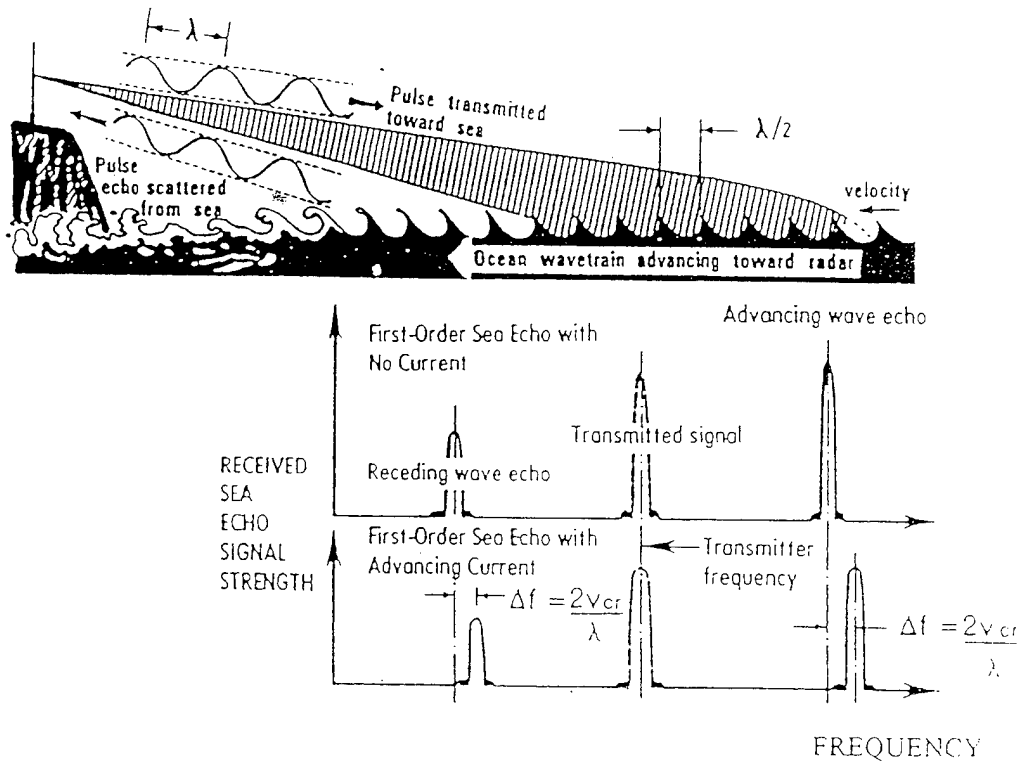


Figure 1. Illustration of the first order Bragg scattering effect of an HF radar pulse incident on the sea surface and the associated Doppler shifts from the surface gravity waves with and without an underlying current (from Barrick et al., 1977).

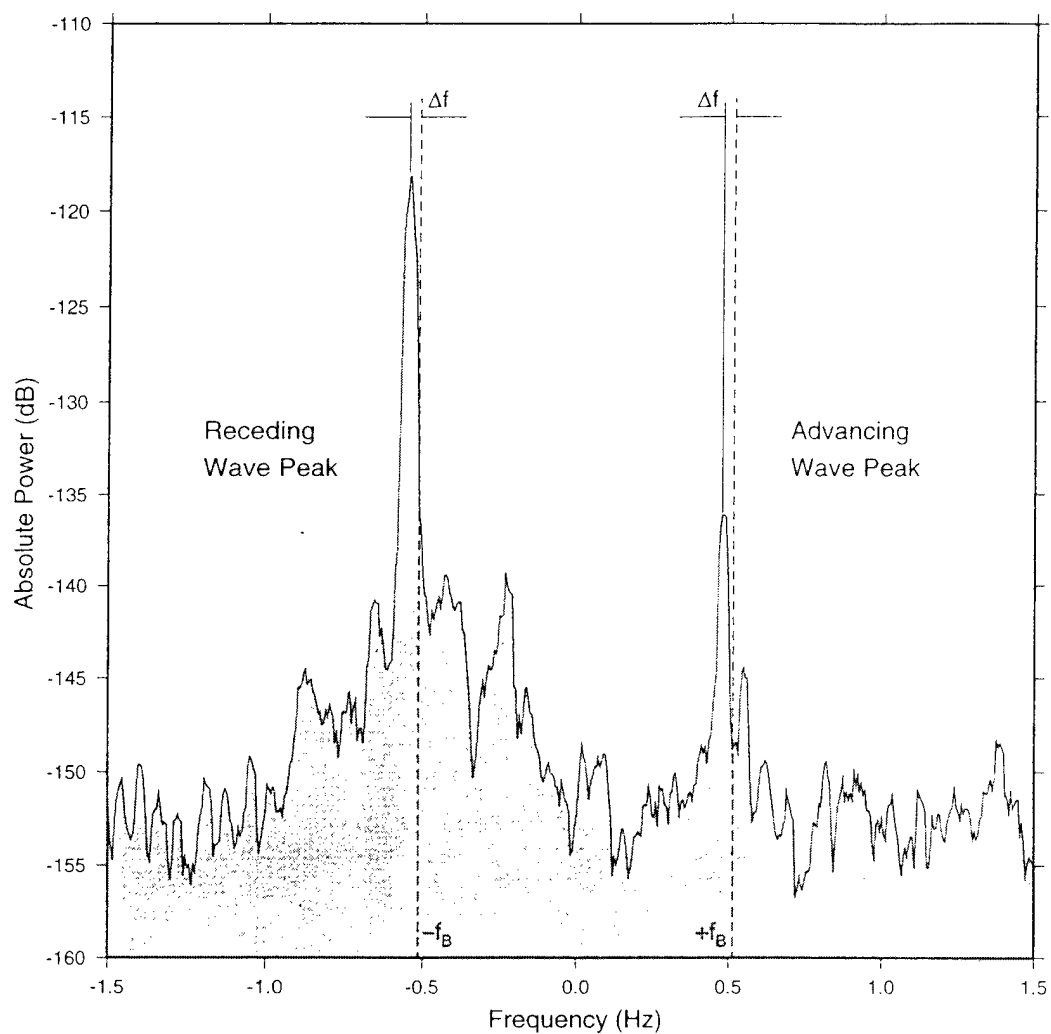


Figure 2. Typical HF Doppler spectrum collected by the OSCAR system during the High-Res Experiment. Note the two Bragg peaks Doppler-shifted by the surface current. The positions of no-current Bragg frequencies are shown by the vertical dashed lines (from Graber et al., 1996).

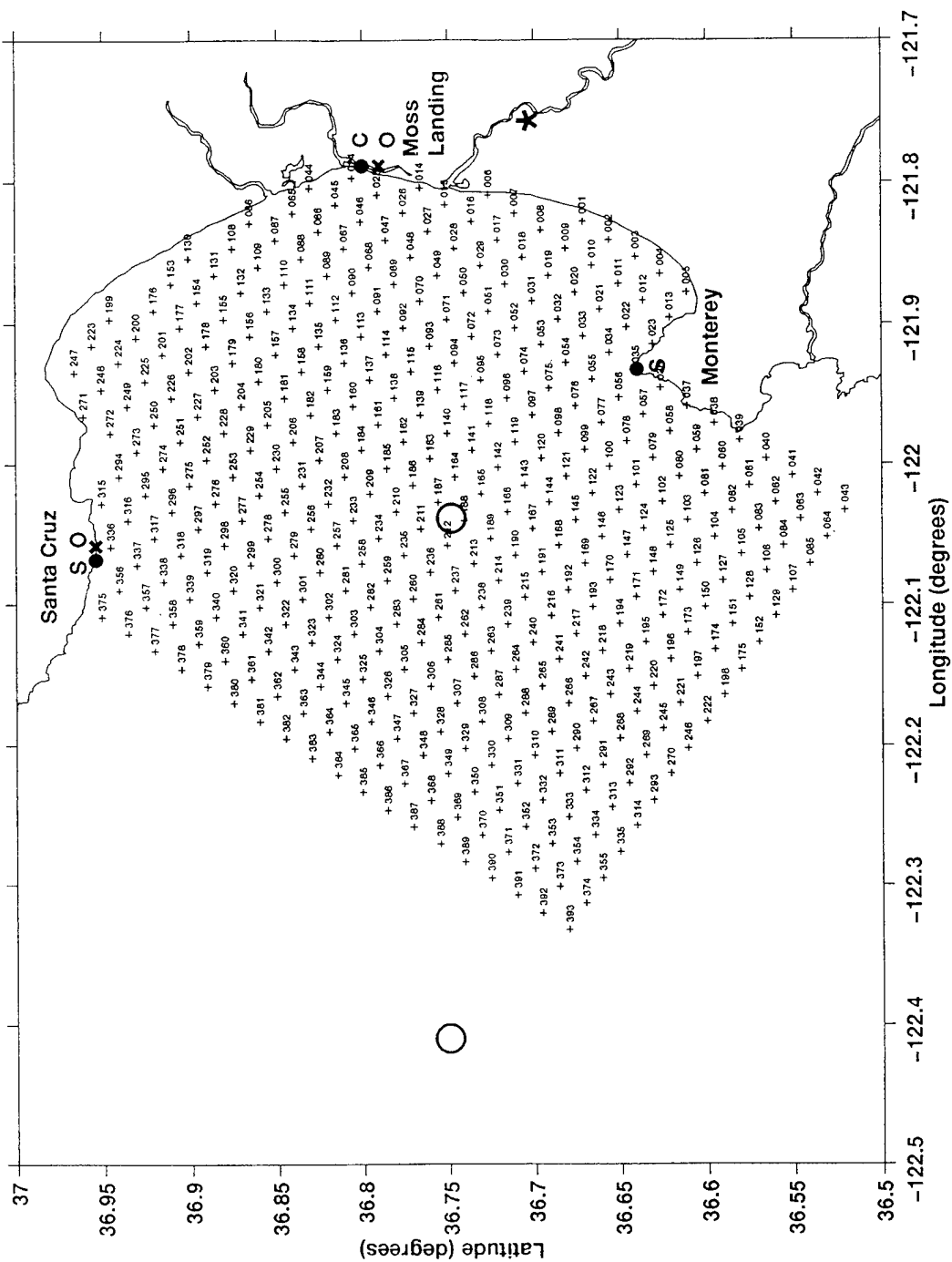


Figure 3. CODAR (C)/SeaSonde (S) and OSCR (O) shore sites with overwater grid locations and wind measurement locations around Monterey Bay. From left to right, the wind locations are: the NDBC 46042 and MBARI M1 moorings (watch circles), and Fritsche Field vertical wind profiling site (*).

12

II. DATA AND METHODS

A. LOCATION

A demonstration deployment of a two-site OSCR system was conducted in Monterey Bay during the period 5-8 May, 1995. The deployment was sponsored by the manufacturer, Marconi Radar Systems, and by Global Environmental and Ocean Sciences Limited (GEOS) of the United Kingdom. Both master and slave sites were operational from 1000 GMT 6 May to 1500 GMT 8 May, 1995. This period is used in this study to evaluate OSCR performance and investigate diurnal current fluctuations in Monterey Bay.

The Master OSCR station was set up at Long Marine Lab in Santa Cruz, CA with a reduced 11-antenna array. This is the same location as the newer CODAR SeaSonde system (Figure 3). The slave OSCR station was installed at the Moss Landing Marine Lab in Moss Landing, CA with a full compliment of 16 antennas as there were no spatial limitations at that site. However, that array was misaligned by 15 degrees relative to the broadside angle entered into the processing algorithm. This error was corrected by rotating the initial position of the radial currents from this site by 15 degrees relative to the slave site before including them in the total vector computation described below (Fernandez and Paduan, 1996). The older CODAR, also located at Moss Landing, was in the Monterey Bay Aquarium Research Institute (MBARI) building, approximately 100 m away. The exact CODAR locations are important as they interact with OSCR in a manner that will be discussed later.

B. PROCESSING

During the period of operation, pulses of energy were sent out by each station. The back scattered reflections were received and evaluated by the stations every 20 minutes. The operation of the slave and master stations were identical, but timing of the slave's cycle was lagged by five minutes. The following sections discuss the different filtering steps used to evaluate the data resulting from the above processes.

1. Spectral

There were generally over 650 data points (radial current estimates) produced by each OSCR station at every activation. A quality index value was assigned automatically to each data point based on several factors as described in the OSCR user manual. These

included, in descending order of importance: the number of Bragg peaks, the size of the largest peak, the Bragg Ratio, the width of the primary Bragg peak and the error in Bragg separation. The quality index ranged from a value of zero to nine. For example, the Bragg Ratio is the height ratio between the Bragg peaks representing the advancing and receding wave trains (refer back to Figure 2). The magnitude of the ratio provides useful classification and quality assessment information. Index values below four are assigned to those spectra that have only one Bragg peak and therefore no Bragg ratio (Iverson, 1996). Only those data points whose index was four or higher were used in this study. This initial filtering was performed on the OSCAR raw data by D.M. Fernandez of University of California, Santa Cruz according to criteria listed in the OSCAR User Manual (Fernandez and Paduan, 1996). It performed a basic separation of usable data from obvious noise.

2. Radial Vectors

In addition to the threshold filtering based on the OSCAR quality index, further quality control thresholding was applied to the radial data and, in turn, to the vector currents derived from it. All radial speeds with magnitudes greater than 100 cm/sec were discarded as they are considered to be unrealistic for Monterey Bay. As the remaining radial data was reviewed, it was discovered that three types of maps were produced. Figures 4 through 6, respectively, are examples of normal, excessive velocity, and reduced range radial maps. To provide an overview of the data and to determine times and/or patterns of the abnormal radial maps, Figure 7 was created. The top panel is the absolute mean radial velocity from all radial vectors produced during each master or slave station activation or "snapshot." The bottom panel documents the number of velocities that contributed to the mean values in the top panel. Note the spikes in both panels; these are due to the abnormal radial maps (e.g., Figures 5 and 6) and indicate the contamination discussed below.

a. Contamination

The slave station snapshots that contain a mean velocity in excess of approximately 30 cm/sec (e.g., Figure 5) produce the spikes shown in the top panel of Figure 7. These high mean velocities are evidence of contamination by the CODAR station located at Moss Landing. This station operates at a frequency of 25.4 MHz, exactly the same frequency as OSCAR. Early in the study period, it was turned off, but during the last day it was re-activated with a duty cycle that was on for 28 minutes every two hours. All data from the radial current estimates associated with the spikes > 30 cm/sec in Figure 7 were eliminated from the dataset. The corresponding master snapshots were also neglected as there is evidence for the contamination of both stations by the one CODAR station's

activation. The contamination to the master data was evidenced by either spiking in mean velocity or a significant drop in valid data points (i.e., those that passed the quality indexing criteria). The velocity spikes in the master data tend to be smaller than those in the slave data, but are still easily seen in the top panel. The drops in available data, which are correlated in time with each of the spikes, can be observed in the second panel of Figure 7.

The SeaSonde in Santa Cruz, although operating at a different frequency (11.5-13.5 MHz), also caused contamination of some OSCAR data. This station was manually activated on four occasions, for durations of one hour. The known activation times are easily correlated with the first, second, third and fifth spikes contained in the OSCAR master data shown in the bottom panel of Figure 7. The individual spikes are easy to identify as they are blocked off at the bottoms, indicating several consecutive time periods of equally reduced data numbers. Unlike contamination by the Moss Landing CODAR as discussed above, only the adjacent OSCAR station is affected. However, both the slave and master vector snapshots were excluded from further evaluation. The severe reduction of data (e.g., Figure 6) is likely due to an increased noise level produced by the SeaSonde, thus reducing the effective range of coverage of the OSCAR.

Figures 8 and 9 show range of coverage for the OSCAR master station over specific time periods. Figure 10 illustrates the same for the slave station. Note the limited range for the times 1940 through 2020 on 6 May in Figure 8. This is the time period of the first master low data spike in Figure 7. This is a pattern of interference by the SeaSonde station. The OSCAR is receiving high intensity noise from the SeaSonde. That is, because the SeaSonde produces a strong signal from a location very close to the OSCAR, any valid signals from the more distant areas need to be strong enough to support their validity in the signal to noise ratio evaluation in the quality index assignment. The stronger signals make it through, but the weaker returns are not detected well enough through the SeaSonde's signal to be considered of high enough quality to report. The maps generated for the times 1840 through 1920 on 7 May cover a normal period with no contamination present.

The first two maps on Figure 9, 7 May 2240 and 2300, were constructed from data in which the contamination effects are from both the SeaSonde and CODAR stations. The pattern is identical to that created by the SeaSonde station. Two additional types of interference patterns were created by the Moss Landing CODAR station. These are presented for the times 0100 and 0120, 8 May. Additional examples of the interference are also provided with maps made for times 0300 and 0320, 8 May. The range of coverage increases, but the outer data points either do not pass through the quality index screening

process or they have a magnitude exceeding 100 cm/s. The data points with excessive velocity are indicated by "x's." The larger coverage is expected as there is more distance between the OSCR and CODAR sites.

The maps of May 6 1945 through 2025 in Figure 10 are normal slave returns. The nodal pattern is due to each point in the original grid being rotated approximately 15 degrees clockwise to match up with the actual slave station alignment. The slave OSCR station appears not to be affected by activation of the SeaSonde station and presents variable return patterns when contaminated by the CODAR. Examples of the results are provided for times 2105, 2125, and 2325 on 7 May. They contain various mixtures of low data point coverage and excessive vector velocities, which again are indicated by "x's." Characterization of the post-filtering data set is shown in Figure 11. The upper and lower panels are consistent with the data types presented in Figure 7. The radials of this dataset were used to create time series of total vectors.

3. Total Vectors

As discussed previously, the radials from each HF radar station were combined to produce vector values for the surface current field. The x-y grid used previously for the CODAR network in Monterey Bay (e.g., Paduan and Rosenfeld, 1996) was used to map these total, or vector, currents with the radials from the two-site OSCR network. The grid has approximately 2 km spatial resolution and 393 points within the OSCR coverage area (Refer to Figure 3). The operational dataset, therefore, consisted of a time series of u and v velocity components and their associated mapping uncertainties. The uncertainty values, or mapping errors, are related to the amount of directional ambiguity present in the utilized group of radial vectors. These values were used as filtering criteria for the derived vectors.

a. Mathematical Calculation

To explain this further, the following mathematical description from Gurgel (1994) is presented. Figure 12 contains a geometric representation of the total vector problem using two radial vectors (OSCR solutions used in this study contained up to 9 radial vectors simultaneously). Referring to the figure, equations describing the process by which radial vectors $\vec{U}r1$ and $\vec{U}r2$ are transformed into u and v components of the total vector \vec{U} are as follows:

$$u * \cos \theta_1 + v * \sin \theta_1 = |\vec{U}r1| \quad (2.1)$$

$$u * \cos \theta_2 + v * \sin \theta_2 = |\vec{U}r2| \quad (2.2)$$

In the illustrated example, the radial currents are traveling in the negative direction, away from the station points. However, values input for the radial vectors are the absolute values. The sign of the radial vectors is accounted for by the angles θ_1 and θ_2 . For example, if the radial vectors were in opposite directions, their angles would be 180° larger, or approximately 220° and 330° for θ_1 and θ_2 , respectively. The resulting total vector would be positive in the u component and negative in the v component, opposite to the one presented in the figure.

When more than two radials are available, the problem is overdetermined and the components u and v are obtained as a least squares solution. In this case, matrix notation is convenient and the above equations generalize to:

$$\underbrace{\begin{bmatrix} \cos \theta_1 & \sin \theta_1 \\ \vdots & \vdots \\ \cos \theta_n & \sin \theta_n \end{bmatrix}}_A \cdot \underbrace{\begin{bmatrix} u \\ v \end{bmatrix}}_a = \underbrace{\begin{bmatrix} |U_{r1}| \\ \vdots \\ |U_{rn}| \end{bmatrix}}_b \quad (2.3)$$

If a pre-existing error field is known, such as instrument error, then a weighting function (σ) may be used to modify the data kernel in Equation 2.3 to become:

$$A = \begin{bmatrix} \frac{\cos \theta_1}{\sigma_1} & \frac{\sin \theta_1}{\sigma_1} \\ \vdots & \vdots \\ \frac{\cos \theta_n}{\sigma_n} & \frac{\sin \theta_n}{\sigma_n} \end{bmatrix} \quad (2.4)$$

As station instrument errors were not known, only equation 3 was used.

The solutions for u and v minimize the squared error:

$$\epsilon^2 = |A \cdot a - b|^2 \Rightarrow \text{Minimum} \quad (2.5)$$

and the solution to Equation 2.5, using singular value decomposition, becomes:

$$a = C \cdot ((A^T) \cdot b) \quad (2.6)$$

where

$$C = (A^T \cdot A)^{-1} \quad (2.7)$$

is the covariance matrix (Menke, 1984) and T denotes matrix transpose. The u solution is $a(1)$ and the v solution is $a(2)$. C_{11} is the variance in the u direction and C_{22} is the variance in the v direction. The mapping errors, e_u and e_v , are $\sqrt{C_{11}}$ and $\sqrt{C_{22}}$, respectively.

b. Filtering

The above process takes place inside a mapping program whose final output consists of a 393-point total surface current vector snapshot at any desired regular time interval. One criteria for the total vector production was the search radius around each mapping point. Radial vectors within this radius were used in the equations described above to form the total vector shown in the map. In this study, a search radius of 1.5 km was selected through elimination of smaller and larger radii that either were not consistent in the number of radials covered or that smoothed out detailed circulation features. It is worthy to note that as the radii for each mapping point overlap, some radial vectors may be shared. This will prevent each mapping point from being completely independent. Although not a hindrance in the present case, this property and the size of features studied should be considered when determining the search radius used.

Threshold filtering was applied to the vector current results in addition to the earlier filtering steps applied to the radial current data. The maximum total vector velocity was set to 75 cm/sec, based on reasonable values for Monterey Bay. A maximum mapping error value was set at 40 cm/sec. This number was chosen based on histograms of the total vector velocities and the mapping error values (not shown). Over 90% of the data were within these velocity bounds.

Figure 13 assigns to each mapping point a percentage reflecting the amount of valid data within the time series of constructed total vectors. Times with flagged or invalid data derive from all of the aforementioned filtering steps. The figure shows nearly complete coverage over most of the grid with reduced coverage at the farthest ranges.

Finally, a time criteria was used to produce different flow maps best suited to each informational requirement. For instance, to show the total mean flow of the surface current within Monterey Bay, the center time of the 53-hour dataset was chosen and a map (Figure 14) was produced that averaged together all radial vectors 27 hours ahead of and 27 hours after that time.

4. Vector Averages

a. Daily Averages

Several features can be observed in the 53-hour mean currents in Figure 14. The primary flow is a strong persistent flow across and outside the mouth of the bay that moves north to south with some west to east component. The velocity is strong, approximately 30 cm/sec. The flow gets progressively weaker toward the bay's interior. Here, a localized, secondary circulation is found. At the northern tip of the grid, the current moves in a southwestward direction, curving cyclonically until the flow in the center of the bay is toward the northeast.

This two-day-average picture can be compared to a two-day mean flow measured by CODAR just prior to the deployment of OSCAR. In Figure 15, the primary flow is seen with the same velocity pattern in the region of overlapping coverage. Previously using longer records, CODAR has been able to pick up this primary circulation. This is demonstrated by the CODAR-derived average currents for the month of September 1992 (Figure 16) in which the cyclonic circulation is clearly present (Foster, 1993).

To compare the degree of similarity between the two full days of OSCAR data, each day's mean surface current pattern was formed by making two maps (Figure 17), each using the radial data 12 hours ahead of and after the map time. Essentially, the daily averages are the same, but there are some subtle differences. During the first day, the primary current was broader and more spatially consistent than during the second day when it had more of a curve at its entry point into the grid and dominated less of the grid. Perhaps a meander of the California Current changed its position, and therefore its effect on the bay over the two days. Changes can also be observed in the secondary feature. The axis of the cyclonic rotation was farther to the north during the first period, and the northeast flow inland of the axis was enhanced over that flow in the second period.

b. Canonical Day Average

Canonical hourly maps were also produced. These were made by taking corresponding hours from each "day" and averaging them together (Neal, 1992; Foster, 1993). The number of hours available for the average ranged between two and three, as

there were only two complete 24-hour cycles available for analysis. The result was an hourly representation of currents on an average day. Maps for the time period of 1000 GMT to 1700 GMT and their corresponding mapping errors are presented in Figures 18 through 25. Note the formation of a cyclonic pattern that begins to appear at approximately 1300 GMT. As the vortex of the circulation migrates northwest towards Santa Cruz, the vectors toward the east strengthen and become more uniform. This reflects the beginning of the seabreeze influence and preconditions the surface waters for their flow into the bay with the wind.

The mapping errors presented with the canonical-hour maps are represented as vectors formed from e_u and e_v . Since these are strictly positive, the error vectors are restricted to point in the first quadrant only. Horizontal error vectors indicate maximum mapping uncertainty in the u velocity component while vertical error vectors indicate maximum uncertainty in the v component. The largest mapping errors remain along the outer edges of the grid, indicating that the original excellent mapping quality is maintained by the canonical averaging method.

Figures 26 and 27 contain canonical hourly currents for an entire day, including the hours discussed above, in local time (PDT) for ease of comprehension of the typical daily cycle. The strengthening flow resulting from the seabreeze can be clearly seen during the afternoon hours as can the relaxation into localized circulation during the nighttime and early morning hours, and the preconditioning period described previously. The seabreeze pattern is a dominant feature of Monterey Bay and will be discussed in Chapter IV.

In Chapters III and IV, the vector current data from the OSCR network is used to describe the higher frequency fluctuations in a more rigorous fashion. The basic dataset used in the evaluation of tidal and diurnal-period fluctuations of the Monterey Bay surface currents consisted of hourly maps. These were constructed with a time search area of 30 minutes to each side of the hour. These maps generally included three sets of radial returns from both the master and slave stations (these correspond to the "snapshot" patterns shown in Figures 8 through 10). Exceptions that included less than three returns available to produce the map were due to the elimination of returns that were contaminated by CODAR transmissions, as discussed previously.

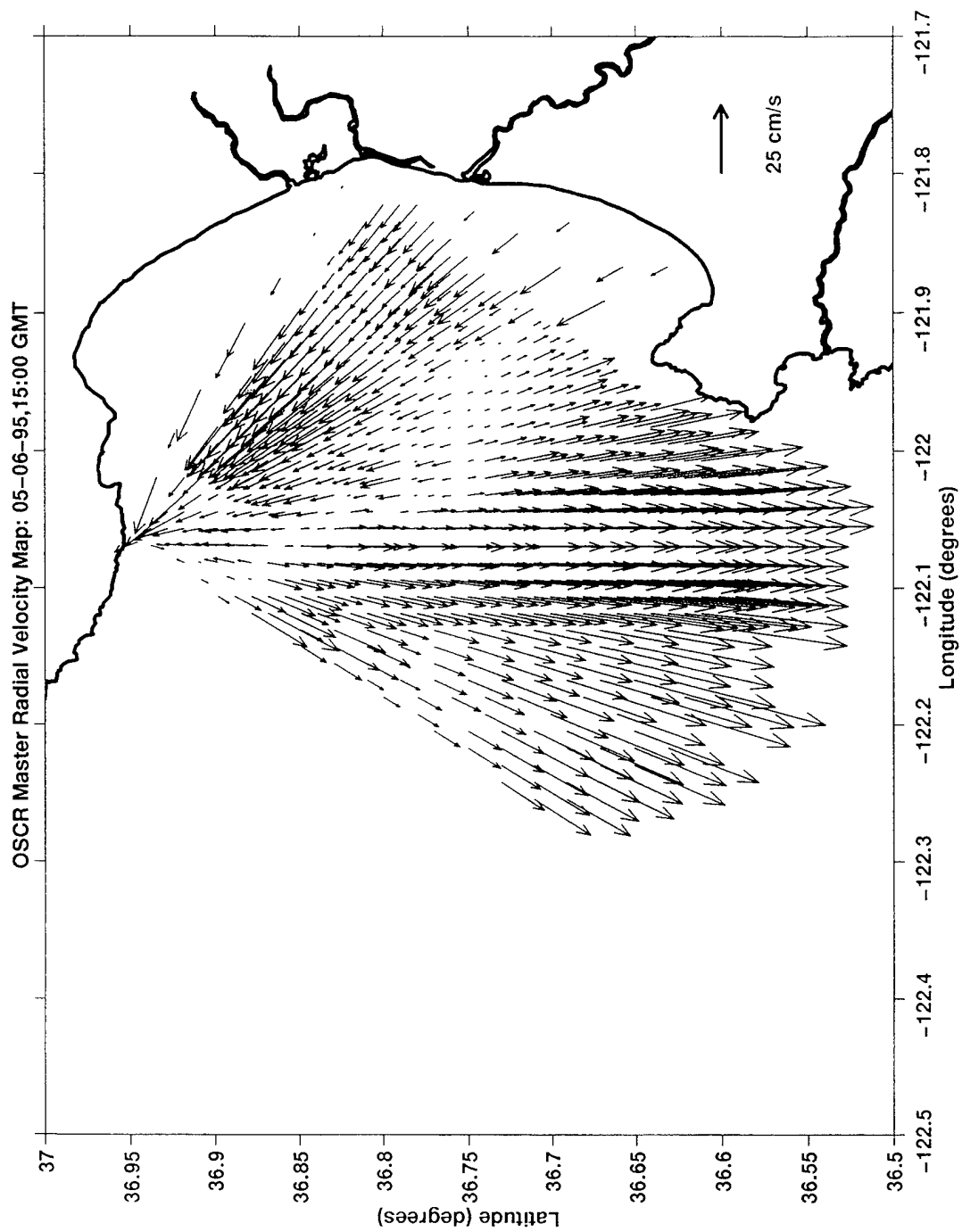


Figure 4. Normal OSCR radial vector map from Santa Cruz site.

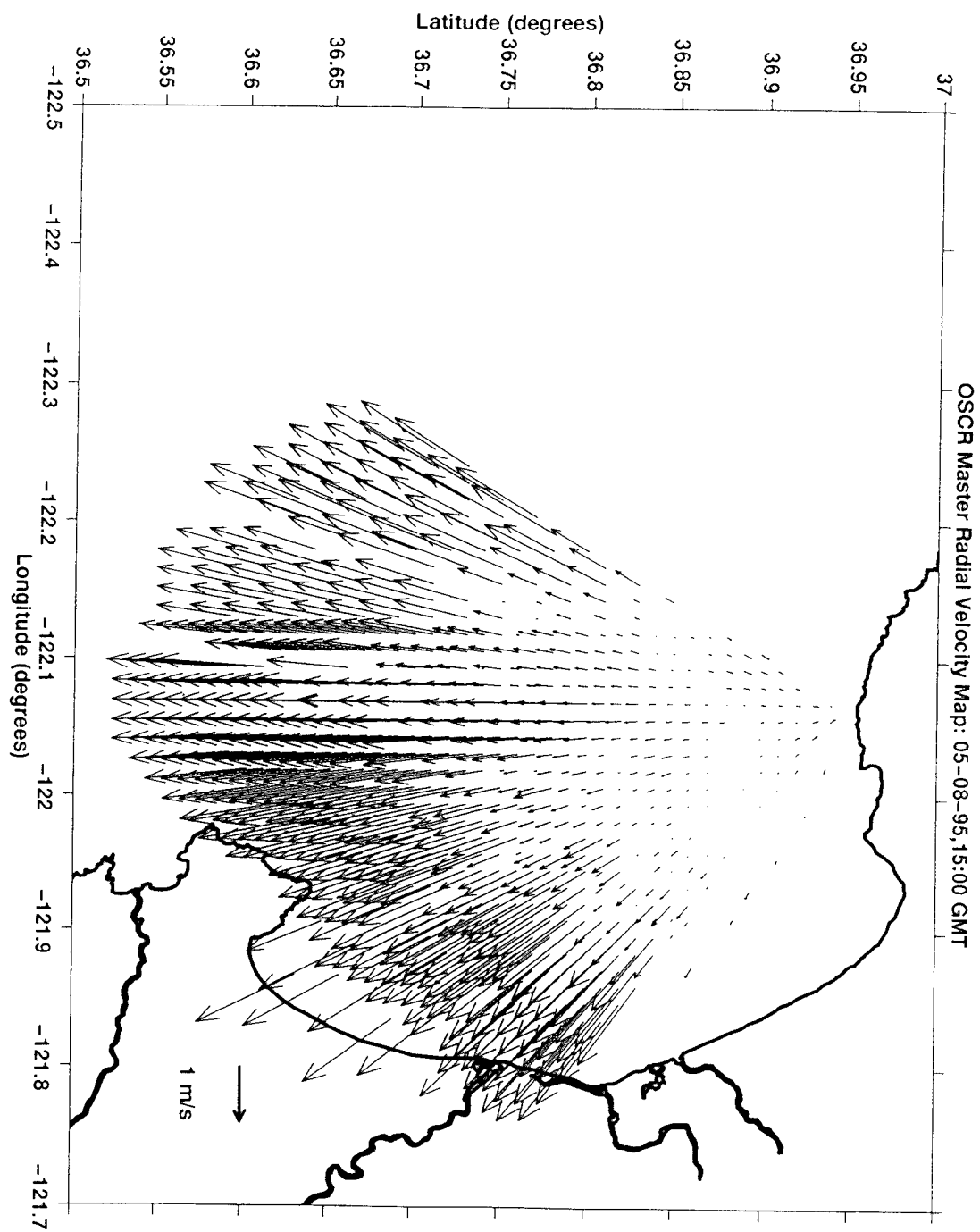


Figure 5. OSCR radial vector map showing excessive velocities. Note scale change compared with Figure 4.

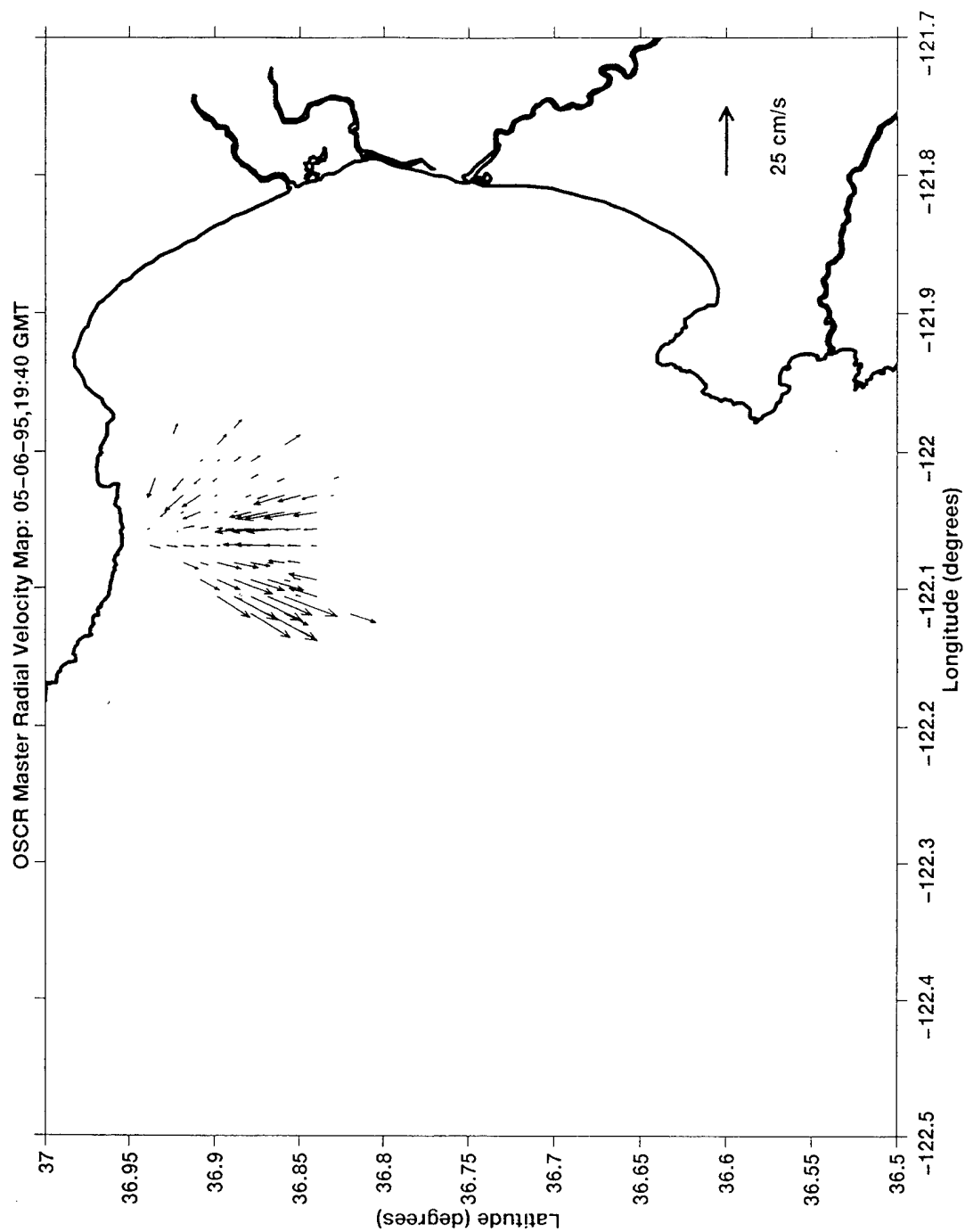


Figure 6. OSCR radial vector map showing insufficient data return and associated low range.

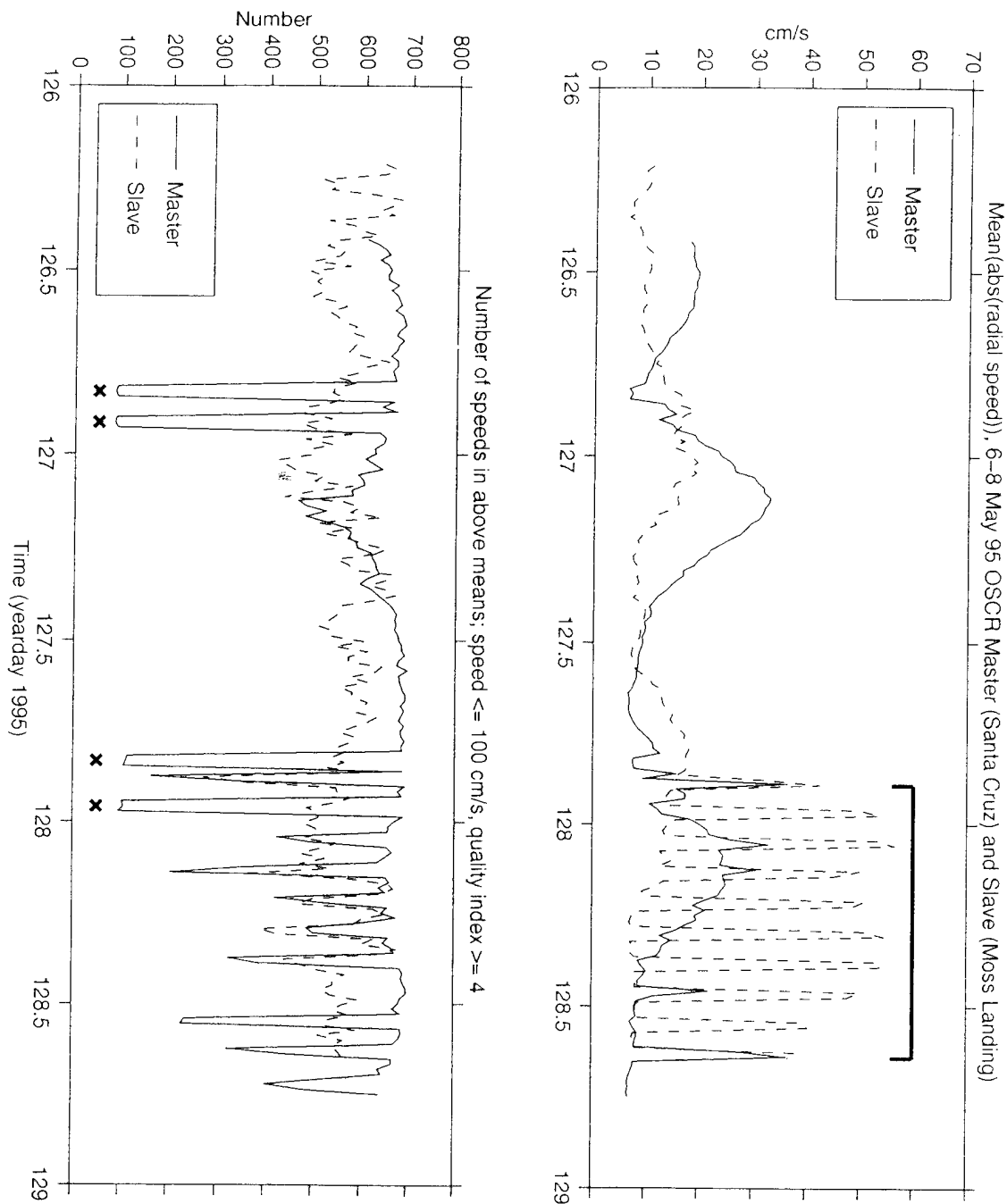


Figure 7. Time series of spatially averaged radial velocities (upper panel) and number of data returns (lower panel) for master and slave stations. Filtered data includes only those with speeds ≤ 100 cm/sec and with quality index ≥ 4 . Effect of contamination by the SeaSonde at Santa Cruz is seen in the low coverage times (x), while contamination by the CODAR at Moss Landing is seen in the excessive average speeds (overbar).

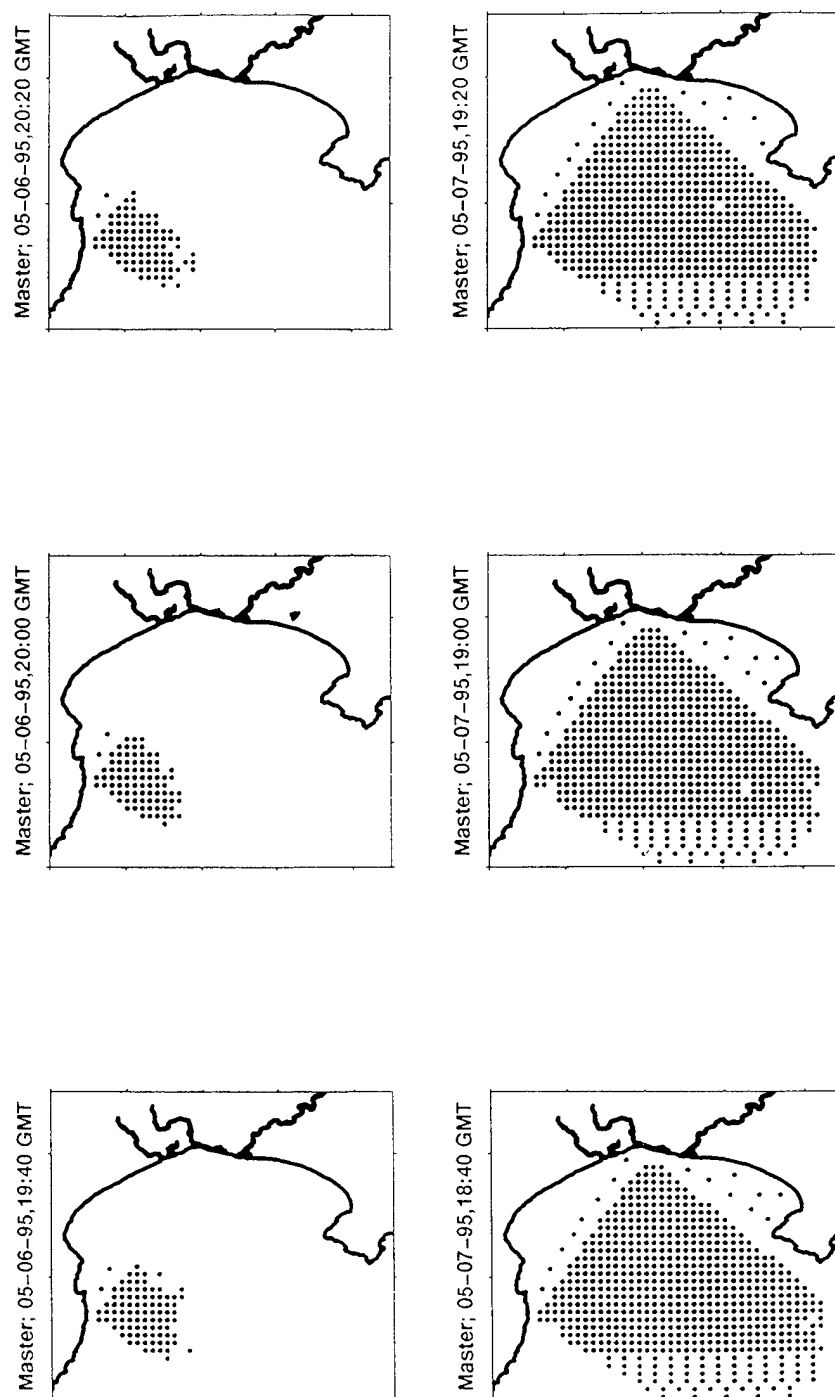


Figure 8. Maps of OSCAR master site coverage for various times. Map times 1940 through 2020, 6 May show limited coverage range due to contamination by the CODAR Santa Cruz site. Times 1840 through 1920, 7 May show normal coverage.

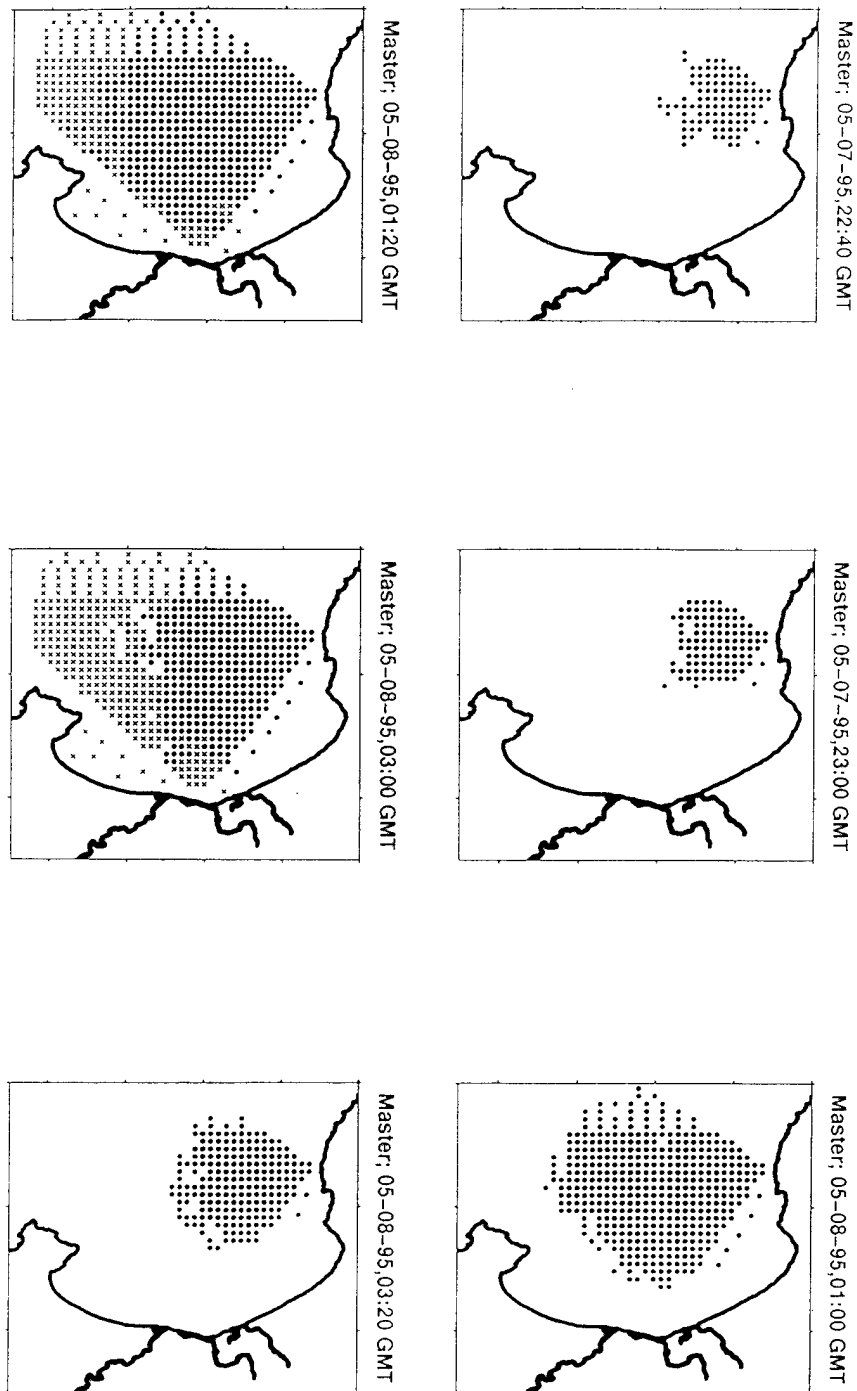


Figure 9. Maps of OSCR master site coverage for various times. "x" indicates velocities greater than 100 cm/sec. Map times 2240 and 2300 show affects from contamination by both CODAR and SeaSonde sites. Times 0300 and 0320 show additional interference patterns.

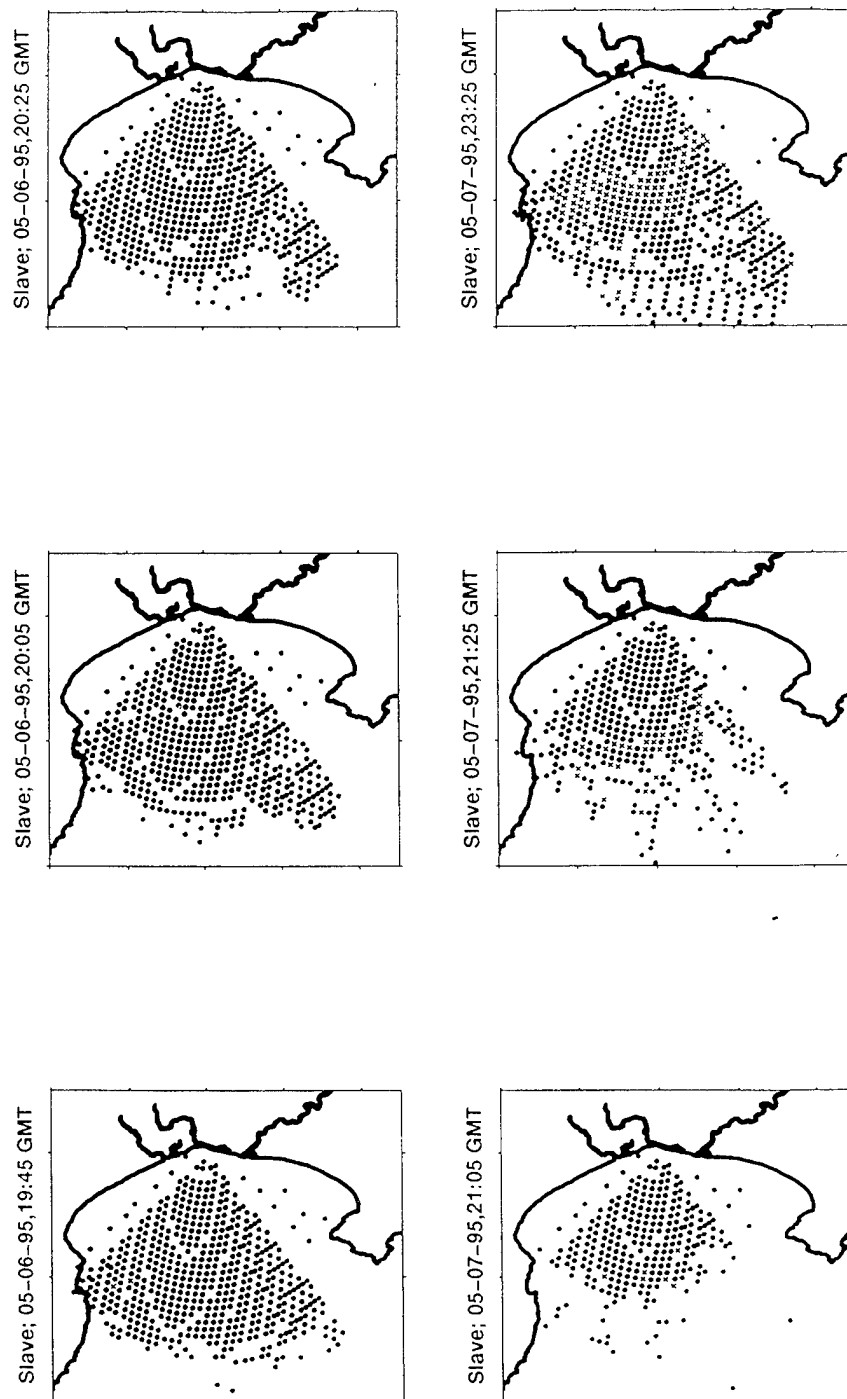


Figure 10. Maps of OSCR slave site coverage for various times. "x" indicates velocities greater than 100 cm/sec. Map times 1945 through 2025, 6 May show normal coverage. Map times 2105 through 2325, 7 May show the variable mixtures of low coverage in range and excessive velocity.

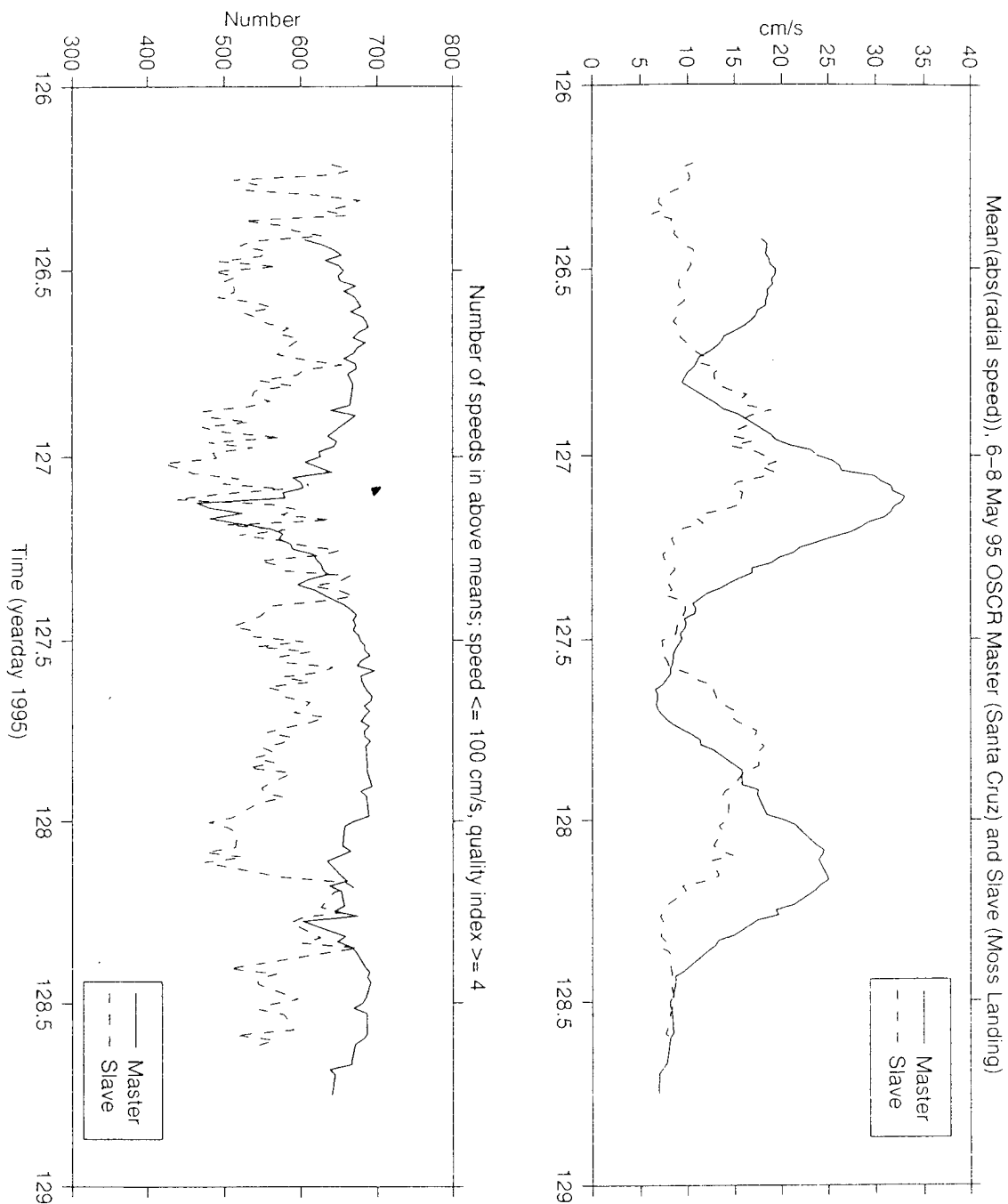


Figure 11. Time series plots similar to those shown in Figure 7 with contaminated data removed.

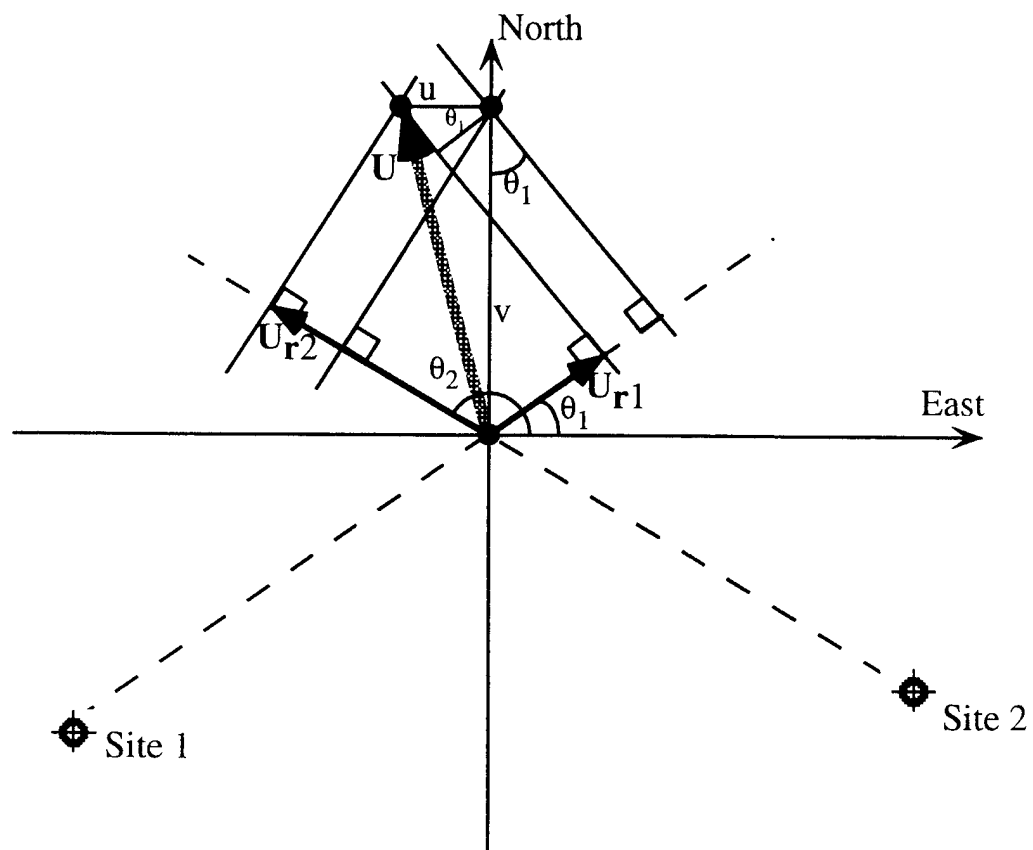


Figure 12. Geometric calculation of surface current \vec{U} from two radial components \vec{U}_{r1} and \vec{U}_{r2} (after Gurgel, 1994).

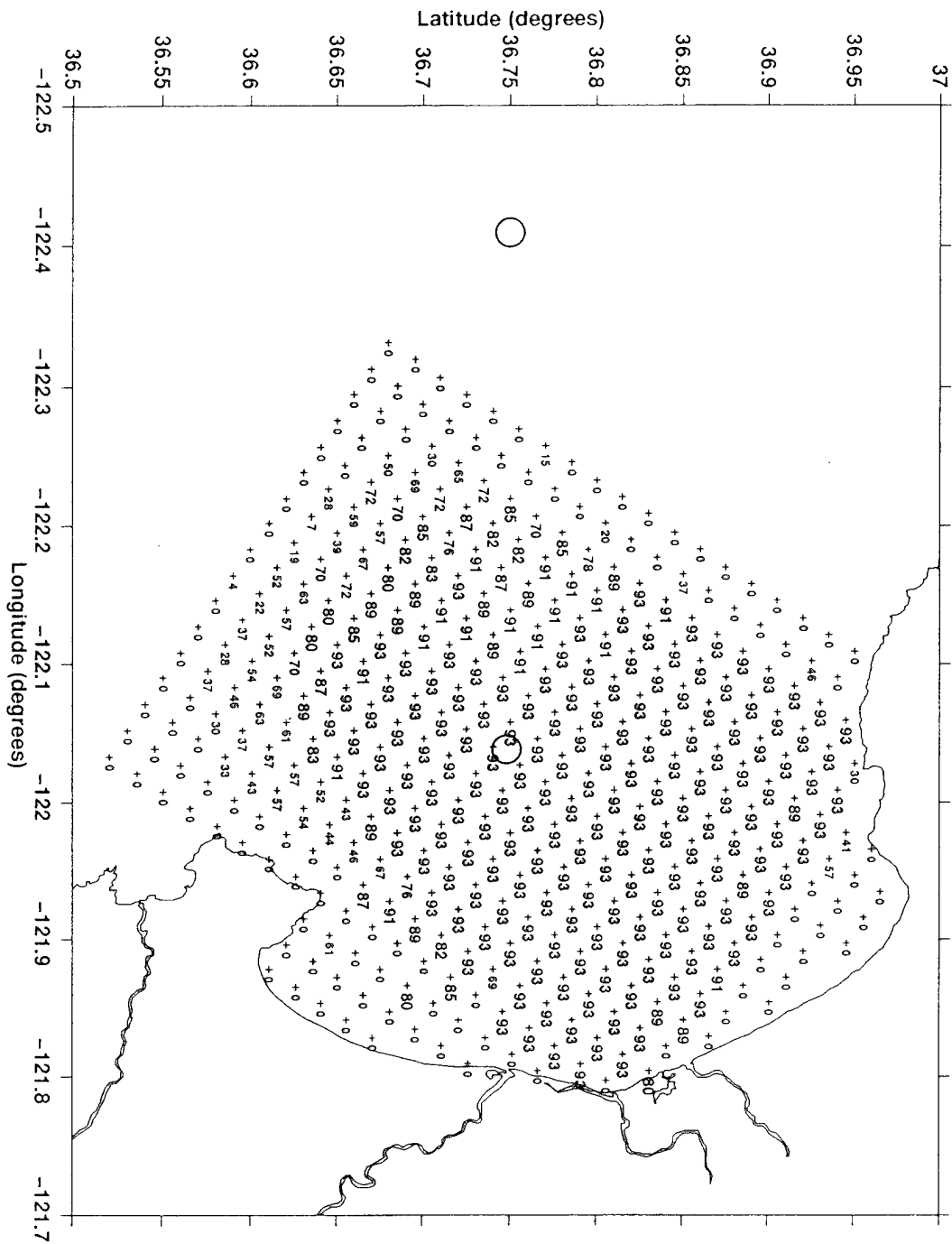


Figure 13. OSCR percent coverage map of Monterey Bay for May 6-8, 1995.

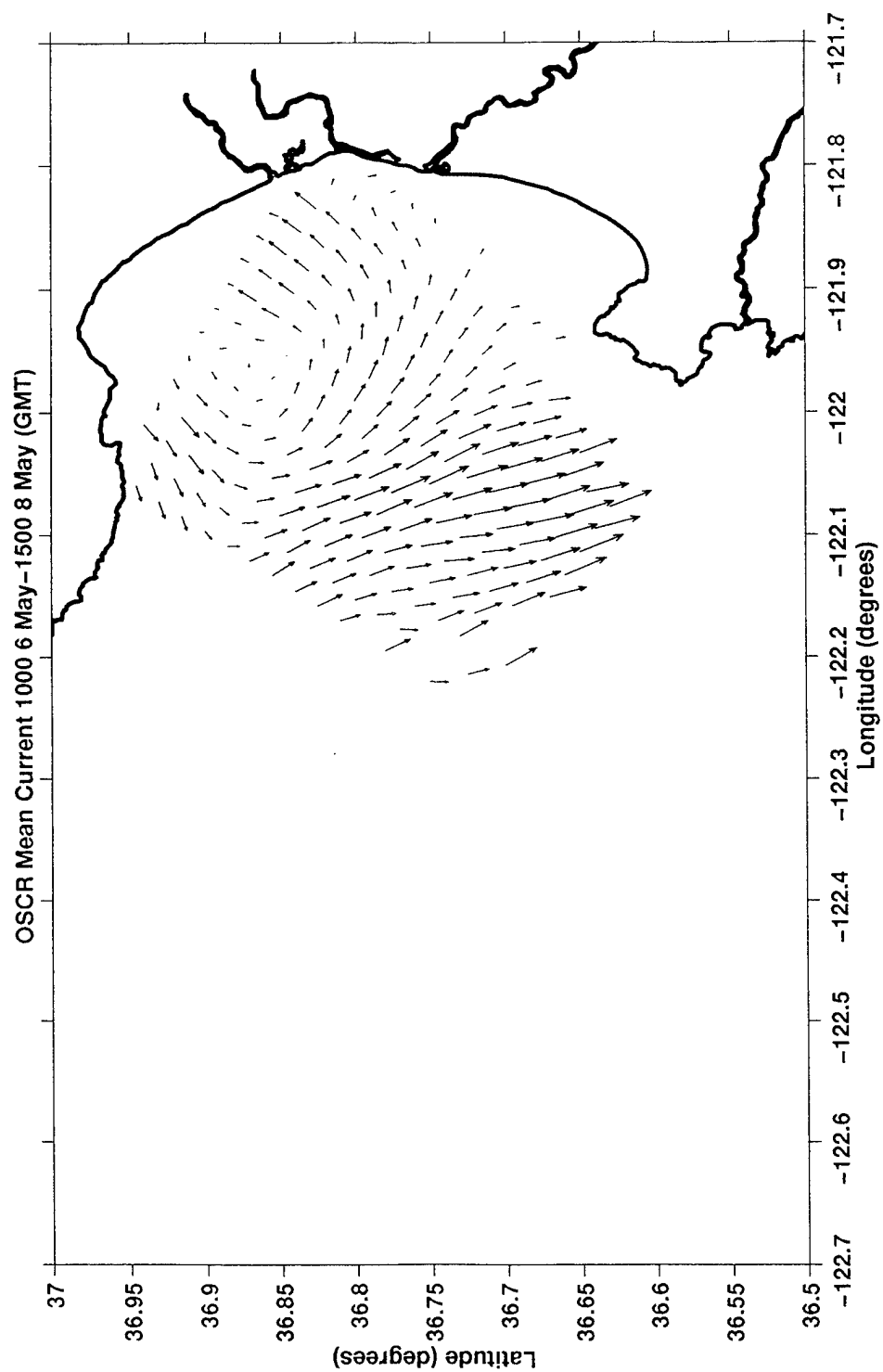


Figure 14. OSCR-derived mean surface current flow over 53-hour period, 1000 GMT 6 May to 1500 GMT 8 May, 1995.

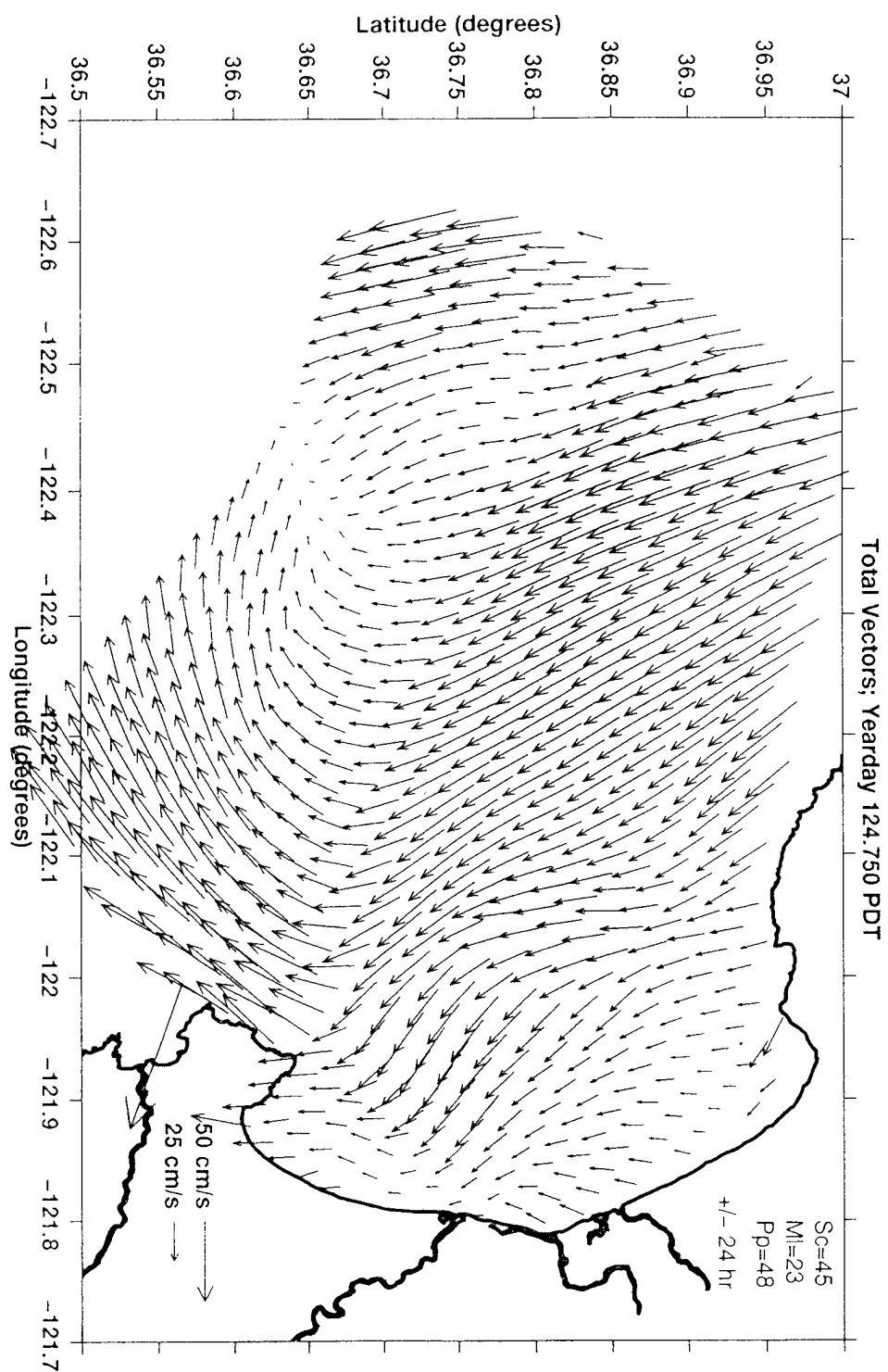


Figure 15. CODAR-derived mean surface current flow over 48-hour period, 1800 GMT 3 May to 1800 GMT 5 May, 1995.

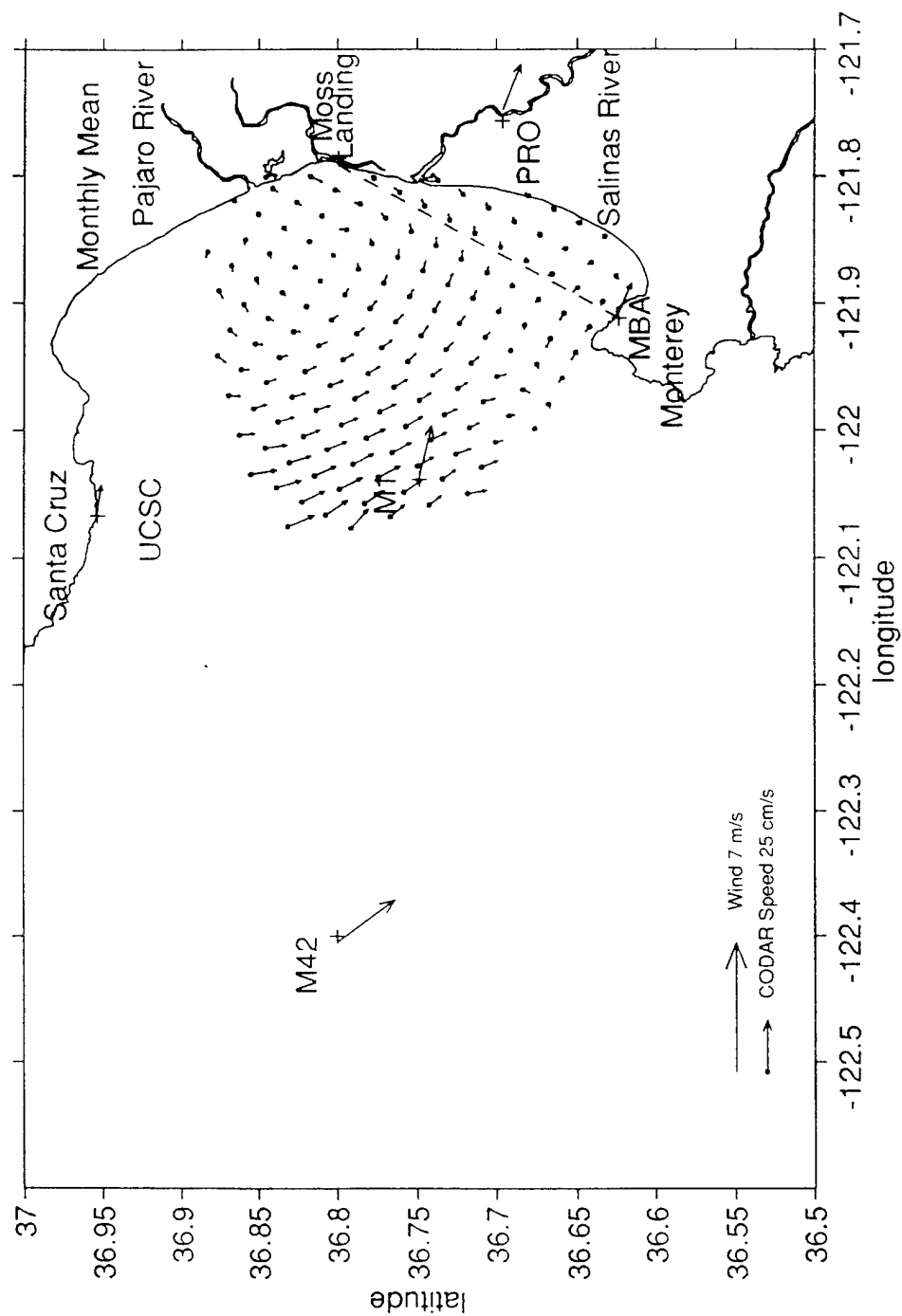


Figure 16. CODAR-derived mean current and wind fields for September 1992 (from Foster, 1993).

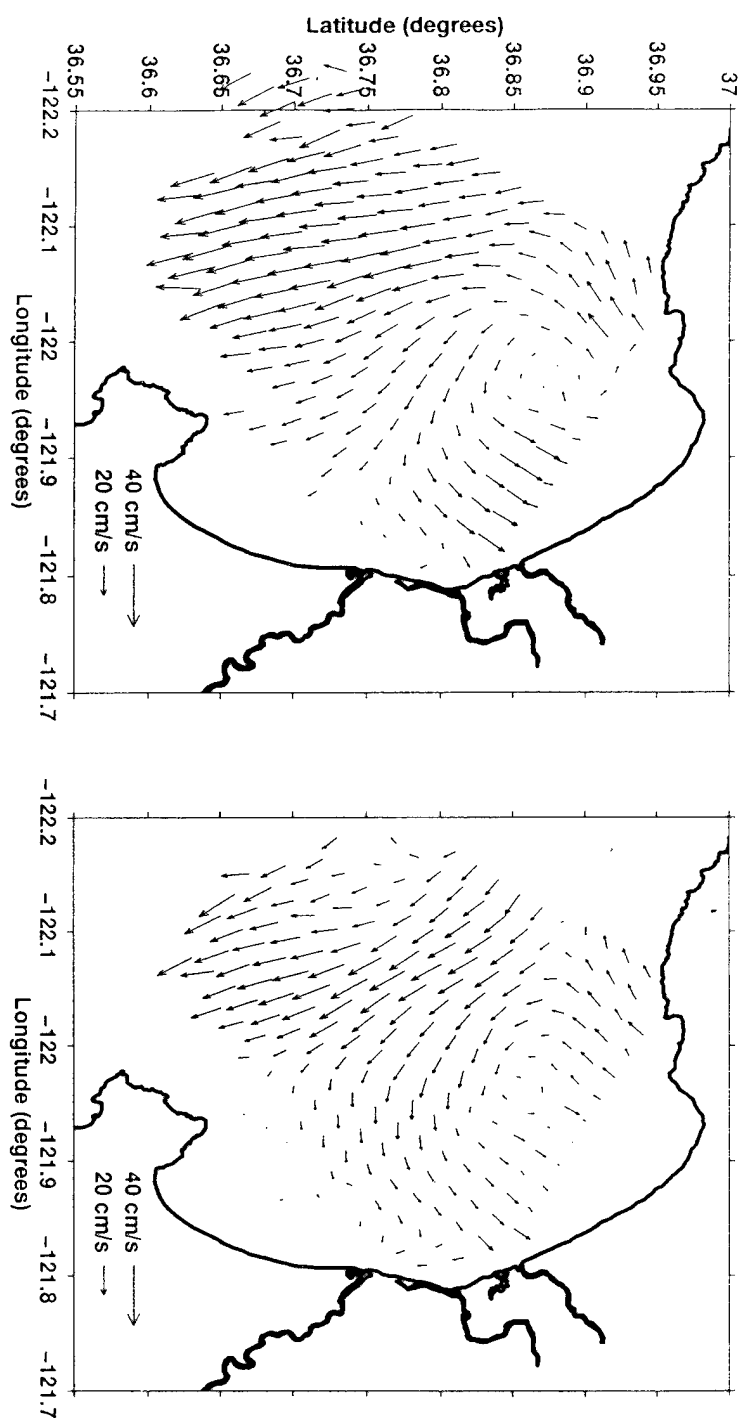


Figure 17. OSCR-derived mean surface current flow over the 26.5 hour period, 1000 GMT 6 May to 1230 GMT 7 May 1995 (left) and, 1230 GMT 6 May to 1500 GMT 8 May, 1995.

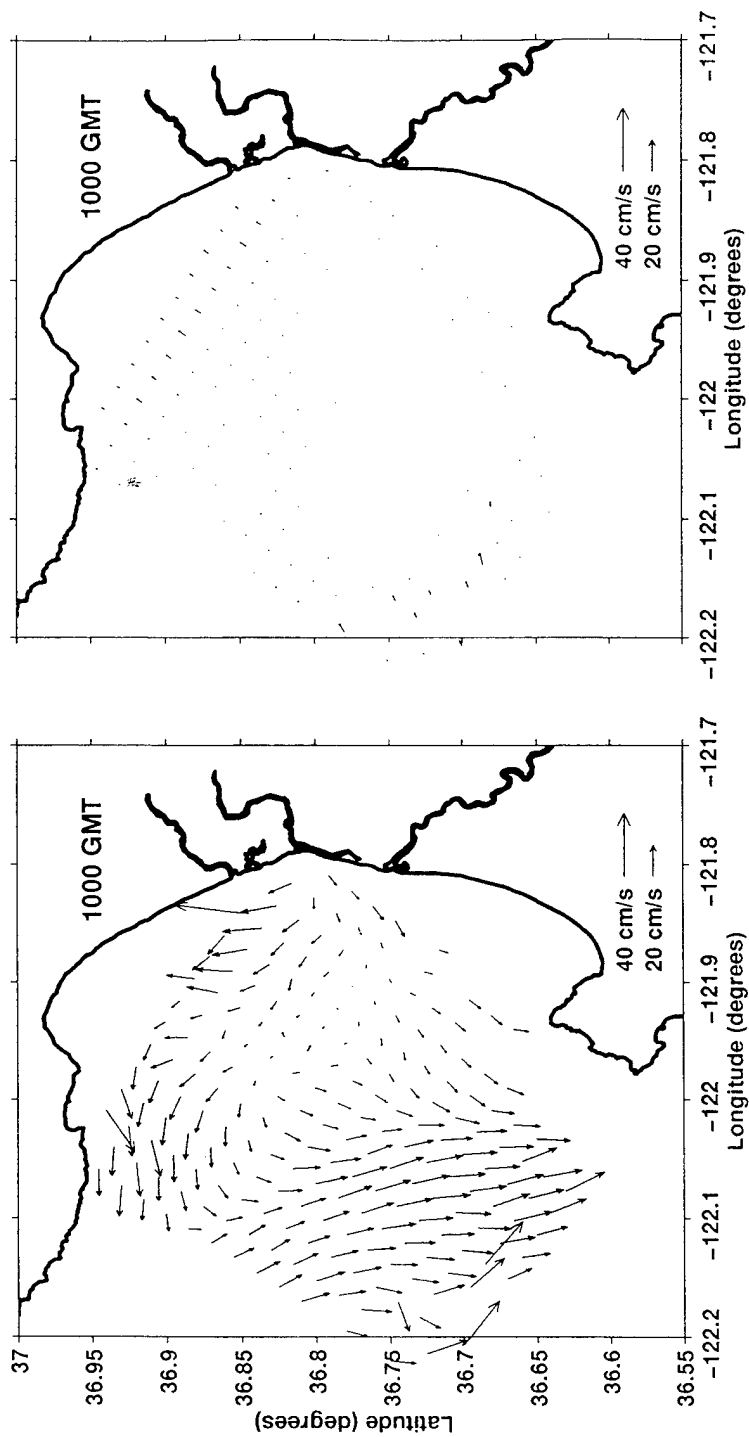


Figure 18. OSCR-derived canonical flow (left) for 1000 GMT with associated mapping error (right).

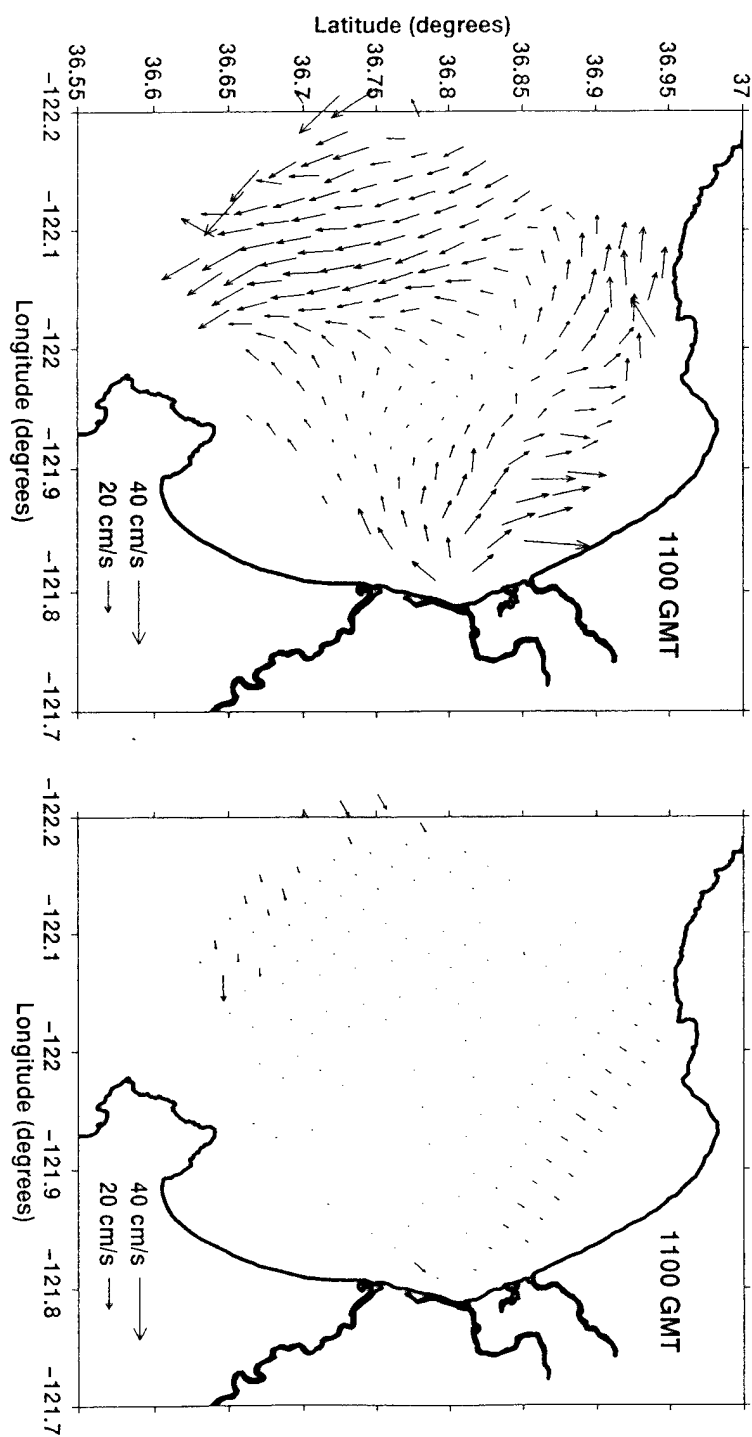


Figure 19. OSCR-derived canonical flow (left) for 1100 GMT with associated mapping error (right).

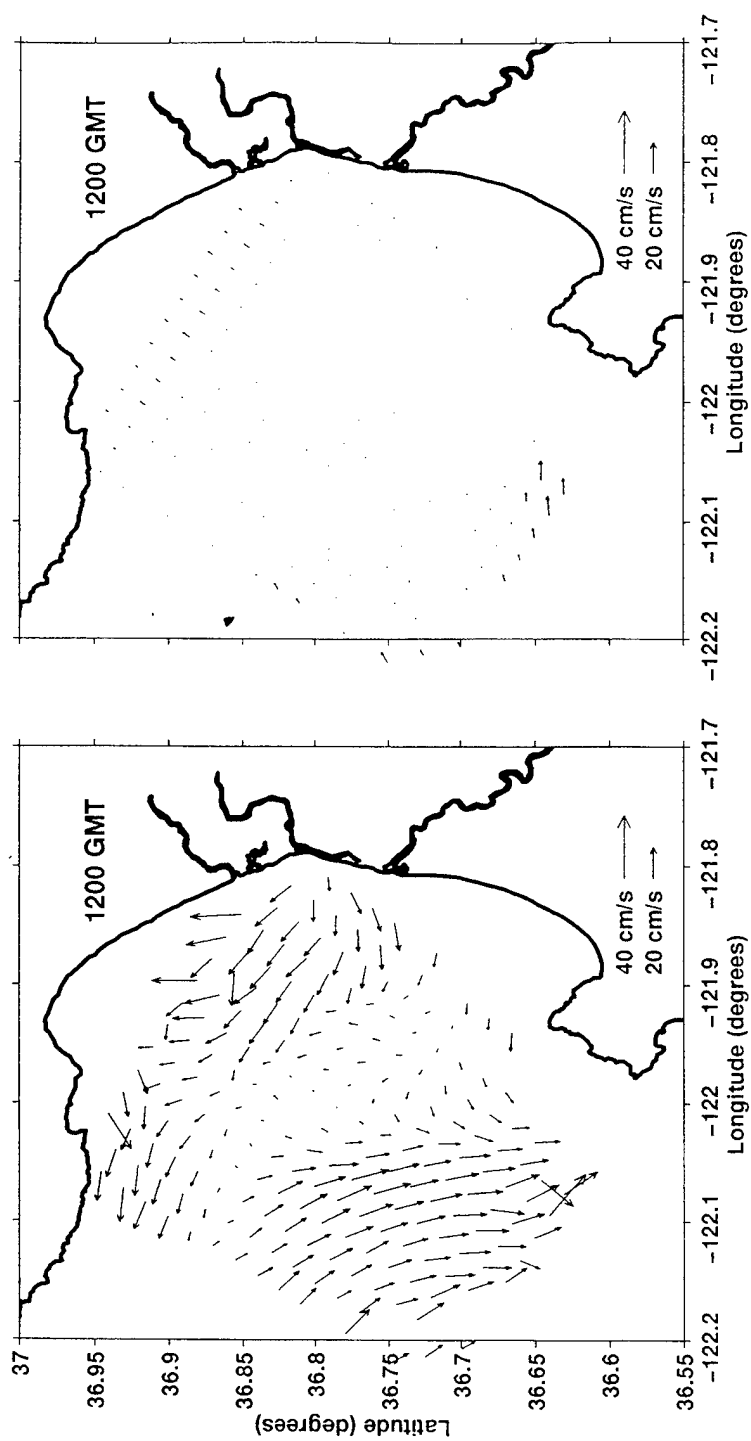


Figure 20. OSCAR-derived canonical flow (left) for 1200 GMT with associated mapping error (right).

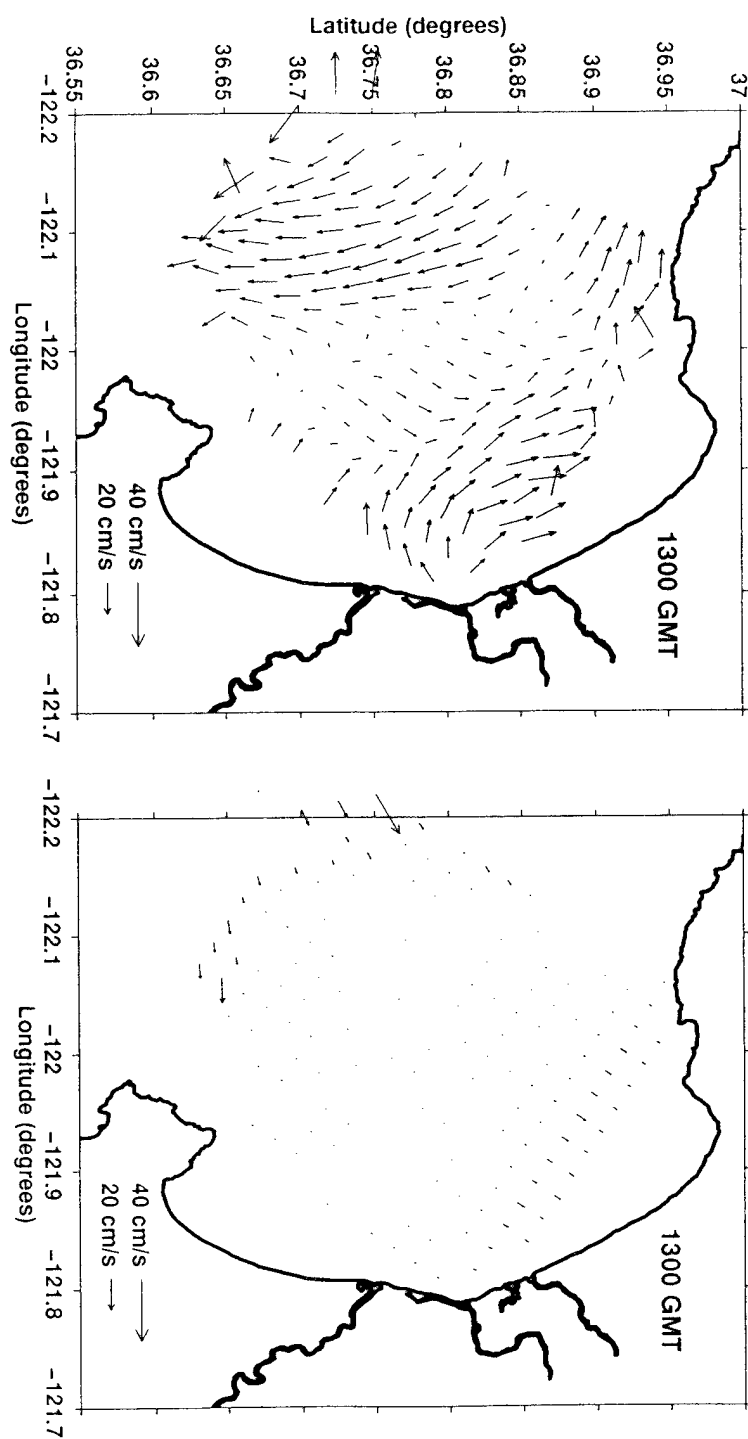


Figure 21. OSCR-derived canonical flow (left) for 1300 GMT with associated mapping error (right).

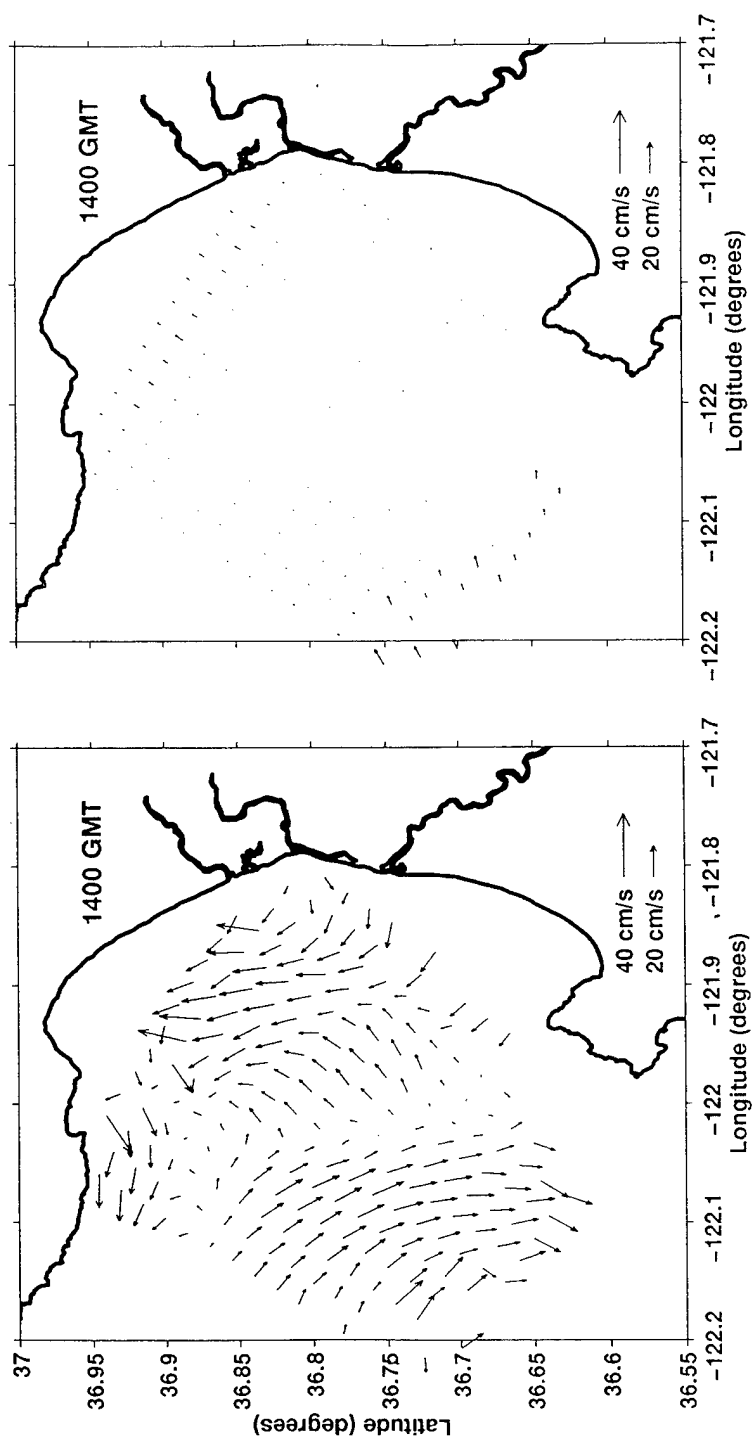


Figure 22. OSCR-derived canonical flow (left) for 1400 GMT with associated mapping error (right).

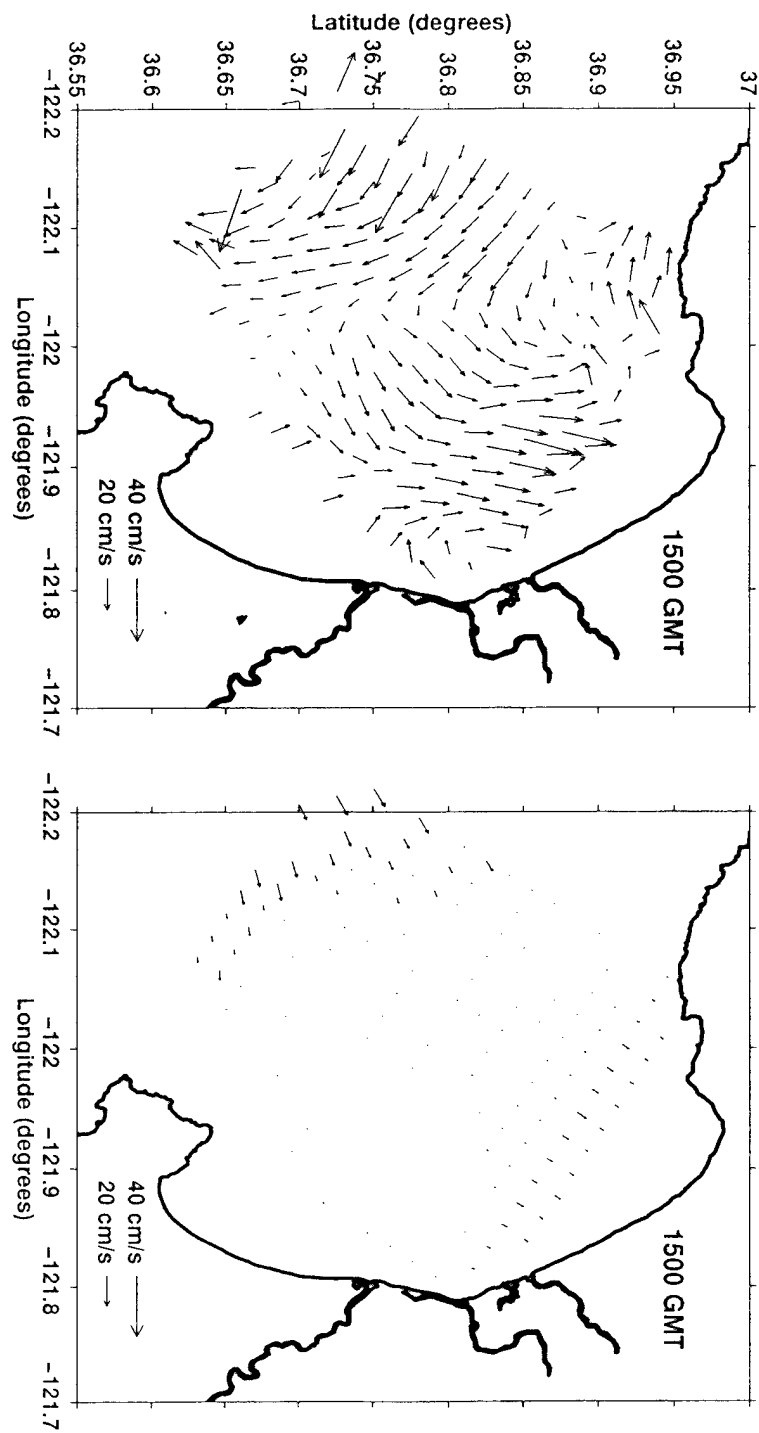


Figure 23. OSCR-derived canonical flow (left) for 1500 GMT with associated mapping error (right).

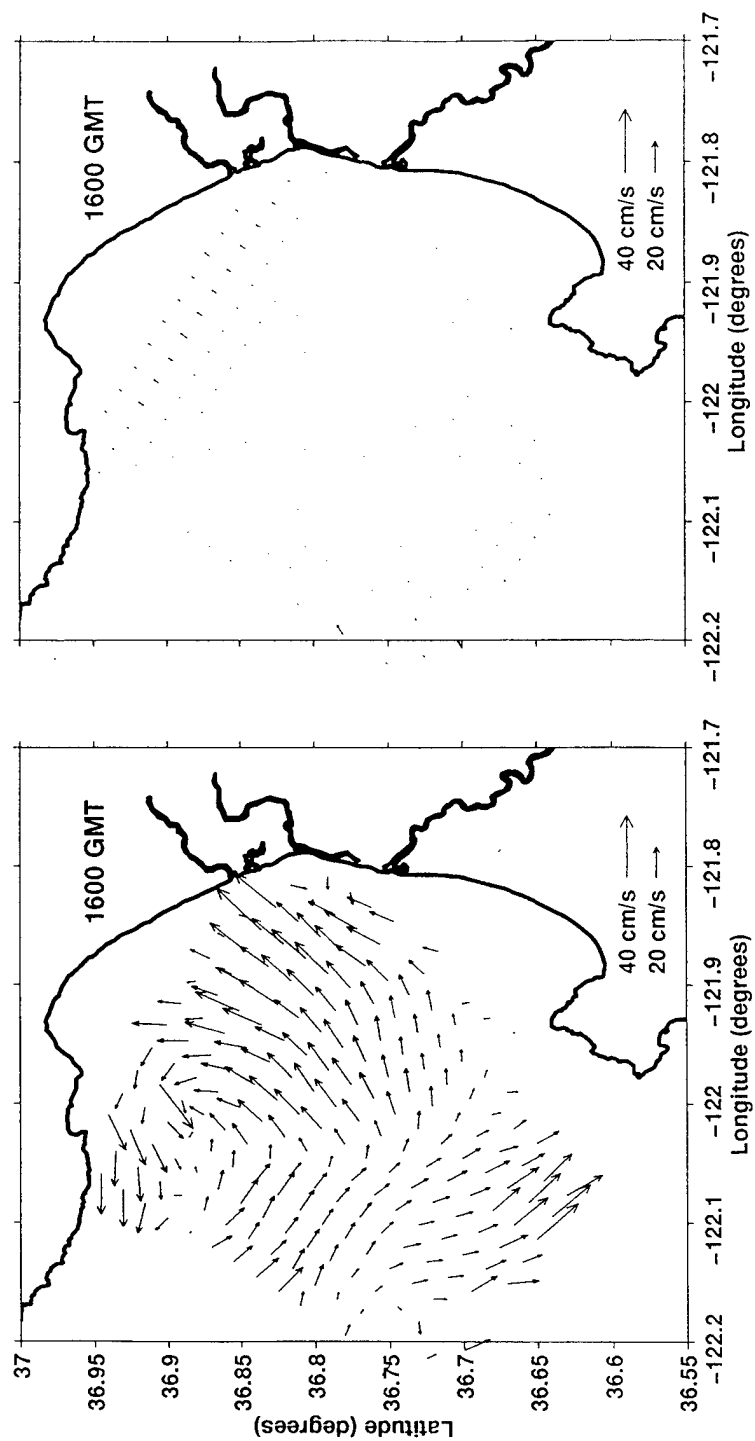


Figure 24. OSCR-derived canonical flow (left) for 1600 GMT with associated mapping error (right).

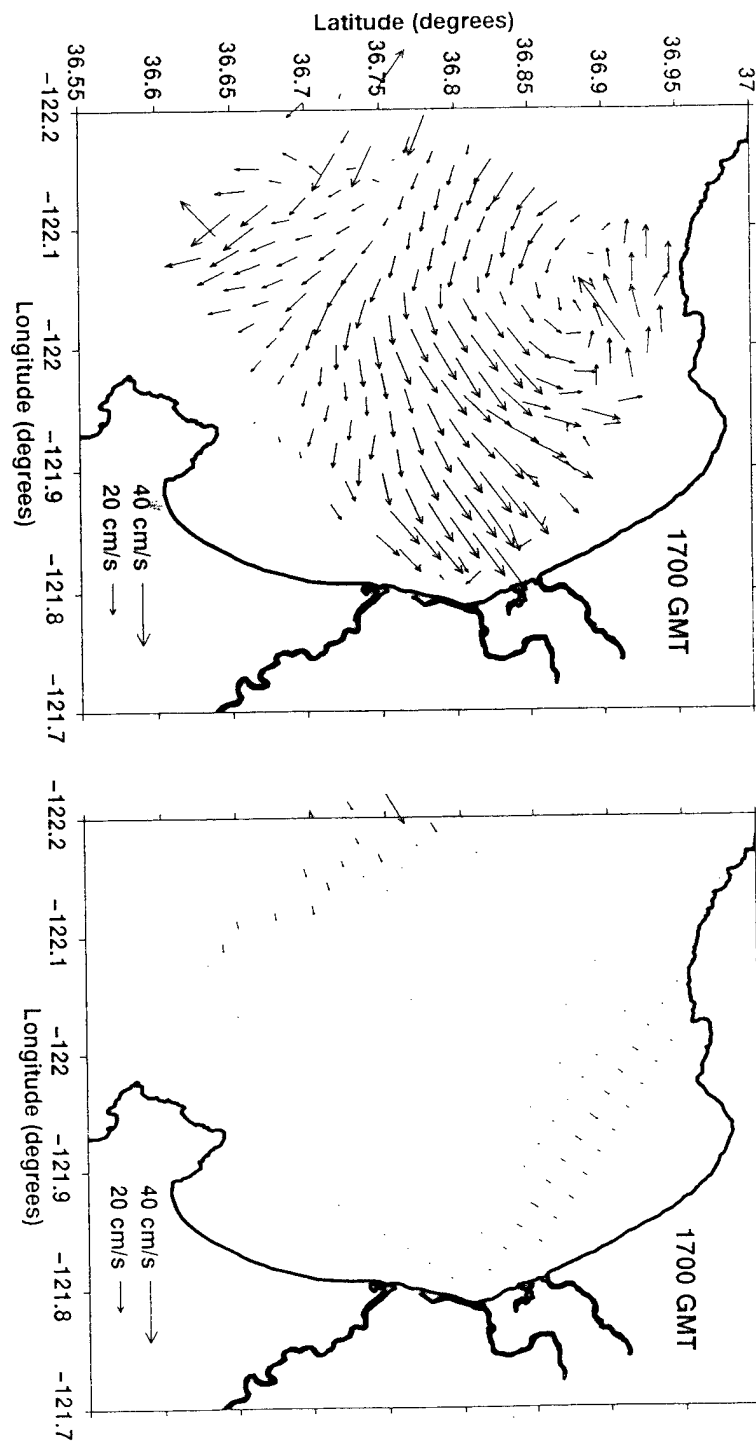


Figure 25. OSCR-derived canonical flow (left) for 1700 GMT with associated mapping error (right).

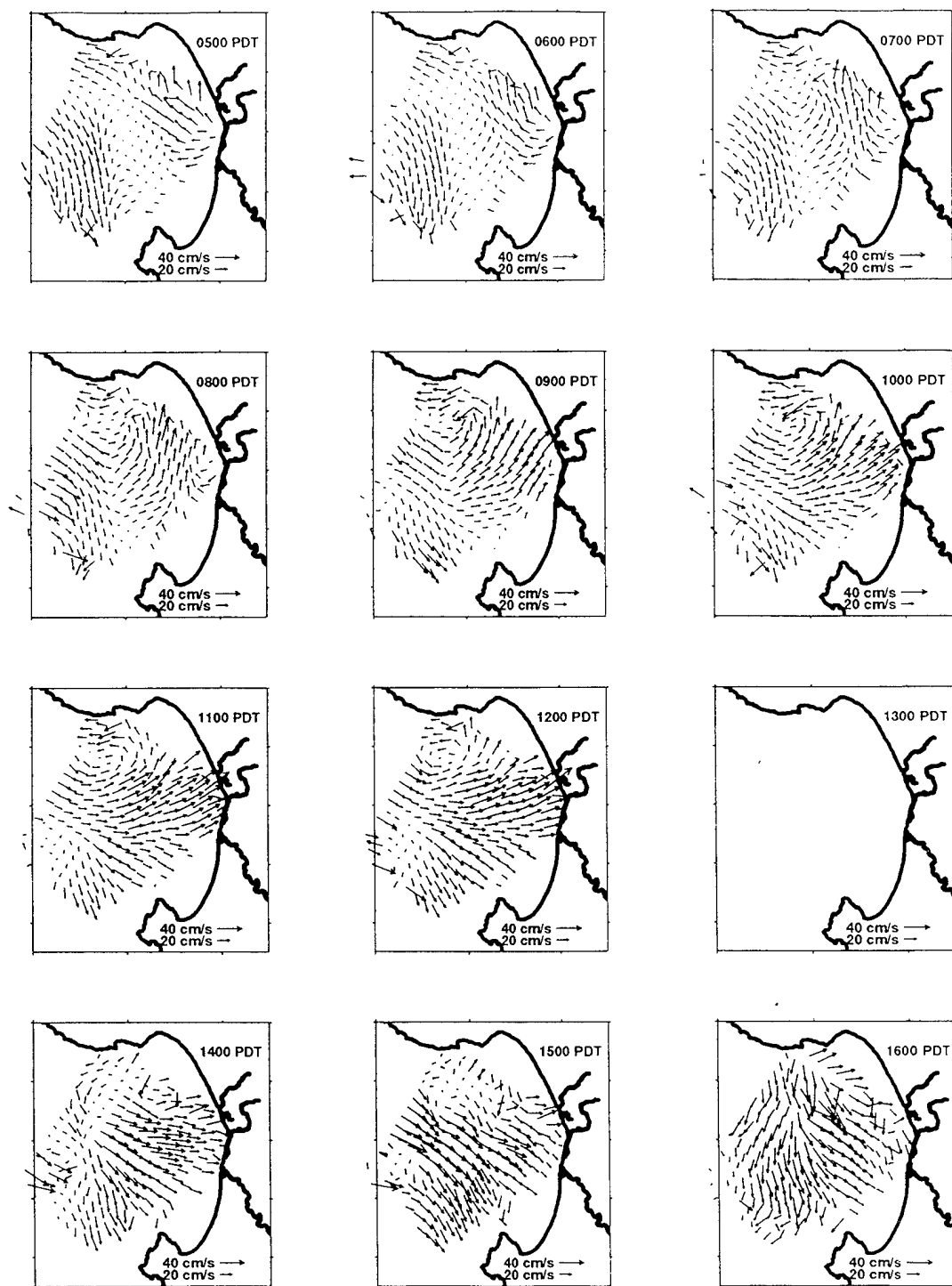


Figure 26. OSCR-derived canonical flow for 0500-1600 PDT. No valid data were collected for hour 1300.

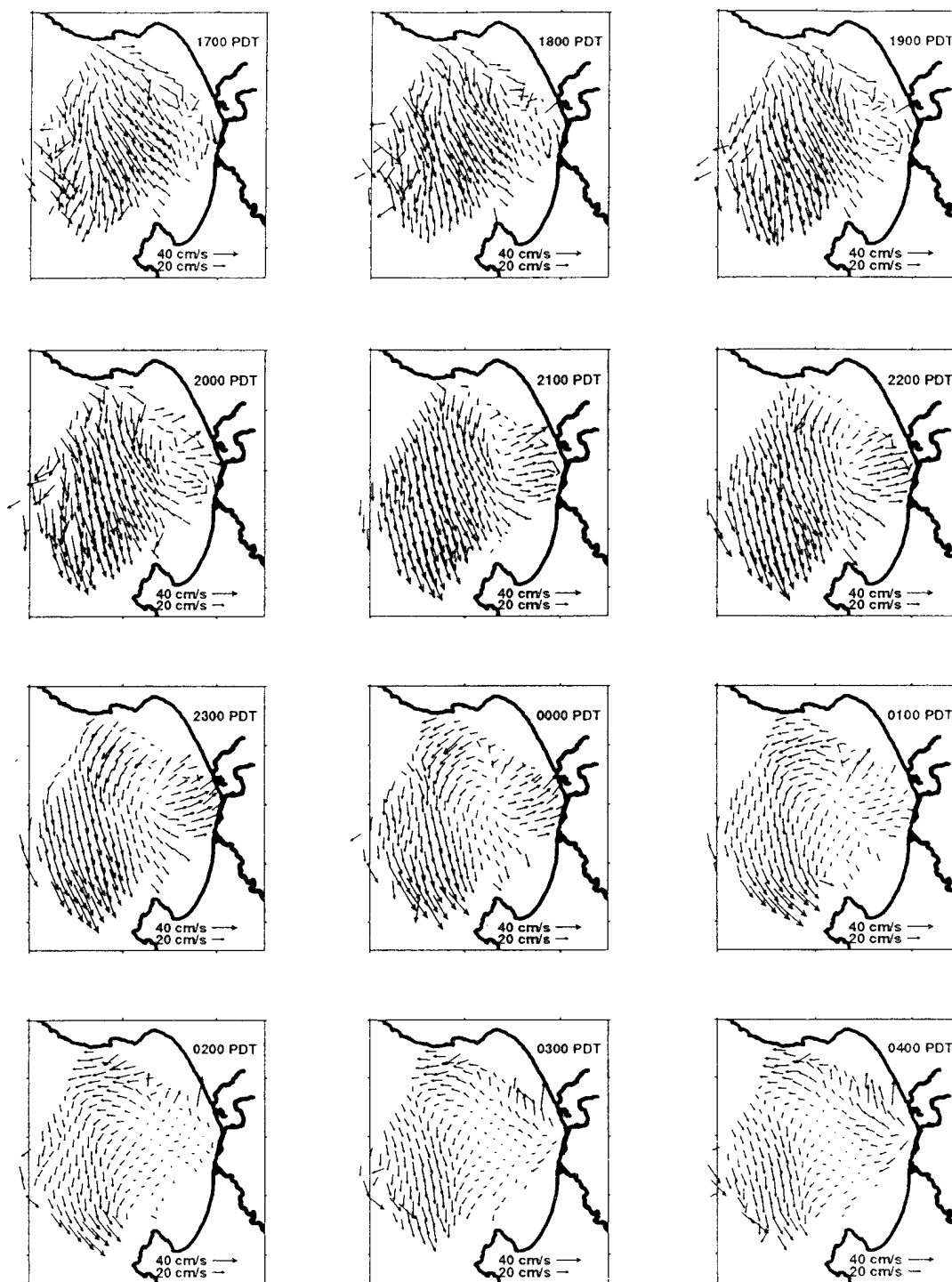


Figure 27. OSCR-derived canonical flow for 1700-0400 PDT.

III. TIDAL PERIOD FLUCTUATIONS

A. BACKGROUND

Real time tidal current predictions made possible by OSCAR may be employed in oil-spill control, search and rescue operations, extreme navigational situations and assessing the possible magnitude of flooding due to a major storm surge. Long term study and prediction of the tidal cycle and its resultant currents provide information concerning its affects on various physical and biogeochemical cycles such as plankton distribution and sediment and waste transport. Tidal height predictions as performed by tables are of very little use in these situations where the surface currents along the coastlines need to be known.

1. Tidal Constituents

The variations in the composite gravitational pull between the sun, earth, and moon, combined with periodic global variations, result in nearly 400 tidal components, or "constituents." A partial list of these constituents is presented in Table 1. A few are dominant enough that by analyzing just these, the tidal pattern may be described with a reasonable degree of accuracy. The strongest semidiurnal constituent is the principal lunar, or M2 tide. This component is a composite result of the moon's orbit around the earth and the earth's rotation about its axis. The luni-solar diurnal, or K1 tide, is the largest diurnal constituent. It is produced by those orbital motions that have periods of a lunar and a solar day interacting with those that have periods of a tropical month and a tropical year. (Werner, 1992).

The harmonic analysis of surface current measurements reveal cycles coinciding with these major tidal components. However, resolution among the many important contributing constituents depends on having an adequate time series record length to enable the isolation of those constituents with narrowly separated frequencies. Otherwise, the constituents (or other external influences) that are close in frequency may be evaluated as one constituent. Another cause of "constituent impurity" in the analysis may be the internal tide (an internal wave of tidal frequency). These are generated by the interaction of tidal sea level oscillations and bottom topography and can have a dominant influence on the tidal-period current fluctuations in many coastal regions.

TABLE 1 Partial list of principal harmonic tidal components (After Petruncio, 1993)

Name of constituent	Symbol	Period in solar hours	Coefficient ratio M2:100
<u>Semidiurnal components</u>			
Principal lunar	M2	12.42	100.0
Principal solar	S2	12.00	46.6
Larger lunar elliptic	N2	12.66	19.2
Luni-solar semidiurnal	K2	11.97	12.7
<u>Diurnal components</u>			
Luni-solar diurnal	K1	23.93	58.4
Principal lunar diurnal	O1	25.82	41.5
Principal solar diurnal	P1	24.07	19.4
<u>Long period components</u>			
Lunar fortnightly	Mf	327.86	17.2
Luni-solar fortnightly	MSf	354.37	0.9
Lunar monthly	Mm	661.30	9.1

B. HARMONIC ANALYSIS

A primary means of conducting tidal analysis utilizing vector data is to analyze, separately, two components of flow, usually the u-component, positive in the eastward direction, and the v-component, positive in the northward direction. Harmonic decomposition separates the data, using a least squares fit, into possible constituents. For each of the constituents, the flow's phase and amplitude are used to reconstruct u and v as a function of time. The total current's harmonic representation can be expressed as a complex number as follows (Godin, 1972):

$$U(t) = u_0(t) + \sum_{j=1}^N u_j \cos(\sigma_j t - \phi_j) + i[v_0(t) + \sum_{j=1}^N v_j \cos(\sigma_j t - \theta_j)]. \quad (3.1)$$

The real part of this expansion (the first two terms on the right hand side) represent the mean and periodic components of eastward flow. The imaginary part (the last two terms) represents corresponding northward flow. By letting $A_1 = u_j \cos \phi_j$, $B_1 = u_j \sin \phi_j$, $A_2 = v_j \cos \theta_j$, and $B_2 = v_j \sin \theta_j$, dropping the use of the suffix i for constituent numbering, letting $a^+ = [(\frac{A_1+B_2}{2})^2 + (\frac{A_2-B_1}{2})^2]^{1/2}$, $a^- = [(\frac{A_1-B_2}{2})^2 + (\frac{A_2+B_1}{2})^2]^{1/2}$,

$\epsilon^+ = \arctan(\frac{A_2 - B_1}{A_1 + B_2})$, and $\epsilon^- = \arctan(\frac{A_2 + B_1}{A_1 - B_2})$, and performing some algebra following Godin (1972), the contribution of the current in any specific tidal constituent can be written as:

$$U(t) = U^+(t) + U^-(t) = a^+ \exp i(\epsilon^+ + \sigma t) + a^- \exp i(\epsilon^- + \sigma t) \quad (3.2)$$

$$= \exp[i(\frac{\epsilon^+ + \epsilon^-}{2})] \{ (U_{maj}) \cos((\frac{\epsilon^+ - \epsilon^-}{2}) + \sigma t) + i(U_{min}) \sin((\frac{\epsilon^+ - \epsilon^-}{2}) + \sigma t) \}. \quad (3.3)$$

It may be seen in Equation (3.2) that this contribution consists of two vectors, $U^+(t)$, and $U^-(t)$. The angular rotation speed of each is σ cycles per hour. The first vector has length a^+ , counterclockwise rotation, and is ϵ^+ radians counterclockwise from the positive X axis (east/west) at time $t=0$; the second vector's length is denoted by a^- , which rotates clockwise, and is at ϵ^- radians counterclockwise from the positive X axis at $t=0$. The composite vector $U(t)$ will rotate in the counterclockwise direction if $a^+ > a^-$, clockwise if $a^+ < a^-$, and linearly if $a^+ = a^-$. Equation 3.3, applied from time zero to $2\pi/\sigma$, shows that the path of the composite vector traces an ellipse, or if moving linearly, a line segment, whose respective semi-major (U_{maj}) and semi-minor (U_{min}) axis lengths are $a^+ + a^-$ and $a^+ - a^-$, and whose angle of inclination, in the clockwise direction from the positive X axis is $(\epsilon^+ + \epsilon^-)/2$ radians.

The tidal current ellipses exhibit 180° ambiguity with respect to the angle of inclination, as this angle indicates the offset from due east for either end of the semi-major axis. The true position of the tidal current vector for a given point in time will indicate the same direction regardless of which end of the semi-major axis is selected as the reference, but the angle describing the ellipse inclination and current vector phase may change by 180°, again depending upon the chosen axis end (Petruncio, 1993). This ambiguity should be kept in mind while evaluating the phase angles of the tidal current constituents. An illustration of the tidal ellipse is presented in Figure 28.

C. OBSERVATIONS

Tidal current ellipses were derived using the harmonic analysis package of Foreman (1978). As the sample record was less than three days long, only a few tidal constituents were resolved, and only two (M2 and K1) were strong enough to be resolved with any confidence regarding their accuracy. For the M2 and K1 constituents, grid points with less than 85 percent temporal coverage were discarded.

Plots were made of the M2 and K1 current ellipses in order to show the spatial pattern of the fluctuations in Monterey Bay. The mapping routine was similar to that used by Petruncio (1993), with an additional correction for the Mercator projection's "stretching" in the longitudinal direction. In each plot, vectors on each ellipse were included to represent the direction of the surface current during the time of high tide for that constituent. These vectors will be referred to as "phase vectors."

1. Elliptical Description and Definition

Based on their size and shape, the ellipses contain various degrees of validity when presenting certain information. For instance, when evaluating the direction of rotation an ellipse that is shaped similar to a circle will be more reliable than an ellipse that is shaped like a line. Relative size may also be an indication of the degree of information ambiguity, with a larger size indicating lesser ambiguity. Therefore, size and shape descriptors are given. Full is defined as having greater than 75% semi-minor to semi-major axis ratio, and substantial as having a velocity greater than 5 cm/sec. Flat (~linear) ellipses may be described as those whose semi-minor axis is insignificant in comparison with the semi-major axis, which I describe as possessing less than a 20% semi-minor to semi-major axis ratio. Median ellipses are those in between the above axis ratios.

2. M2 Constituent

a. Descriptive

The M2 ellipse plot (Figure 29) displays the orientation and strength of tidal currents throughout the tidal cycle. The major axis direction of those ellipses that are to the north and south of the canyon is across the slope of the shelf, while those over the canyon at the shallow end have axes that are oriented along the canyon axis direction and those at the deeper end are oriented across the canyon axis. The current strength is significantly amplified at the head of the canyon, dropping off approximately 10 km from the canyon mouth. There is a gradual increase in strength beyond the 1000 m contour towards the southwestern end of the mapping grid. Amplification is also evident at the northern end of

the bay between the shoreline and the 50 m contour. These areas also contain substantial, full ellipses. There are other groups of relatively full ellipses. These are located at 36.69° N, 121.97° W and 36.84° N, 122.08° W.

These findings are in agreement with CODAR measurements made over several extended periods. The velocity intensification at the head of the canyon is clearly depicted in Petruncio's (1993) M2 ellipse patterns, although his area of coverage was somewhat limited, covering only 36.68-36.85° N and 122.05-121.82° W, due to the older CODAR system in place at that time. These were produced from a month long data record taken in September 1992. More recently, measurements were taken over August 1994 with a larger updated CODAR system (Paduan et al., 1995). Using three stations, a much larger area of coverage was produced (Figure 30). The similarity between the OSCR data and this data extends to include the amplification of ellipses both to the south of Santa Cruz and to the northwest of the Monterey Peninsula.

b. Current Rotation

The current vector rotation for the M2 constituent is represented in Figure 31. The rotation of the M2 current vectors is predominantly clockwise (-) in the inland portion of the grid, and predominantly counterclockwise (+) at the seaward side. Asterisks indicate that the ellipse had less than a 20% axis ratio, and thus were ambiguous about the direction of rotation.

c. Division of Tidal Periods

Further inspection of the M2 constituent's tidal current cycle was conducted by plotting current vectors that corresponded with high tide, low tide (high tide plus 180°), flood (high tide plus 270°, and ebb tide (high tide plus 90°). Figures 32 through 35 contain plots in which the ellipses have been removed and only phase vectors remain. These indicate the four stages of a tidal cycle.

At high tide the M2 constituent (Figure 32) flows westward, or down-canyon, near the head of the canyon. There is downslope flow along the flanks of the canyon, with higher magnitudes over the steepest contours, resulting in an area of convergence down the center of the bay. The downslope pattern holds true for most of the bay but is discontinuous near the western and northwestern areas of the grid.

In Figure 33, the M2 tide ebbs with weakened canyon-mouth currents shifting southward. The southern flank downslope flow remains as such (towards the west, then turning north), but the trend towards the north continues across the canyon, up the northern flank, then turning slightly to the east at the northeastern edge of the grid. This

results in a spatial pattern of clockwise flow in the inland portion of the bay and flow towards the northwest to seaward.

At low tide (Figure 34) the current near the head of the canyon is heading northeast, or up the canyon. Between 122°W and 122.1°W , to the south of Santa Cruz, there is a northward flow up the Soquel Canyon axis. That flows weakens and turns westward at the 50 m contour.

As the M2 tide floods (Figure 35), there is a strong southward-directed flow from the area south of Santa Cruz, following a cross-canyon path, with the pattern apparently continuing south past the Monterey Peninsula. On the western edge of this pattern, however, there is some weak divergent flow that points towards the east up the southern flank, and continues to turn counterclockwise spatially until it is heading in a northward direction near the head of the canyon.

3. K1 Constituent

a. Descriptive

The K1 ellipses (Figure 36) are uniformly oriented in the northwest-southeast direction within the bay and shift slightly to a northeast-southwest orientation along the northwest edge of the grid. The current magnitudes are generally uniform to the north and south and can be described as being in three regimes from east to west. The first regime, nearest to land, consists of relatively small ellipses, uniformly oriented in direction. These are on the same order of magnitude, or smaller than, the M2 ellipses. The second area is in the interior of the grid running between Santa Cruz and the Monterey peninsula. They tend to be stronger than the M2 currents, in many cases over twice as strong. The largest ellipses are in the center of the bay, approximately 11.5 to 23 km offshore. For these two areas, the semi-minor axes of the ellipses are generally substantial in comparison to the semi-major axes, with the fullness increasing towards the center of the second regime until the ellipses resemble circles. The third regime is located near the western side of the grid, and consists of flat ellipses that display three different orientations. Directly to the south of Santa Cruz, the ellipses are oriented northwest-southeast. South of 36.9°N until 36.75°N they are oriented northeast-southwest. South of 36.75°N , they are oriented northwest-southeast again.

b. Current Rotation

The rotation of the K1 tidal current vectors is presented in Figure 37. There is a predominance of clockwise rotation up to an approximate radius of 28 km from the mouth of the canyon. To seaward of this area, the rotation is generally counterclockwise or

ambiguous in its direction. The delineation between the two areas is coincident with the area of flat or "non-directionally robust" current ellipses described above.

c. Division of Tidal Periods

A tidal phase breakdown similar to that of M2 is presented here for the K1 tidal cycle. At high tide the K1 flow is predominantly southward at a generally high intensity. The flow vectors are maximum near the northern corner of the grid and minimum near the eastern corner of the grid (Figure 38). As the tide ebbs, flow in the northern and eastern portions of the bay turns towards the east. Near the southwestern side of the grid, there is a transition to a northwest flow of approximately one half of the magnitude of the flow towards the southeast (Figure 39). At low tide (Figure 40) the flow is similar to that at high tide but with the general direction being to the north. Again the maximum magnitude is near Santa Cruz and the minimum is near the head of the canyon. Figure 41 presents the flood tide phase. The majority of the bay contains flow to the northwest with magnitudes reaching approximately 20 cm/sec.

D. ANALYSIS

1. Semidiurnal Cycle

The dominant tidal sea level constituent for the Monterey Bay surface waters is M2. However, the extreme topography of the Monterey Bay canyon manifests itself in the surface currents as well. The observed current pattern, therefore, is the result of a complex interaction between various factors. One of these, and perhaps the largest contributor, is an internal tidal wave. Other papers have presented various evidence, in addition to surface current characteristics, confirming the existence of the internal tide (Broenkow and Smethie, Jr., 1978; Shea and Broenkow, 1982; Petruncio, 1996). The data produced by OSCAR demonstrates several traits indicative of internal tide activity within the bay.

2. Internal Tide Indications

a. Ellipses

The M2 ellipse plot (Figure 29) demonstrates the effect of the Monterey Bay's bathymetry on the alignment of the ellipses in that those to the north and south of the canyon are directed down the slope of the shelf, while those over the canyon at the shallow end are oriented in the along-axis direction and those at the deeper end are oriented in the across-axis direction. The increase in current strength at the head of the canyon is indicative

of a focusing of the wave energy caused by the narrowing and shoaling of the canyon (Shea and Broenkow, 1982).

b. Direction of Rotation

Currents produced by the barotropic M2 constituent are expected to rotate in the counterclockwise direction as they are influenced by the poleward propagating Kelvin wave (Munk, Snodgrass and Wimbush, 1970). The trend of rotation (Figure 33), however, in the Monterey Bay is divided. To seaward of this division, in an area expected to be less affected by the internal tide, the rotation is counterclockwise. Landward of this line, inside the bay, the rotation is primarily clockwise. This is the expected rotation of an internal wave (Gill, 1982). However, evidence of bathymetric steering of the rotation patterns (with oppositely rotating ellipses north and south of the canyon axis) as discussed by Petruncio (1993) is not found in this two and a half day record.

c. Amplitude

The M2 barotropic cross-shore amplitude has been found to be roughly 0.5 cm/sec (Petruncio, 1996). The amplitudes found in Figure 29 are significantly larger, indicating the influence of non-barotropic forcing such as internal wave movement.

d. Direction of Flow

Final evidence of the influence of the internal tide exists in the direction of flow as indicated by Figures 32 through 35. In this study, measurements comparing the OSCAR-derived ellipses and sea level heights indicate that the M2 currents at the canyon head lag the sea level response by approximately 5 hours, 20 minutes (160°). This results in a surface flow that appears contrary to what would be expected from the sea surface height change. This replicates Petruncio's (1993) findings, except that his phase lag was determined to be 4 hours. Several explanations can be made for this difference. The most likely is that internal tides are variable with time and are not coupled with the barotropic tidal cycle as noted by Sandstrom (1991). In Monterey Bay, significant variations in the internal tide ray paths were observed by Petruncio (1996) between April and October that were due to seasonal changes in the stratification. It is also true that the time period used in this study is extremely short in comparison to the month-long period used by Petruncio (1993), which reduces the certainty of the phase estimates determined in this study.

e. Influence of Generation Site

Due to both the high current intensity and clockwise direction of rotation, it may be inferred that the internal tide is the cause of the full ellipses at the head of the canyon and in the northern area surrounding 36.84° N, 122.08° W (Figure 29). Seaward of

this region are found lesser current strengths and a counter-clockwise direction of rotation (that which would be expected from a barotropic tidal influence). This area is, presumably, directly above the internal wave's deep generation site and, therefore, a weak (nodal) area is expected at the surface because the sloping internal wave ray paths do not intersect the surface there. A cross section of Monterey Bay showing likely internal wave ray paths, as modeled by Petruncio (1996), illustrates this effect (Figure 42). At the surface, strong semi-diurnal currents are expected both seaward and shoreward of the bottom generation site, but not directly above it.

3. Diurnal Cycle

As seen in Table 1, the size of the K1 tidal constituent should be approximately 58% of the M2 constituents size. Clearly this is not the case. Figures 37 and 38 indicate that the surface current forcing is not due to tidal flow. I believe that the forcing that generated the ellipses in Figure 36 is composed primarily of two forces, one major and the other, relatively minor. The direction, intensity and uniformity of the ellipses indicate that winds with a fluctuation cycle similar to that of the K1 tidal constituent (~24 hours) may be the primary forcing mechanism. Hence, the seabreeze and its influence is discussed next. The presence of a secondary forcing influence is indicated by the rather constant spatial division in ellipse characteristics. This area of division runs from the upper third of the northwest side of the grid (south of Santa Cruz) to near the southern corner of the grid (just off of the Monterey Peninsula). The forcing affects the surface current pattern to seaward of the line of division. This forcing is possibly a mesoscale meander in the California Current. The fluctuation would affect the entire three-day measurement period and not be averaged out when calculating the mean current flow.

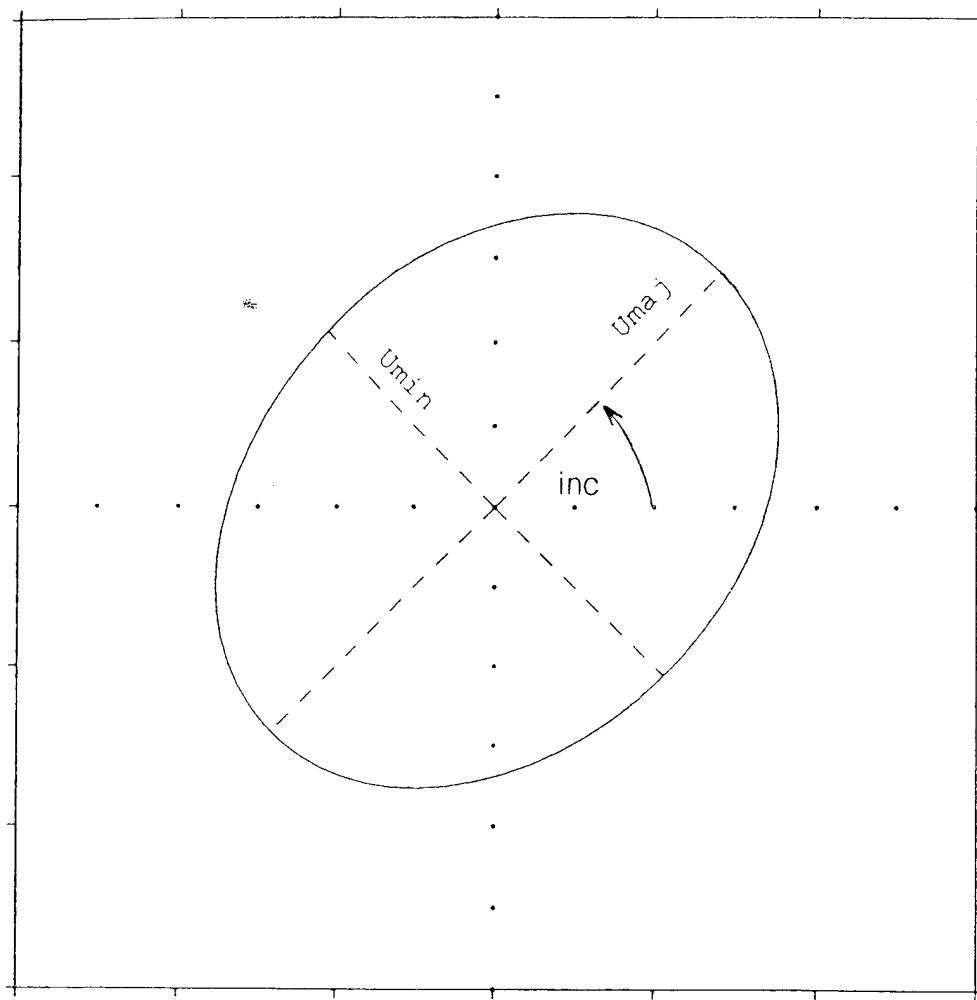


Figure 28. Tidal Ellipse with an inclination of 45° (from Petruncio, 1993).

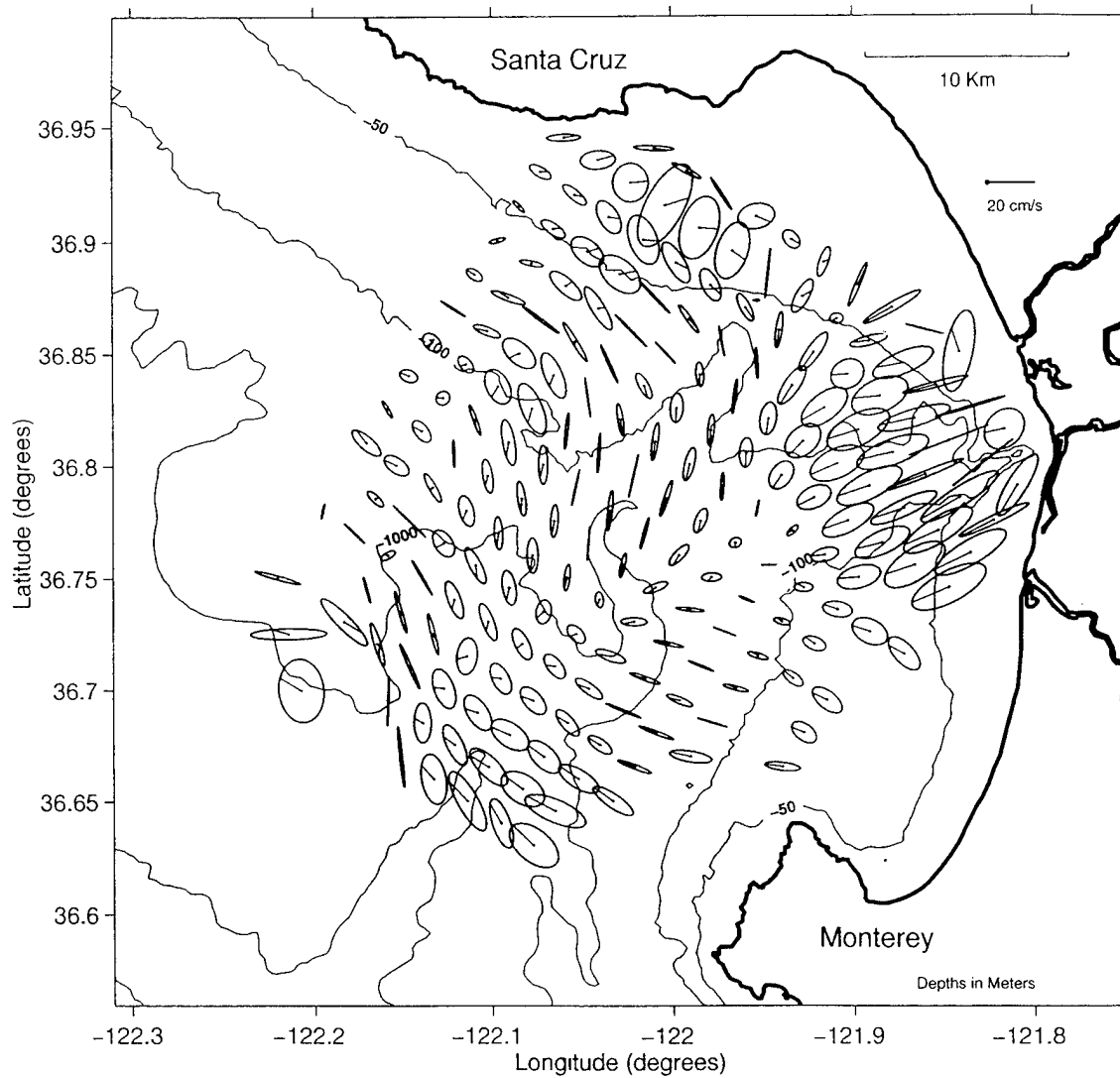


Figure 29. OSCAR-derived semidiurnal period (M2) surface current ellipses, 6-8 May, 1995. The 50 m, 100 m, 1000 m and 2000 m bathymetry contours are also depicted.

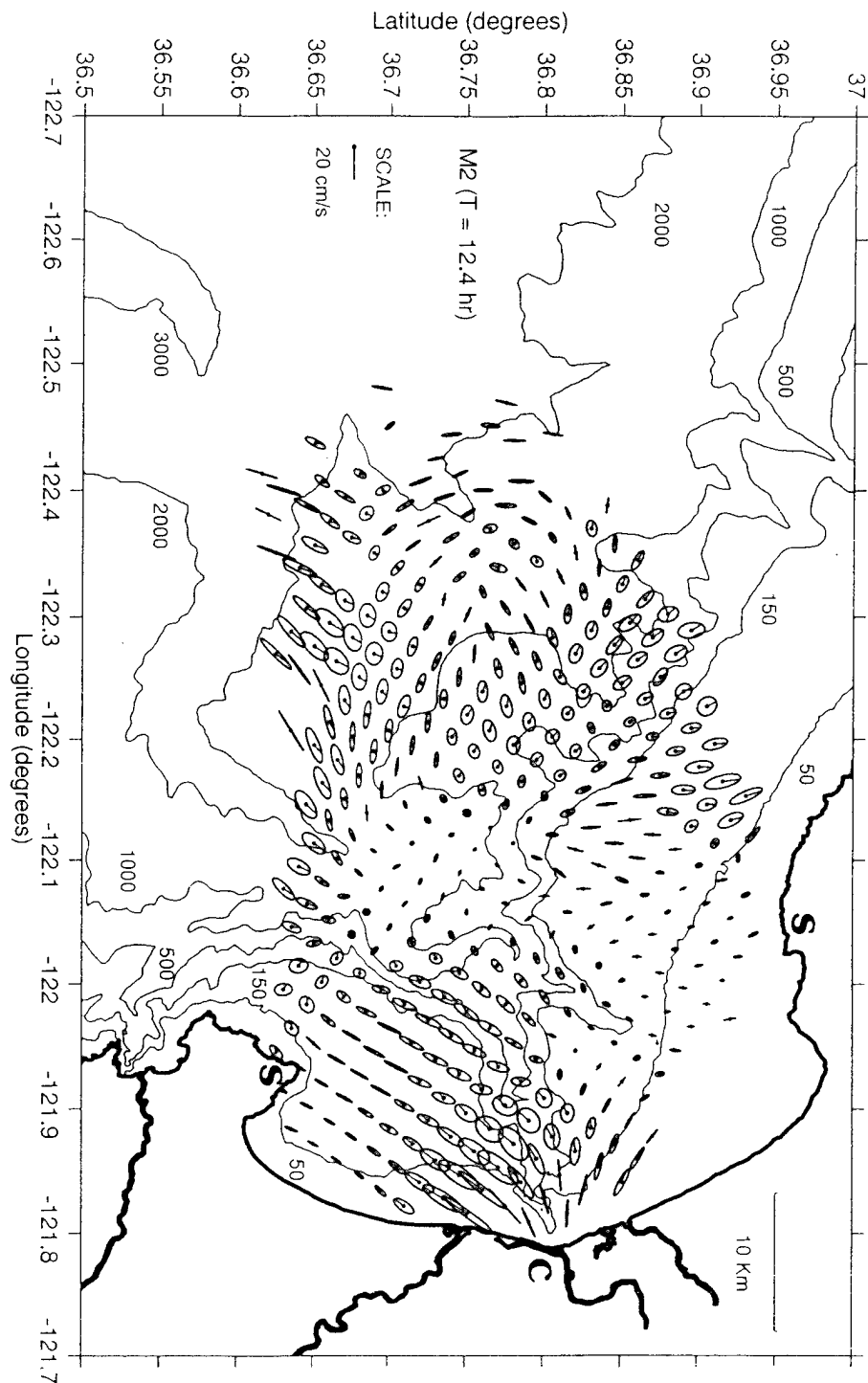


Figure 30. CODAR-derived M2 surface current ellipses, August, 1994. Locations of the two SeaSonde systems (S) and the single CODAR system (C) are denoted by symbols along the shoreline (from Paduan et al., 1995).

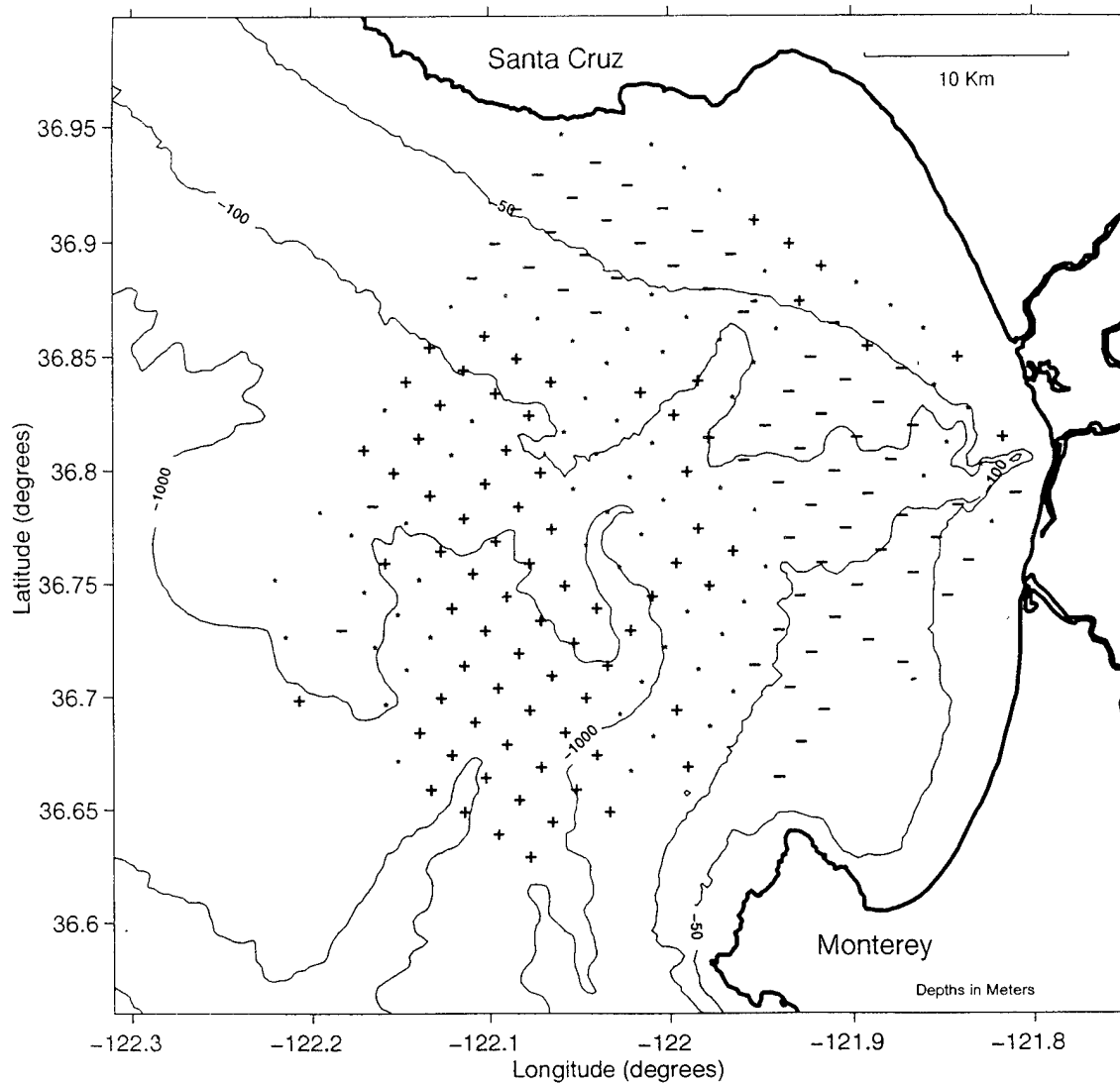


Figure 31. Direction of M2 current rotation ('-' = clockwise, '+' = counterclockwise).

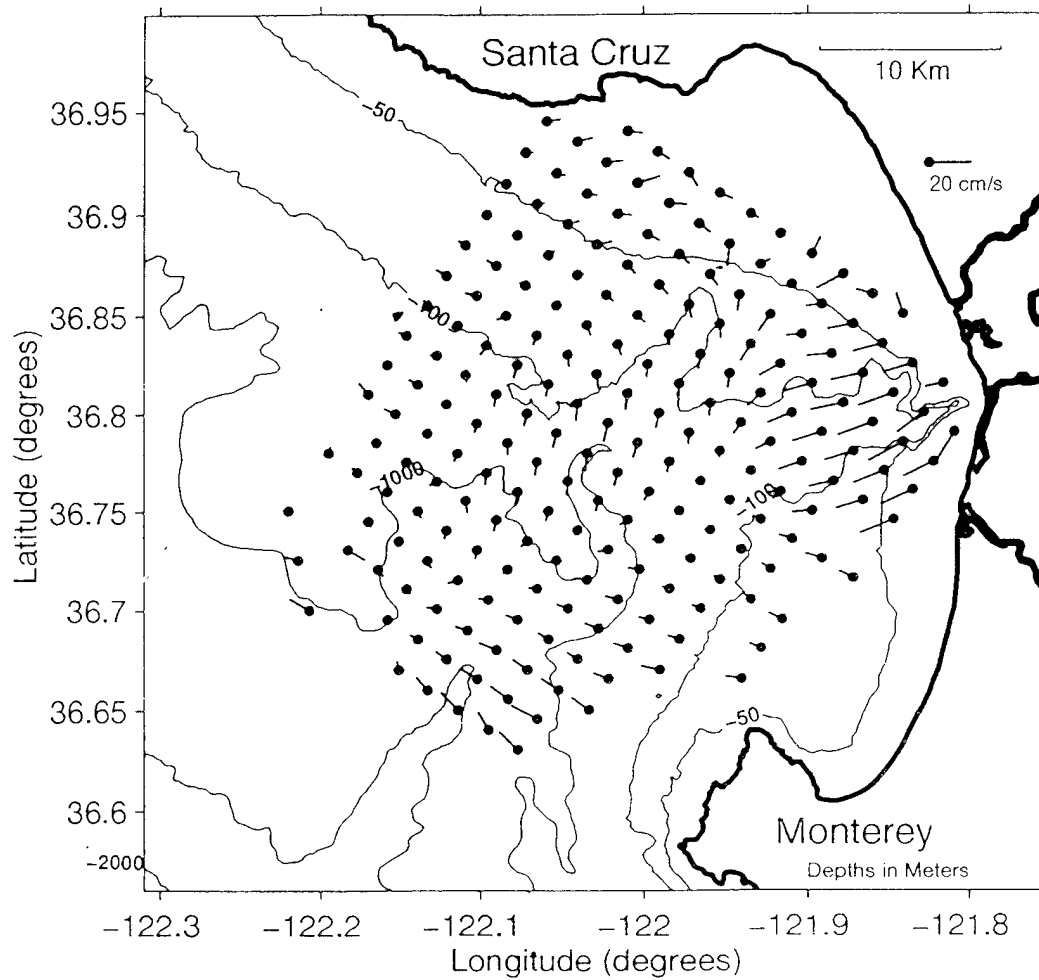


Figure 32. M2 surface current flow during high M2 tide. Gridpoint position is indicated by the dot, flow direction is indicated by the line.

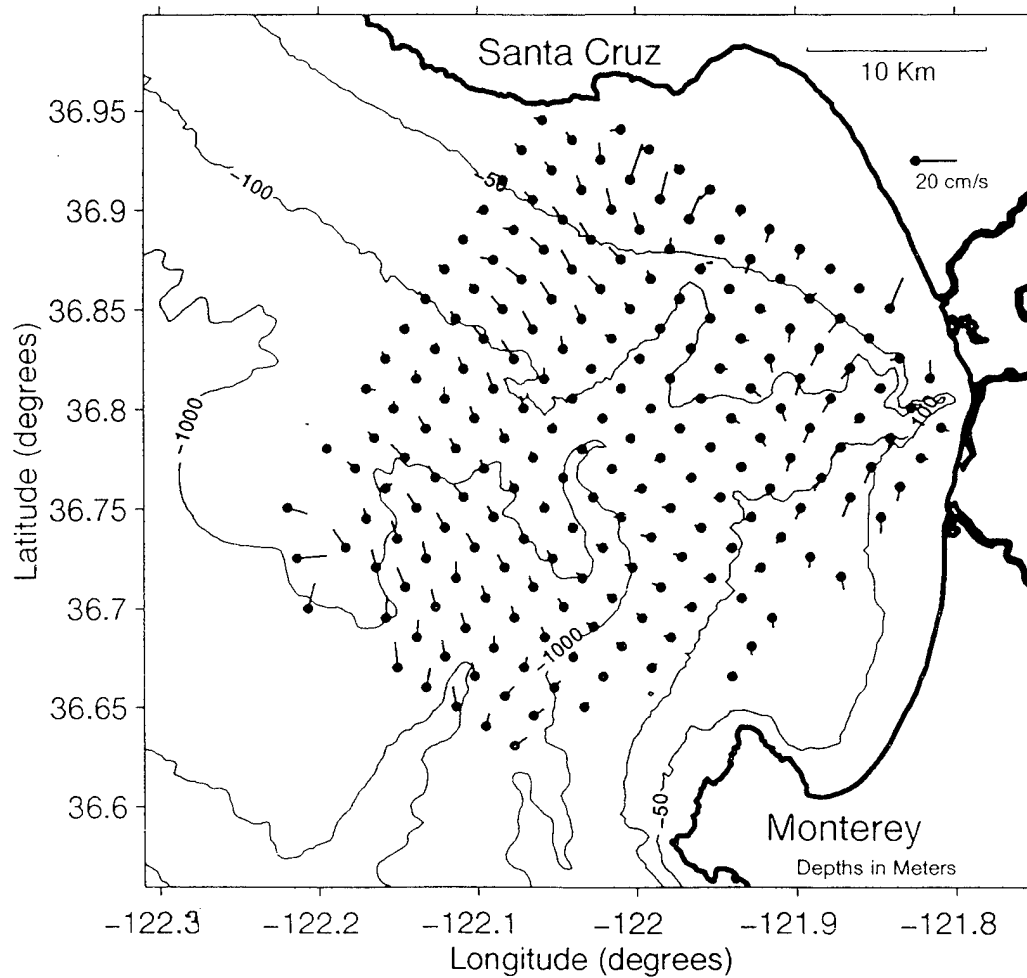


Figure 33. M2 surface current flow during ebb M2 tide. Gridpoint position is indicated by the dot, flow direction is indicated by the line.

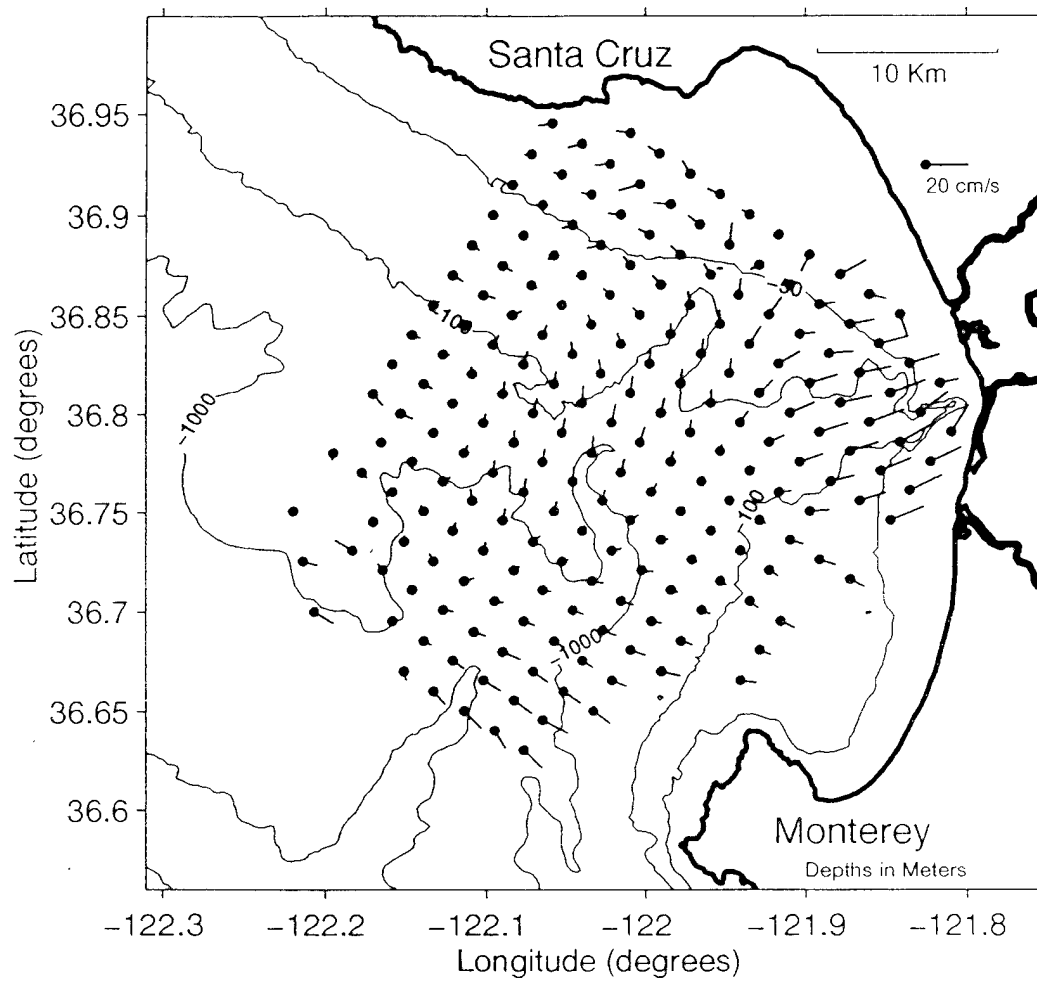


Figure 34. M2 surface current flow during low M2 tide. Gridpoint position is indicated by the dot, flow direction is indicated by the line.

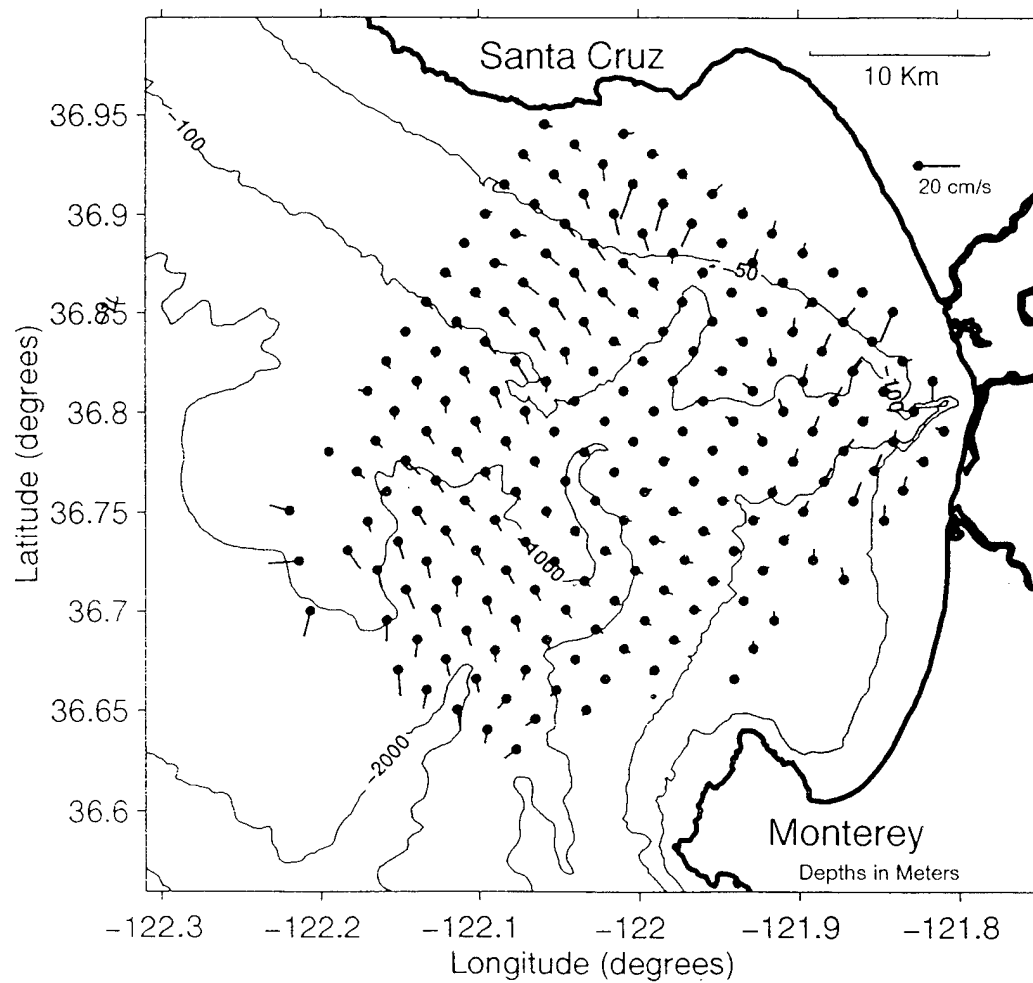


Figure 35. M2 surface current flow during flood M2 tide. Gridpoint position is indicated by the dot, flow direction is indicated by the line.

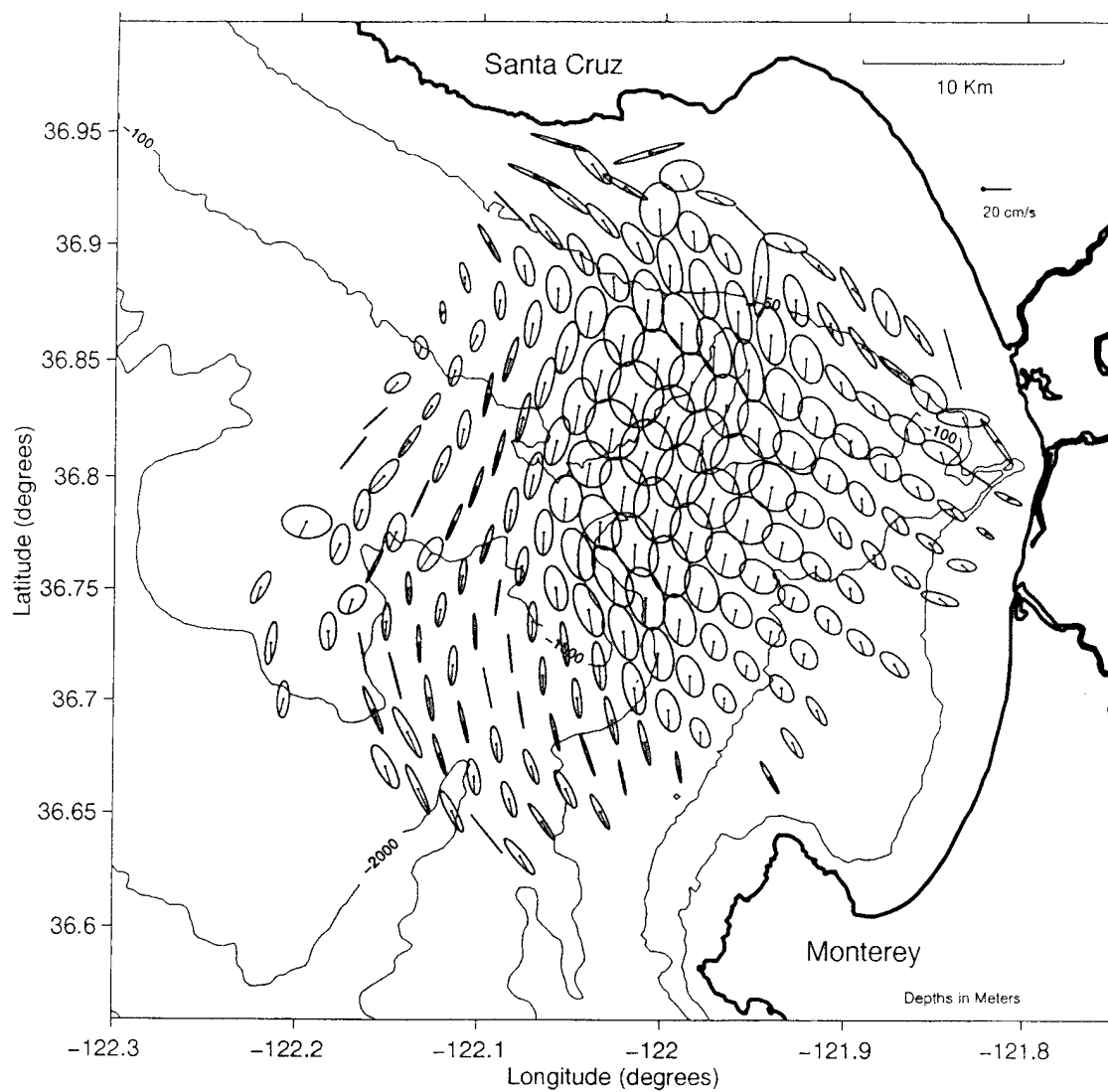


Figure 36. OSCR-derived diurnal period (K1) surface current ellipses, 6-8 May, 1995. The 50 m, 100 m, 1000 m and 2000 m bathymetry contours are also depicted.

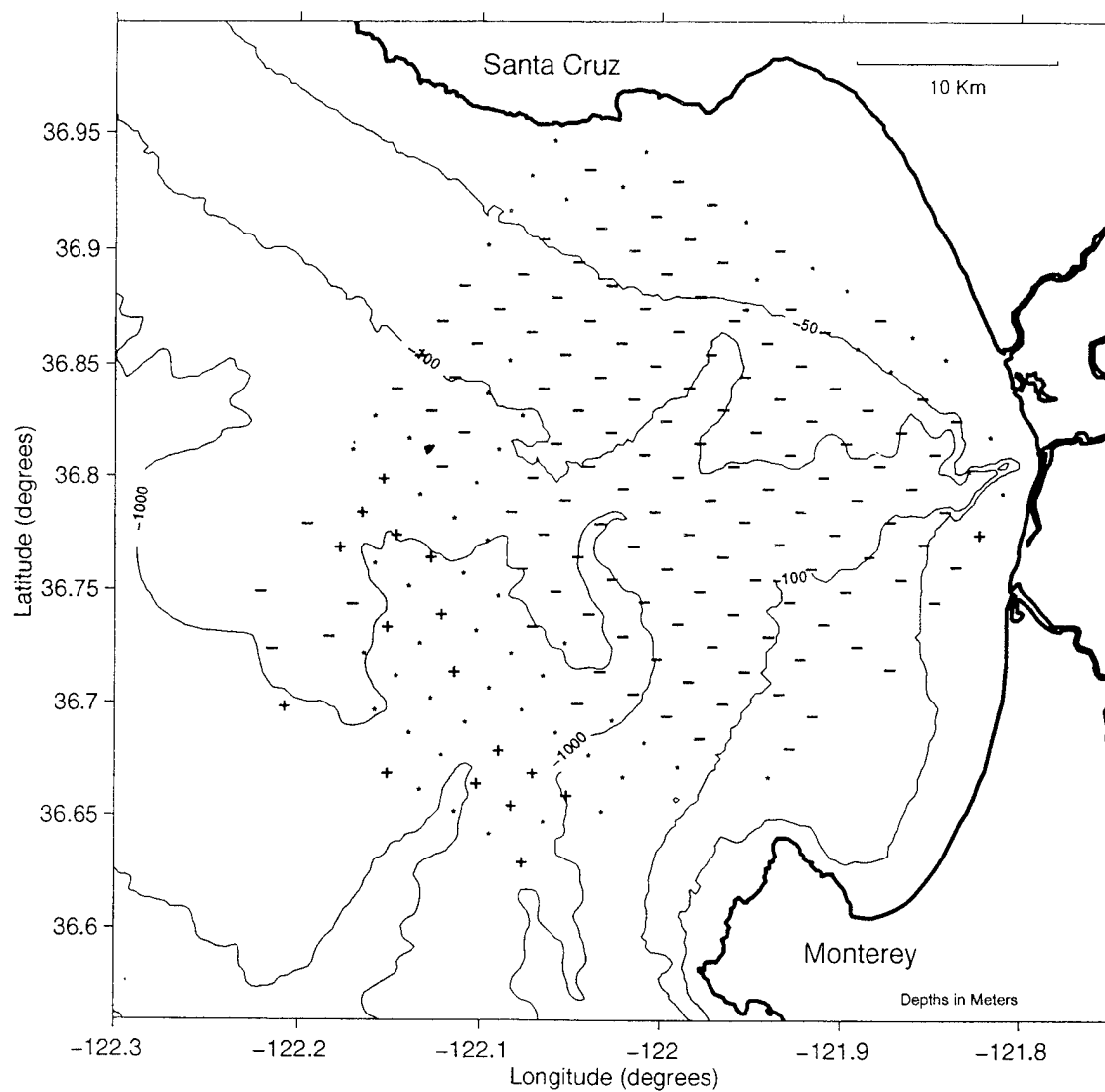


Figure 37. Direction of K1 current rotation ('-' = clockwise, '+' = counterclockwise).

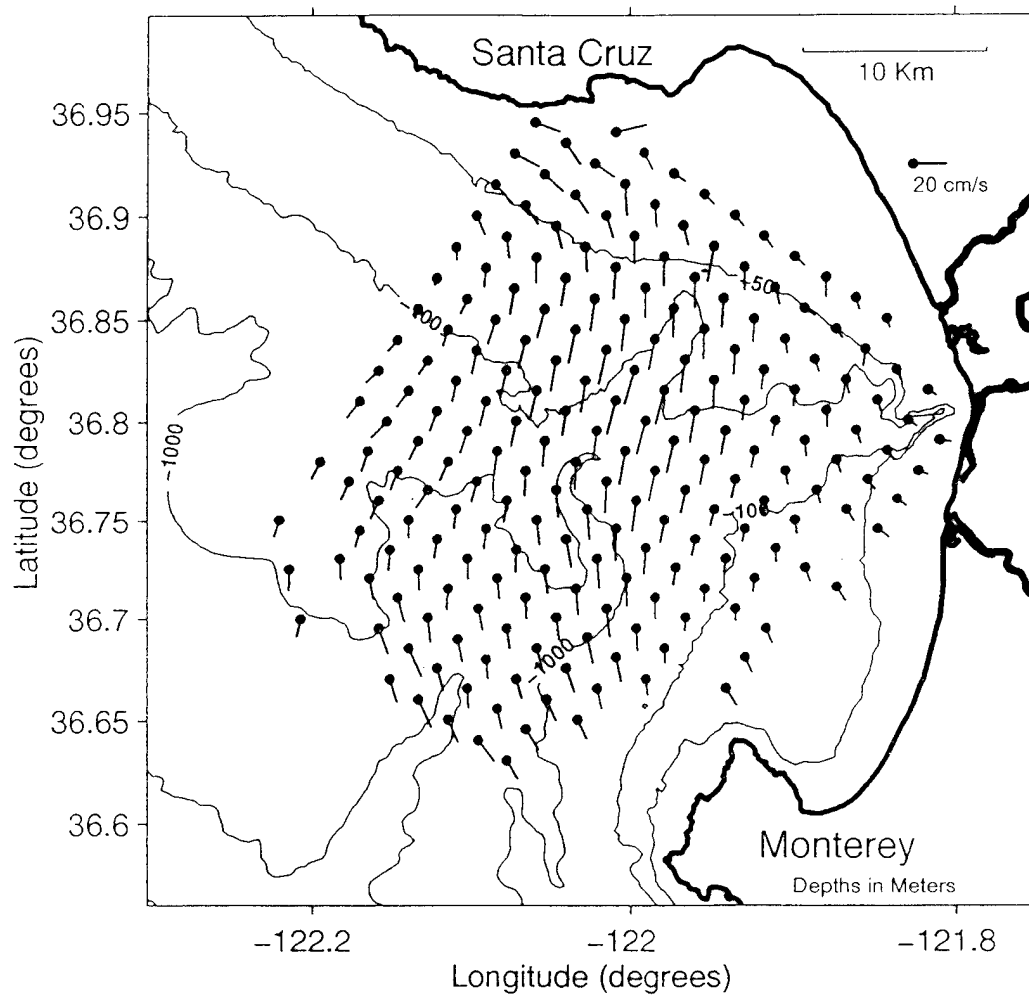


Figure 38. K1 surface current flow during high K1 tide. Gridpoint position is indicated by the dot, flow direction is indicated by the line.

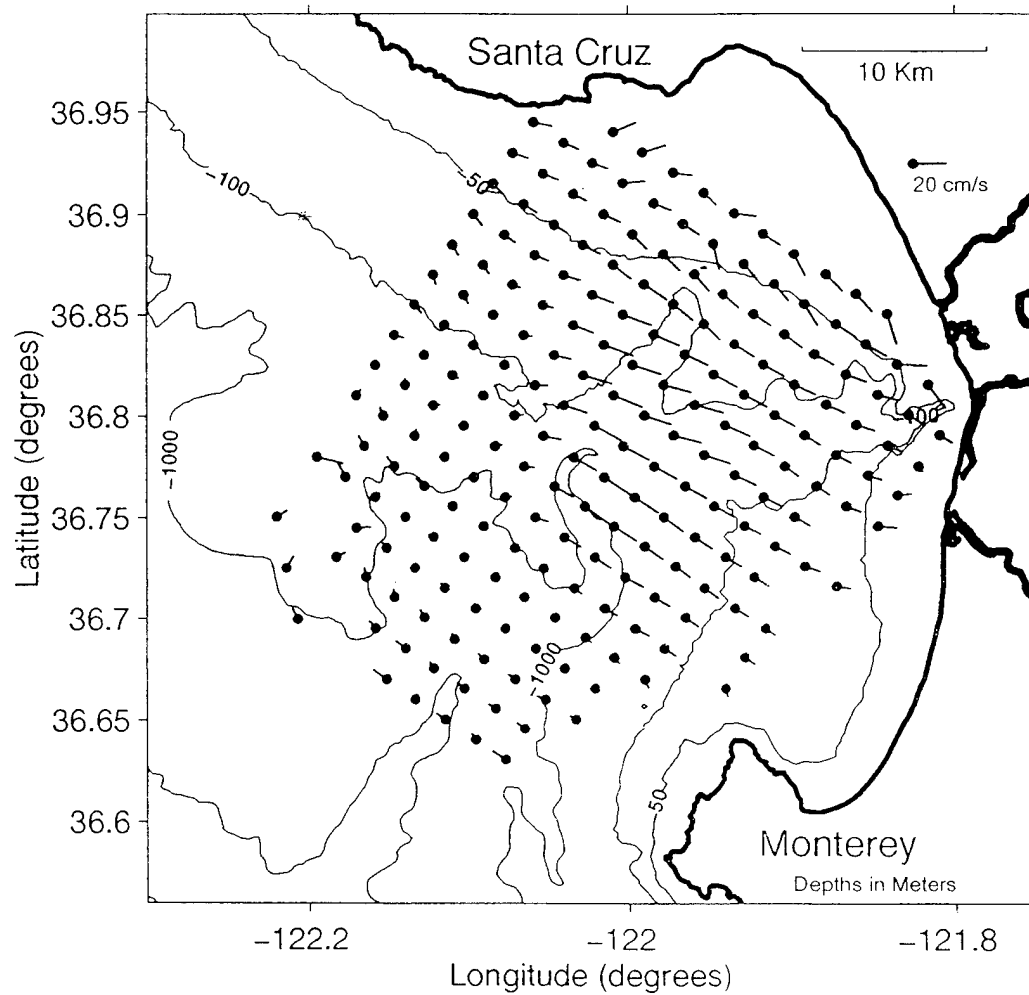


Figure 39. K1 surface current flow during ebb K1 tide. Gridpoint position is indicated by the dot, flow direction is indicated by the line.

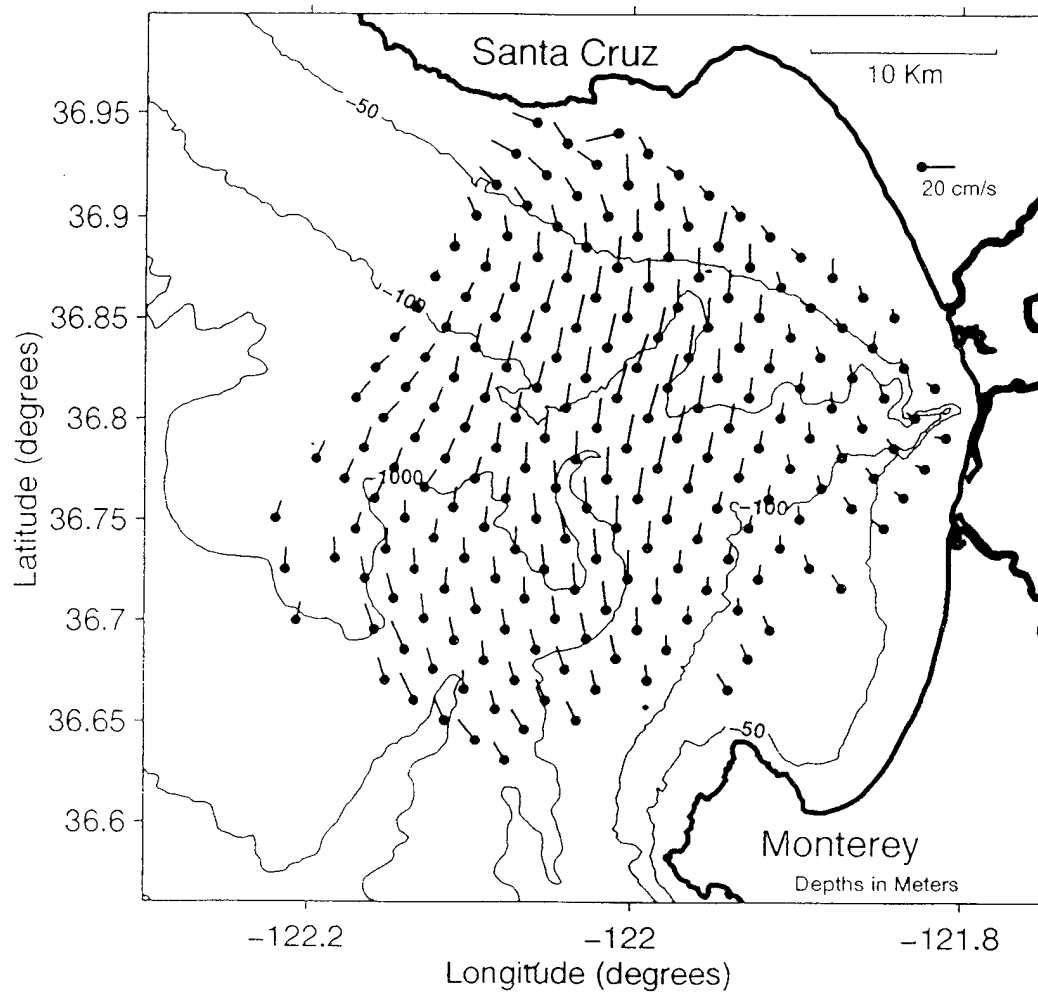


Figure 40. K1 surface current flow during low K1 tide. Gridpoint position is indicated by the dot, flow direction is indicated by the line.

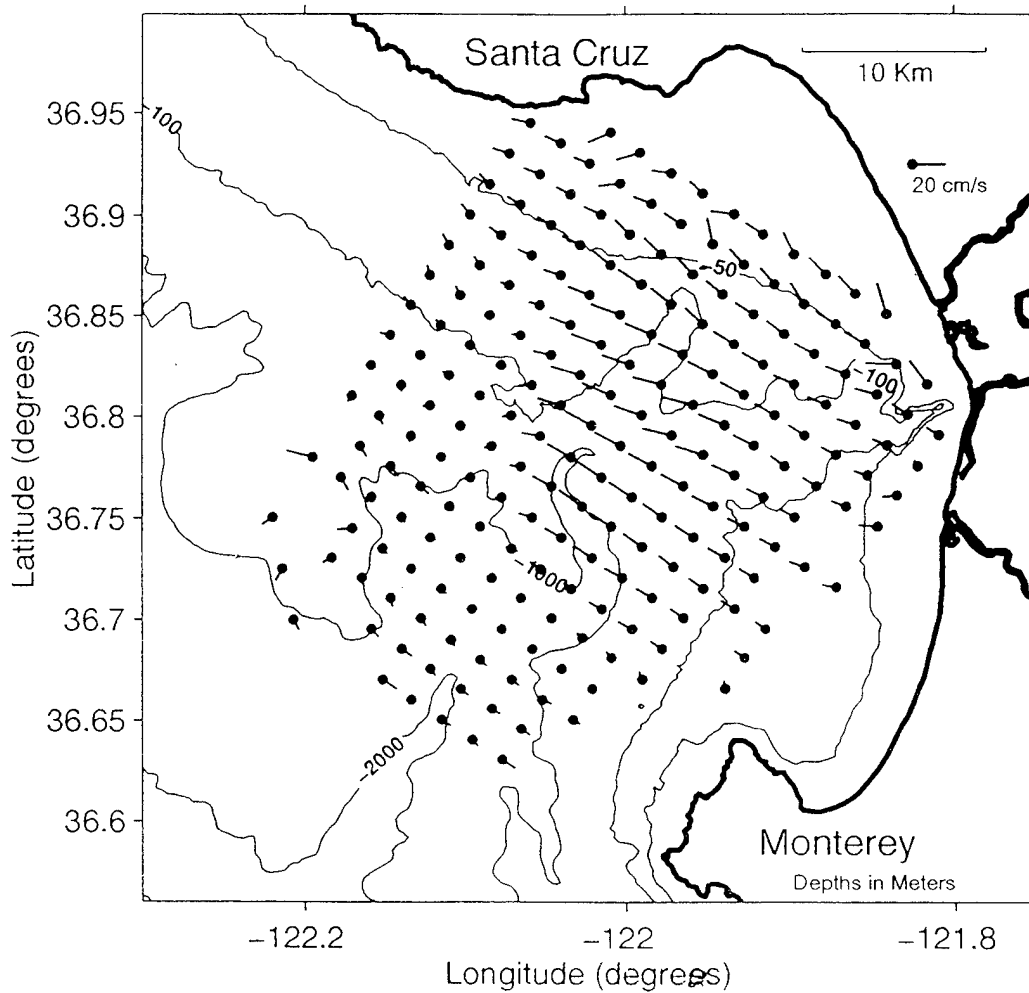


Figure 41. K1 surface current flow during flood K1 tide. Gridpoint position is indicated by the dot, flow direction is indicated by the line.

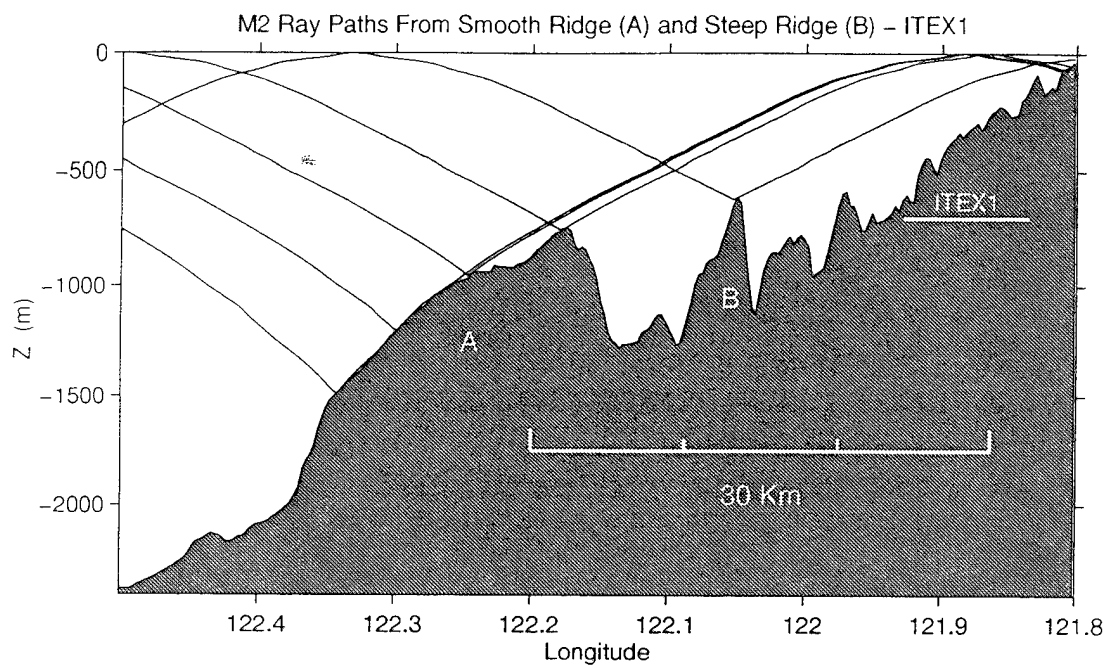


Figure 42. M2 ray traces from smooth ridge (A) and steep ridge (B) showing M2 characteristics calculated from the internal wave dispersion relation (from Petruncio, 1996).

IV. SEABREEZE

A. BACKGROUND

The sea and land breeze circulation pattern in the coastal environment is perhaps the most common and easily observed of all near surface wind features. The circulation is thermally induced by the temperature gradients between land and sea. The strength, direction, duration and time of onset vary with the topography, seasonal heating characteristics of both land and water, synoptic flow patterns, and cloud cover. As it is common and can be a dominant influence in local weather and current patterns, it is of interest to the Navy, particularly with the current emphasis on littoral operations. Not only are harbor conditions affected, but airfield wind patterns and ground level visibility influenced as well.

1. Sea/Land Breeze Dynamics

Solar irradiance provides thermal energy to both land and sea surfaces. As land warms quickly, a thermally-induced mesoscale low pressure area is formed, and a vertical rising of the warmer, less dense air occurs. Air from over the ocean flows towards the land to replace the rising air. Aloft the circulation cell is completed with offshore flow. The air, now over the relatively cool water, begins to subside and contributes to the formation of a mesoscale high (Foster, 1993; Stull, 1994).

B. Local Topography

The local topography has a critical affect on the formation and characterization of the seabreeze over Monterey Bay. Figure 43 shows the complexity of the regional land elevations. Heights range from sea level to over 1,000 m. Key features include the Salinas Valley, which extends to the southeast from Moss Landing to King City and is bounded to the west by the Santa Lucia Coastal Mountain Range; the Santa Cruz mountains which run along the coast from San Francisco towards Santa Cruz; the Santa Clara Valley, to the north of Monterey Bay, and the Pajaro Valley which is due east of Monterey Bay and provides a connection to the Santa Clara Valley. The Salinas and the Santa Clara valleys provide most of the heating that powers the seabreeze circulation cell. Therefore, the orientation of the cell should be along the direction of forcing and the location of the valleys should provide some indication of the direction toward which the seabreeze should steer.

C. Data

Wind measurements were made from three locations, two at sea and one on land. The MBARI M1 and National Oceanographic and Atmospheric Administration (NOAA) NDBC46042 buoys are located at 122.03° W, 36.75° N and 122.41° W, 36.70° N, respectively. The land-based vertical wind profiling system, located at Fritsche Field on the former Army base Fort Ord, is at 121.77° W, 36.70° N. (refer to Figure 3) Data from all three sensors was acquired for the entire month of May 1995 and was provided on an hourly basis with no gaps in the time of interest, 6-8 May. It consisted of total wind vectors which were converted into u (positive to the east) and v (positive to the north) components to enable more direct comparison with surface current measurements and to comply with the format required by the Foreman tidal analysis program. Additional information on specific details regarding collection techniques utilized for the wind data may be found in Foster's (1993) work.

D. Analysis

1. Station Description and Comparison

General characterization of the synoptic flow from 6-8 May may be observed from buoy NDBC 46042. This buoy's position allows domination by the larger scale wind flow and only minimal influence from the Monterey Bay seabreeze circulation. The top panel of Figure 44 shows that over the first half of OSCAR's operation, the winds were from the northwest at approximately 10 m/s. They began to decrease near 1000 GMT 7 May and continued to decrease until the end of the OSCAR period at which point a change of direction occurred. The synoptic flow change did affect the more seabreeze-dominated wind pattern recorded by the MBARI M1 buoy (second panel of Figure 44). After the synoptic flow decreased, there was reversed flow from the south/southwest observed following the northwesterly (seabreeze) flow. Prior to the synoptic scale decrease, the winds at M1 did not reverse direction, but rather became weaker following the seabreeze time periods.

A more indirect synoptic influence was felt at the Fort Ord profiler (third panel of Figure 44), with a general weakening of the wind's magnitude and increased definition of its direction following the decrease in synoptic flow offshore. The seabreeze became a more eastward flow, rather than running up the Salinas or Pajaro Valleys. The "off-time" flow, in the early mornings, was uniformly light and from the southwest. A separation of

the u and v wind components (Figure 45) provides an alternate visualization of the above described fluctuations, particularly in the u component.

2. Canonical Day Winds

As described above, the seabreeze asserts itself in the wind flow pattern measured by the three strategically located stations: the NDBC 42046 outside of the mouth of the bay; MBARI M1 within the bay, and Fort Ord on land in the flow path to the valley heat sources. The degree to which the sea breeze pattern is manifested is most clearly seen in a canonical day plot. The canonical day results are presented as u and v magnitudes in Figures 46 - 48. The upper plot in each figure averages the daily cycle over the full month. The lower plot uses only the wind data from 6-8 May. The longer time period helps to validate the three day operational period wind patterns as representative of typical conditions. The three-day canonical record for each station compares well to the corresponding month-long canonical record, indicating that the recorded wind fluctuations are seasonally common throughout the region, thus presenting a continued and significant influence on surface current patterns.

3. Wind and Current at MBARI M1

a. Characterization

In order to assess the correlation between the wind and certain surface current patterns observed through the OSCR system, both the wind and nearby current records were isolated and analyzed. As the seabreeze cycle is the most likely pattern to be clearly manifested in the current pattern observed over just a few days, this cycle was focused on. Although the Fort Ord wind profiler experienced the strongest seabreeze fluctuation, the MBARI M1 buoy is in the best position from which to work with both the wind and current data. Current gridpoints 187, 188, 211 and 212 (Refer to Figure 3) were chosen due to their close proximity to the M1 mooring.

The initial attempt to characterize the wind field at M1 consists of a vector "scatter plot" (Figure 49). One can see two groupings of the wind vectors, pointing toward the northeast and southeast quadrants. The southeast magnitudes tend to be the larger of the two groups. Keep in mind that the directions of the two groupings do correspond to the locations of the Parajo and Salinas Valleys. The same type of "scatter plot" was made for each of the four subject current gridpoints (Figure 50). Here also, two groupings similar in nature to those found in Figure 49 appear. However, the current vectors are rotated clockwise relative to the wind vectors. This is expected as the Ekman flow manifests itself to the right of the wind (Pickard and Emery, 1990).

In order to achieve a more temporally accurate view of the current and wind behaviors, several time line plots were constructed. The first shows the OSCR-derived current u and v components at the four surrounding grid points as well as the wind's components (Figure 51). Note the gaps in the current data (the top four panels of Figure 51). These are the four hours mentioned in Chapter II in which all three OSCR activations were contaminated by the CODAR. The last panel in Figure 51 is the corresponding wind record taken at the M1 buoy. The velocity patterns of the individual components are very similar over the majority of the record. A larger scale change appears to affect the wind near the end of the data set. Several interesting phenomena may be observed in this figure. These, as well as the other evaluative plots, are discussed in the next section.

b. Observational Analysis

The first result is that, in terms of u and v components, currents appear to be leading the wind. This may be expected given the predictions of Ekman flow for which the current vector is rotated relative to the wind vector, i.e., it is not the wind's x component that drives the current's x component, but the component that is approximately 45 degrees to the left of the current. Therefore, forcing for a particular direction may appear to take place before the wind reaches that direction. Figure 52 displays a plot of the current and wind u components and the current and wind v components. The current components are an average taken among the four gridpoints. The thin vertical lines are positioned times of current extrema. These are repeated on the wind plots for ease of comparison. The thick vertical lines are positioned at the times of wind extrema. It is seen by the relative positions of the lines in Figure 52 that the extrema of the current components lead the extrema of the wind components for a given direction.

In order to remove the possible complication of rotation of the current vector relative to the wind vector, time series of current and wind speed are shown together in Figure 53. Single vertical lines are located at the times of current speed maximums in both plots for ease of comparison. Thick lines are drawn at the times of maximum wind speed. There is a suggestion in this figure that the wind speed peaks after the current speed peaks. This is surprising assuming that the ocean current should follow the motion of the wind forcing above it.

c. Statistical Analysis

A more objective method in determining the relationship between the wind and current cycles is statistical correlation analysis. This was performed on the current velocities averaged between the four gridpoints and the wind measured at the MBARI M1

buoy. Figure 54 displays the cross correlation between the wind and current u components, v components, and speed versus time lag. Assuming all 53 hours used in these correlations represent independent observations, the 95% significance level for these correlations (at zero lag) is 0.27 (Bevington, 1969). The sinusoidal patterns for the u and v components indicate a cyclical correlation with maxima every 12 hours, which would be the case for 24-hour-period oscillatory motions. The maximum component correlations are offset slightly from zero lag indicating that the current leads the wind. The bottom panel in Figure 54 demonstrates significant correlation between the current and wind speeds that is better than that obtained for the u or v components separately. This would be expected following the observations and discussion regarding Ekman forcing (Figure 52).

The complex correlation (Kundu, 1976) can be used to combine the information in the separate component and speed correlations. The magnitude and direction of the complex cross-correlation are shown in Figure 55 versus time lag. The peak correlation is about 1 hour to the left of zero lag, which suggests that the peak current occurs 1 hour prior to the peak wind. The nearly constant slope ($\sim 300^\circ$ in 19 hours) of the phase line in the bottom panel indicates that the correlation is dominated by single-period phenomena with periods of ~ 23 hours. The average angular difference at zero lag (Kundu, 1976) shows OSCAR currents approximately 70° to the right of the wind at the M1 mooring.

d. Interpretation

Neal (1992) and Foster (1993) reported similar wind/current results at the MBARI M1 mooring site using month-long CODAR datasets. They also determined that the wind speed peaked after the current speed peaked. Foster proposed that the difference was due to the transfer of wind momentum to a thickening surface mixed layer. This deepening is consistent with slab-based mixed layer models, such as the classic formulations of Kraus and Turner (1967) and Pollard et al. (1973). Because OSCAR and CODAR measurements are weighted to the upper 1 m of the water column, after the mixed layer deepens beyond that depth, the measured speed of the water will not necessarily increase with continued increase in wind speed. Instead, the depth of the layer of water being driven by the wind may increase.

In the present study, the short record length and one-hour time step that were used in the comparisons mean that the subtle lags observed may not be significantly different from zero. It is also possible, of course, that forcing phenomena other than winds, such as tides, could influence the observed current records and impose an arbitrary phase relative to the winds. Longer records could be used to investigate this possibility by

focusing, separately, on the relative phases of the diurnal and semidiurnal winds and currents assuming the diurnal tidal currents are negligible, as discussed in the next section.

4. Seabreeze and K1 Tidal Component

As mentioned at the end of the tidal analysis chapter, the K1 component in the Monterey Bay currents are too strong to have been influenced only by tidal forcing. At this sub-inertial period, tidally forced fluctuations cannot propagate away as baroclinic internal waves and, as pointed out by Petruncio (1996), the barotropic tidal currents in Monterey Bay are ~ 1 cm/sec, some 20 times smaller than the observed K1 currents. It is, therefore, assumed that, rather than tidal forcing, observed diurnal fluctuations are due to the close proximity of the seabreeze periodicity to that of the K1 constituent, i.e., it is the seabreeze-forced fluctuations that appear in the tidal analysis.

To illustrate the obvious K1 component in the observed wind records, data from each of the three stations were processed through the same tidal analysis program used to extract current constituents. Figure 56 shows very substantial "tidal" ellipses from each of the three stations. Note that, as expected, the ellipses progress from being almost symmetrical at the NDBC 46042 buoy to being very elongated at the Fort Ord profiler. When just the MBARI M1 ellipse is compared to the current ellipses around it, an approximate 45° shifting to the right of the current phase vectors relative to the wind phase vector is seen.

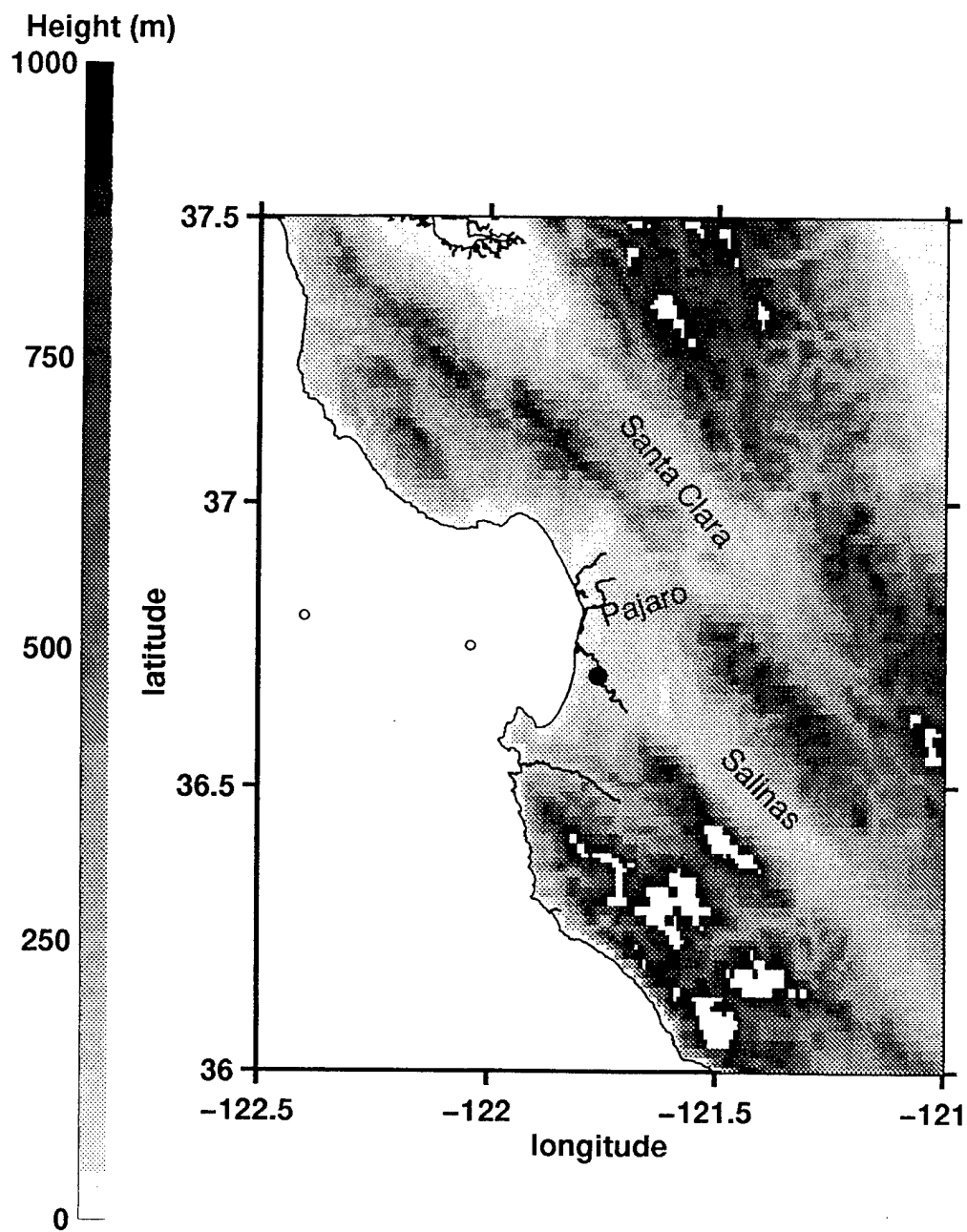


Figure 43. Topography of the central California coastal area. Note positions of sea moorings (o) and inland profiler station (•) in relation to the Salinas, Pajaro and Santa Clara Valleys. White areas indicate heights outside of greyscale range (from US Geological Survey and National Ocean Service data).

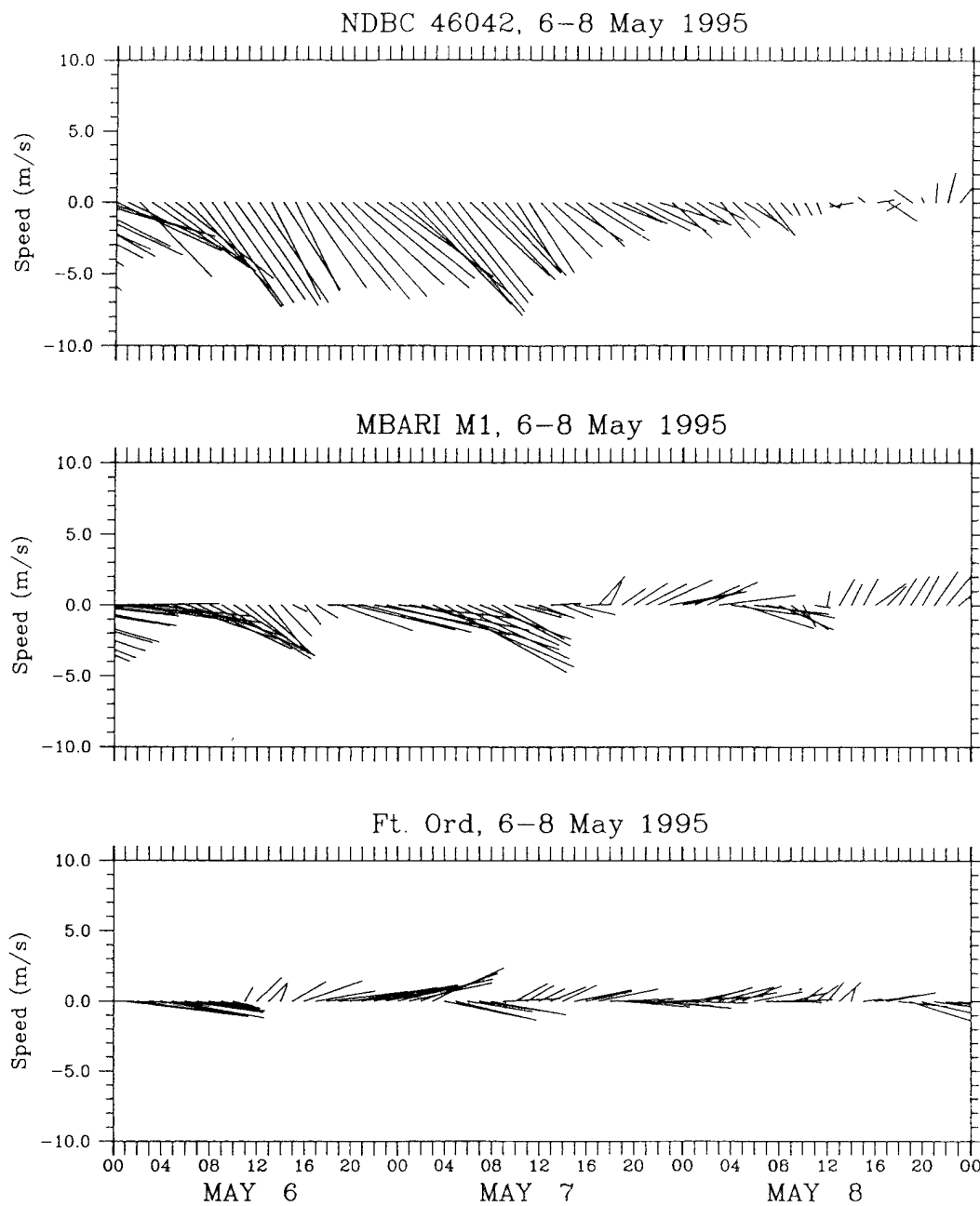


Figure 44. Time series (GMT) of wind velocity vectors at NDBC 46042, MBARI M1 and Fort Ord profiler sites.

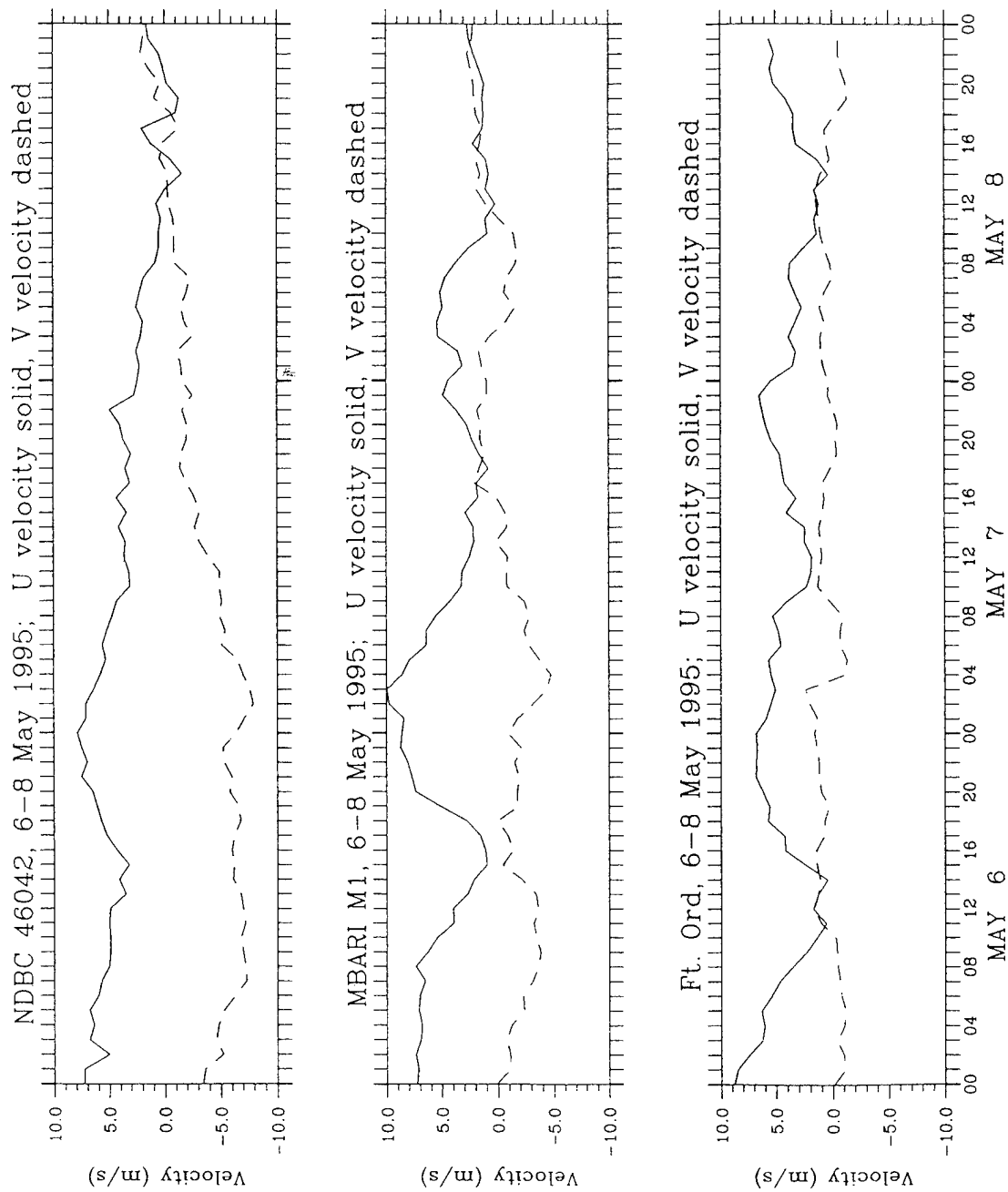


Figure 45. Time series (GMT) of wind velocities, split into u and v directional components, at NDBC 46042, MBARI M1 and Fort Ord profiler sites.

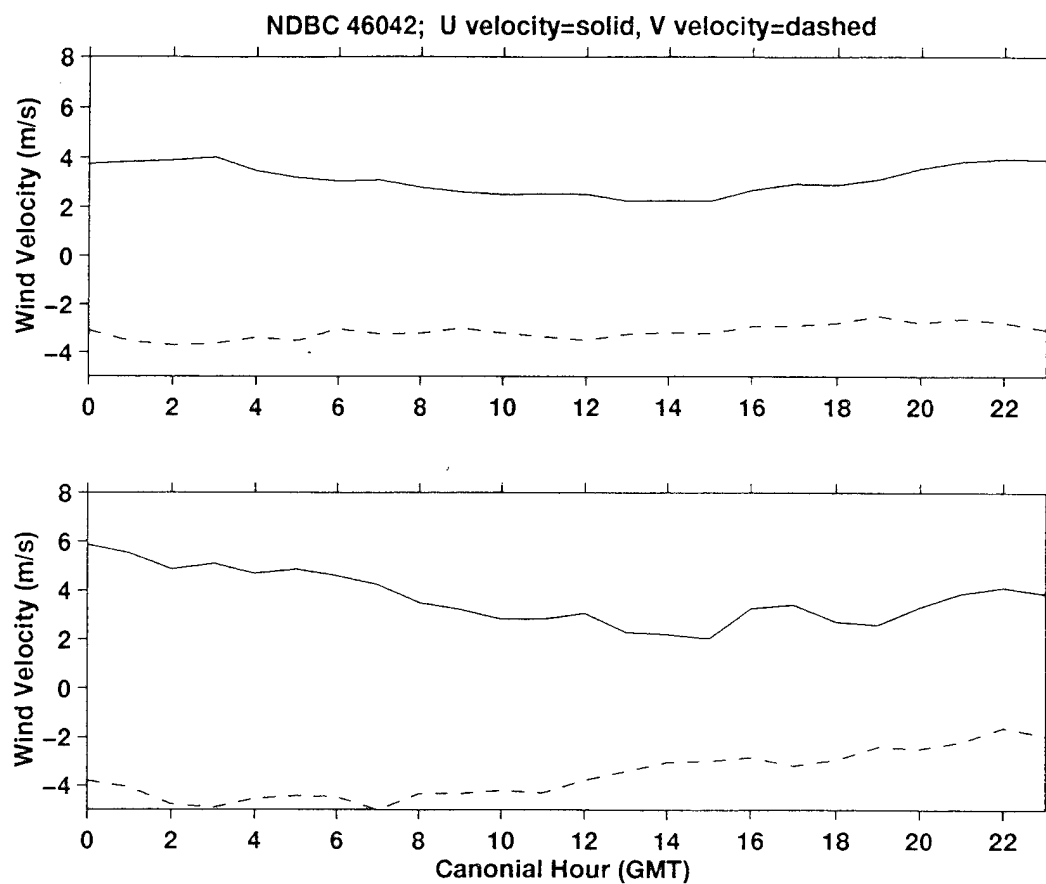


Figure 46. Canonical-hour wind component time series for NDBC 46042 mooring. Top plot is derived from the 30-day May 1995 record, bottom plot derives from the 53-hour 6-8 May, 1995 subset.

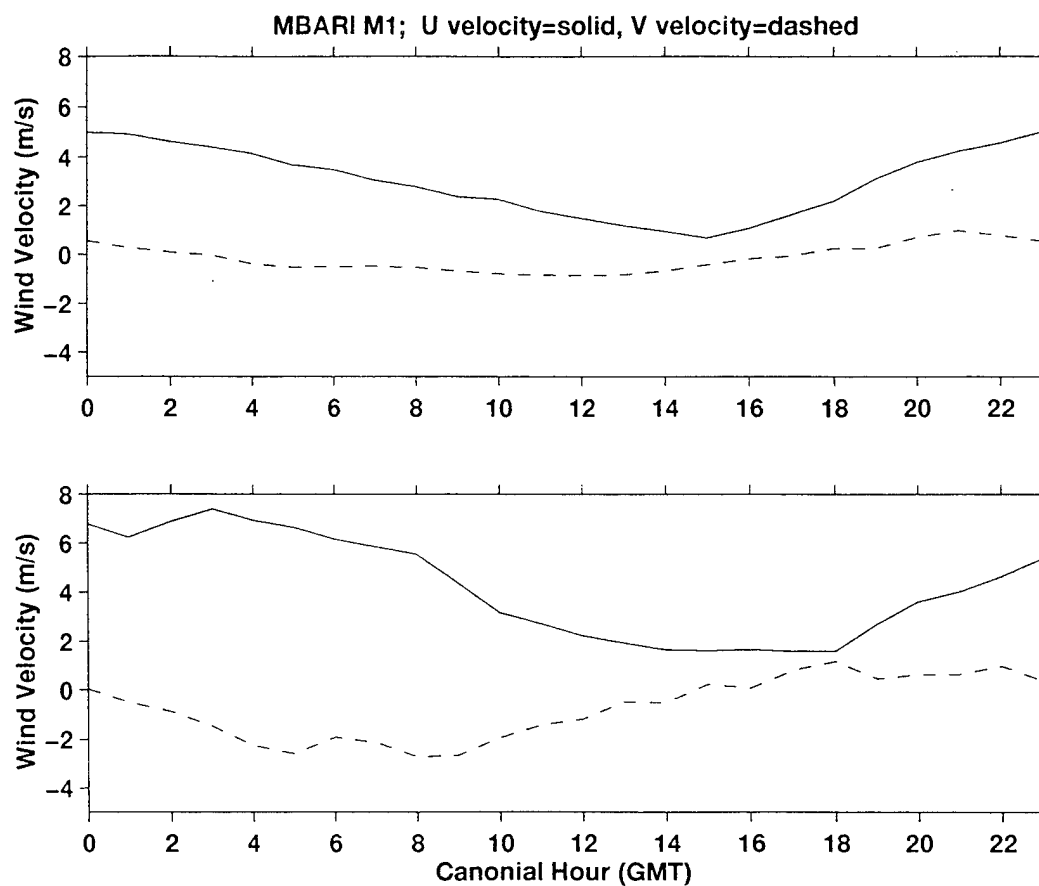


Figure 47. Canonical-hour wind component time series for MBARI M1 mooring. Top plot derives from the 30-day May, 1995 record, bottom plot derives from the 53-hour 6-8 May, 1995 subset.

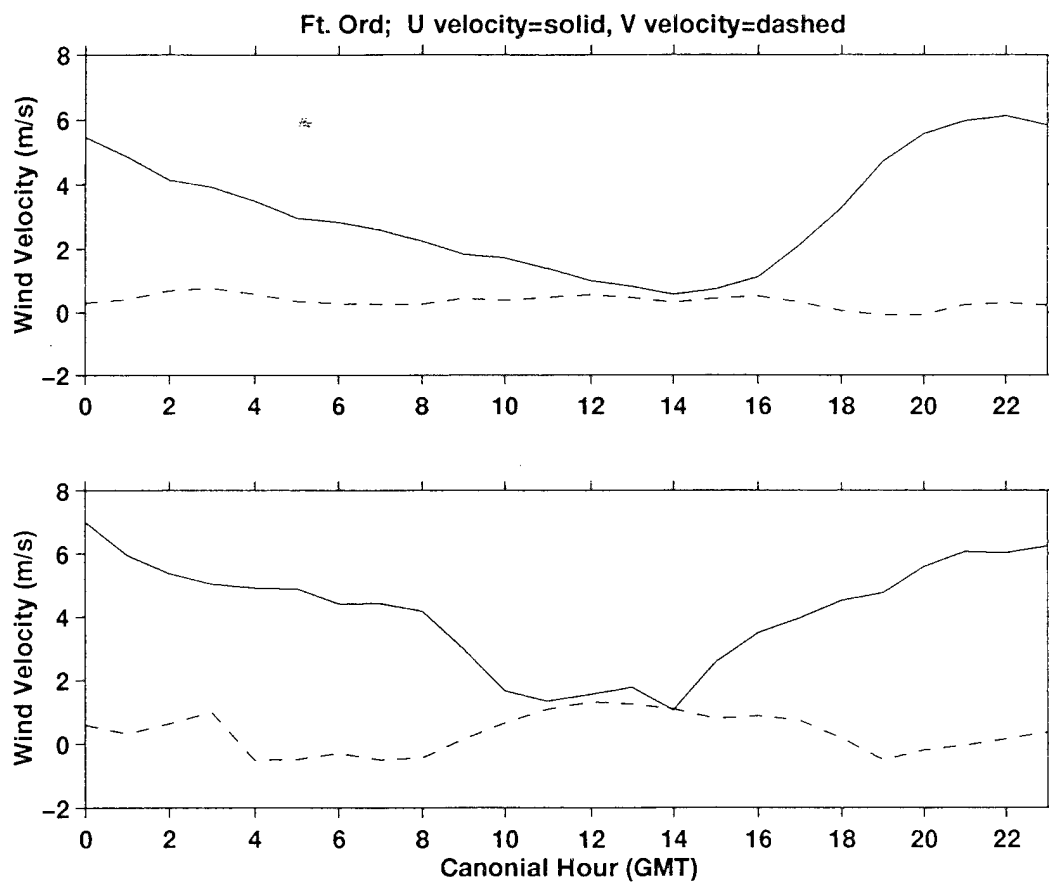


Figure 48. Canonical-hour wind component time series for Fort Ord profiler. Top plot derives from the 30-day May 1995 record, bottom plot derives from the 53-hour 6-8 May, 1995 subset.

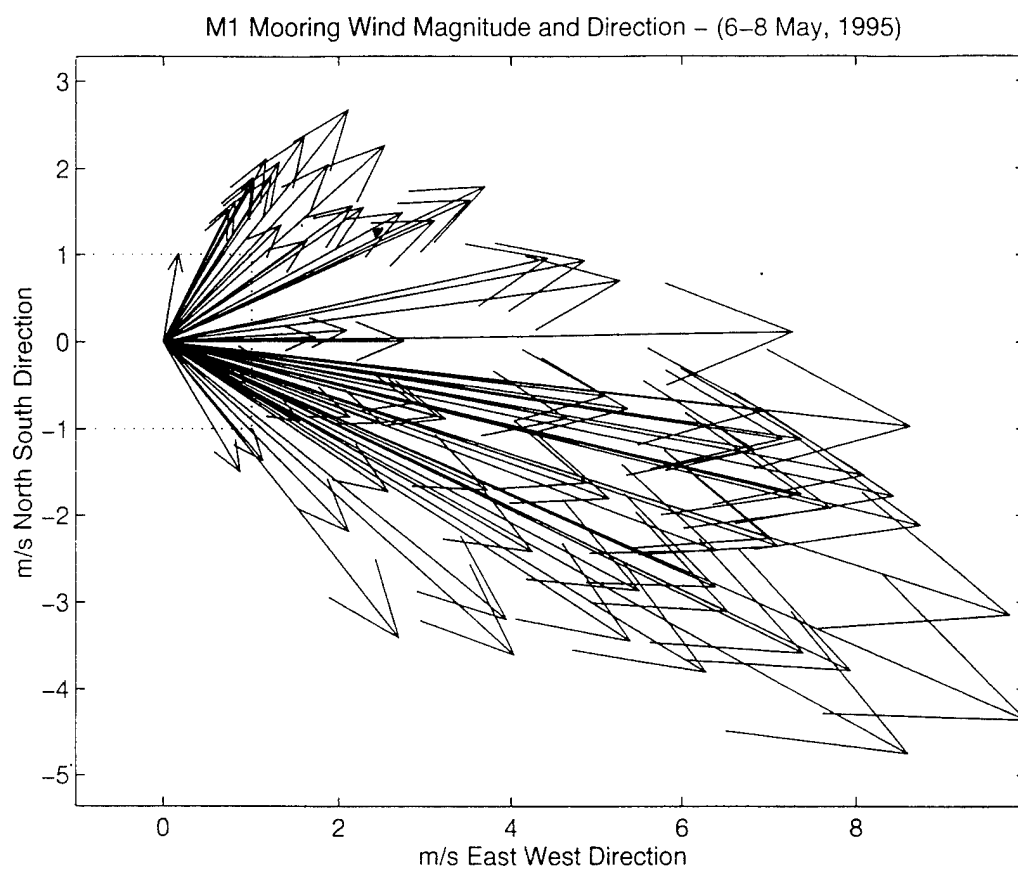


Figure 49. Wind vectors at MBARI M1 mooring, 6-8 May, 1995.

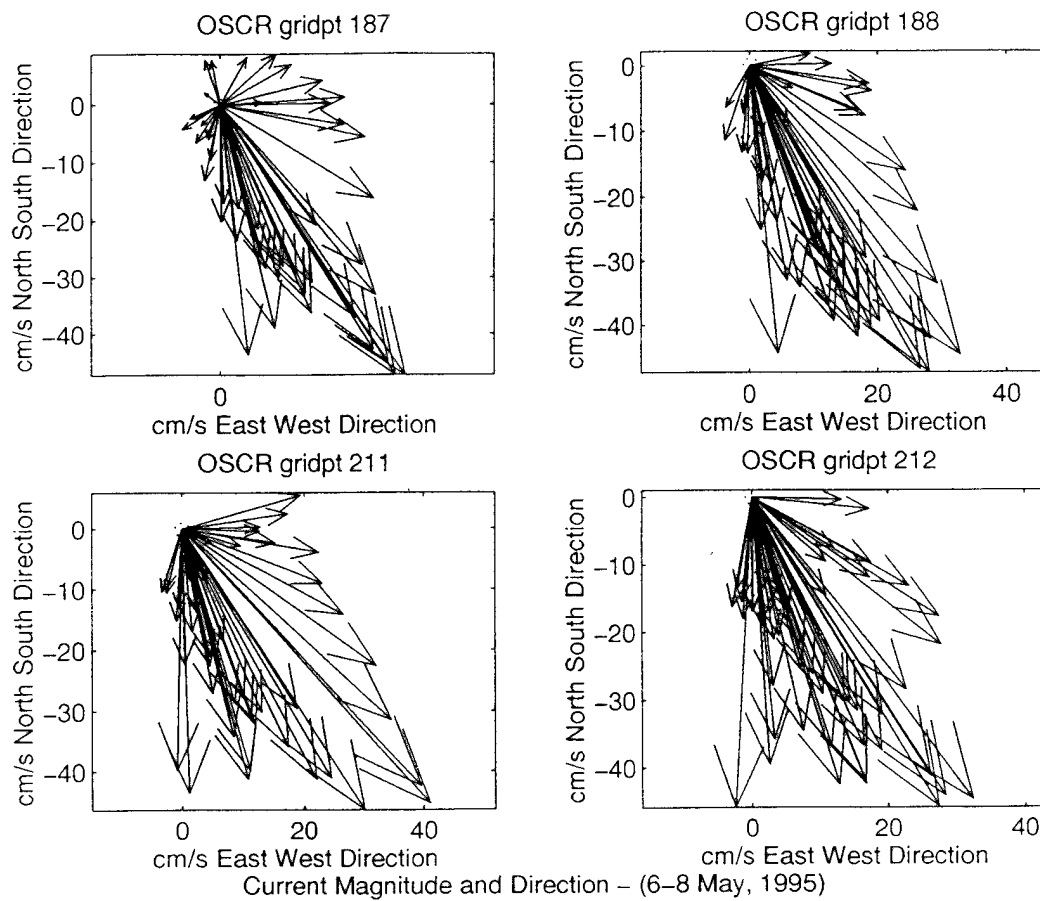


Figure 50. Current vectors at four OSCR gridpoints surrounding MBARI M1 mooring, 6–8 May, 1995.

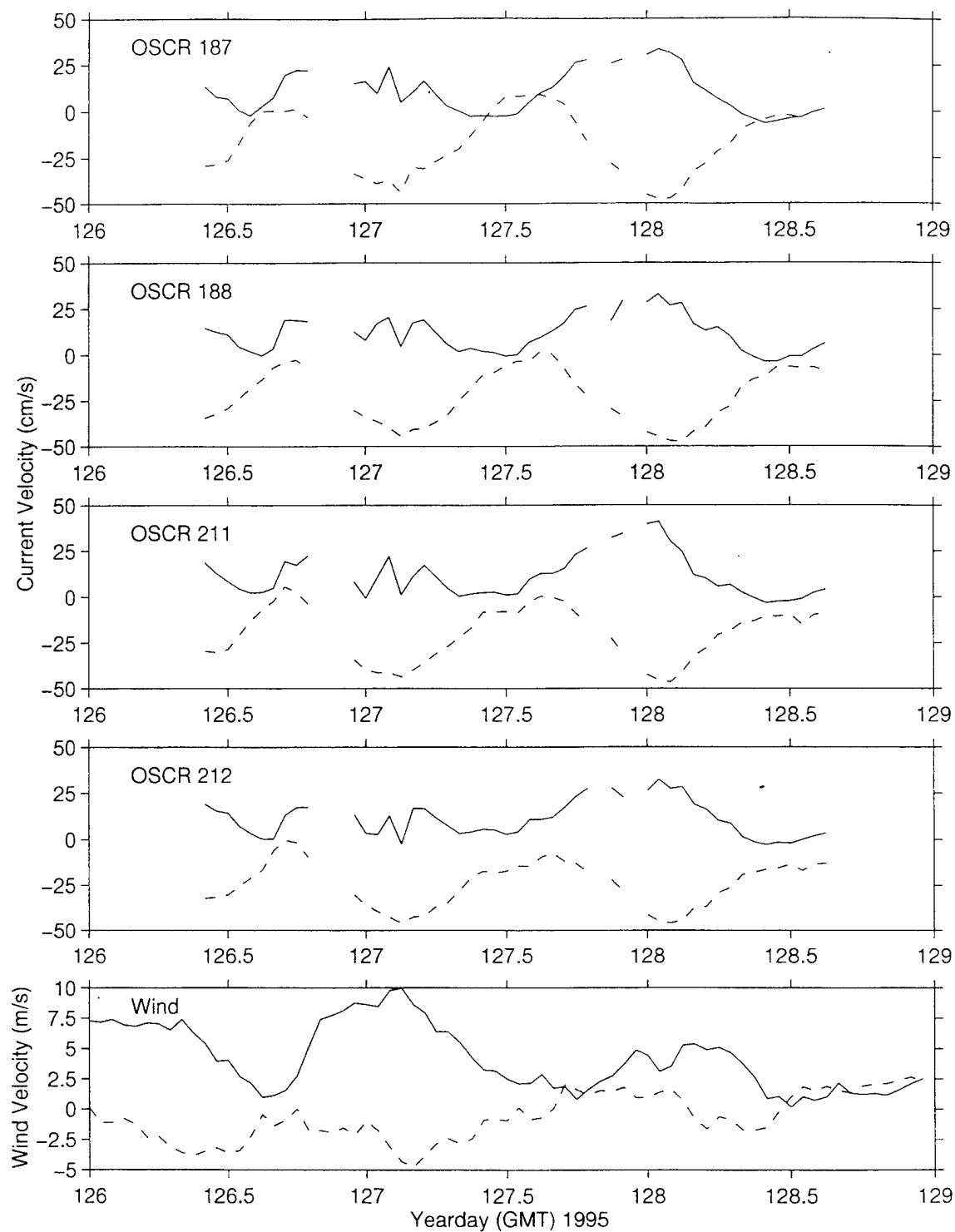
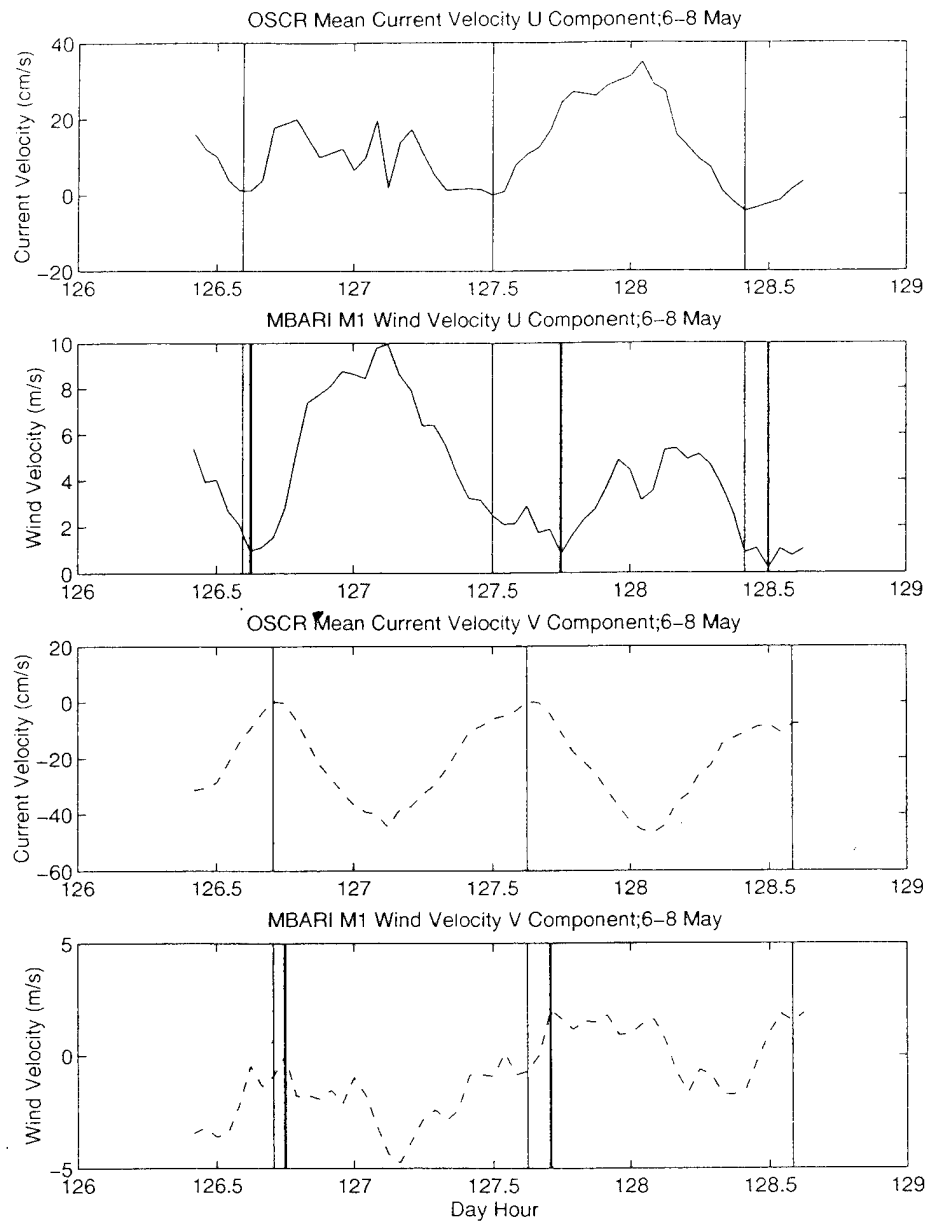


Figure 51. Time series of current and wind velocities, split into u and v directional components, at (from top to bottom) OSCR gridpoints 187, 188, 211, 212, and MBARI M1 mooring.



Thick lines at initiation of wind acceleration.

Figure 52. Velocity components of average current between the four surrounding OSCR gridpoints and corresponding component of wind at MBARI M1 mooring. Thin vertical lines on both wind and current plots indicate current minima. Thick vertical lines, on wind plots only, indicate times of wind minima. Note that the current acceleration leads the wind acceleration.

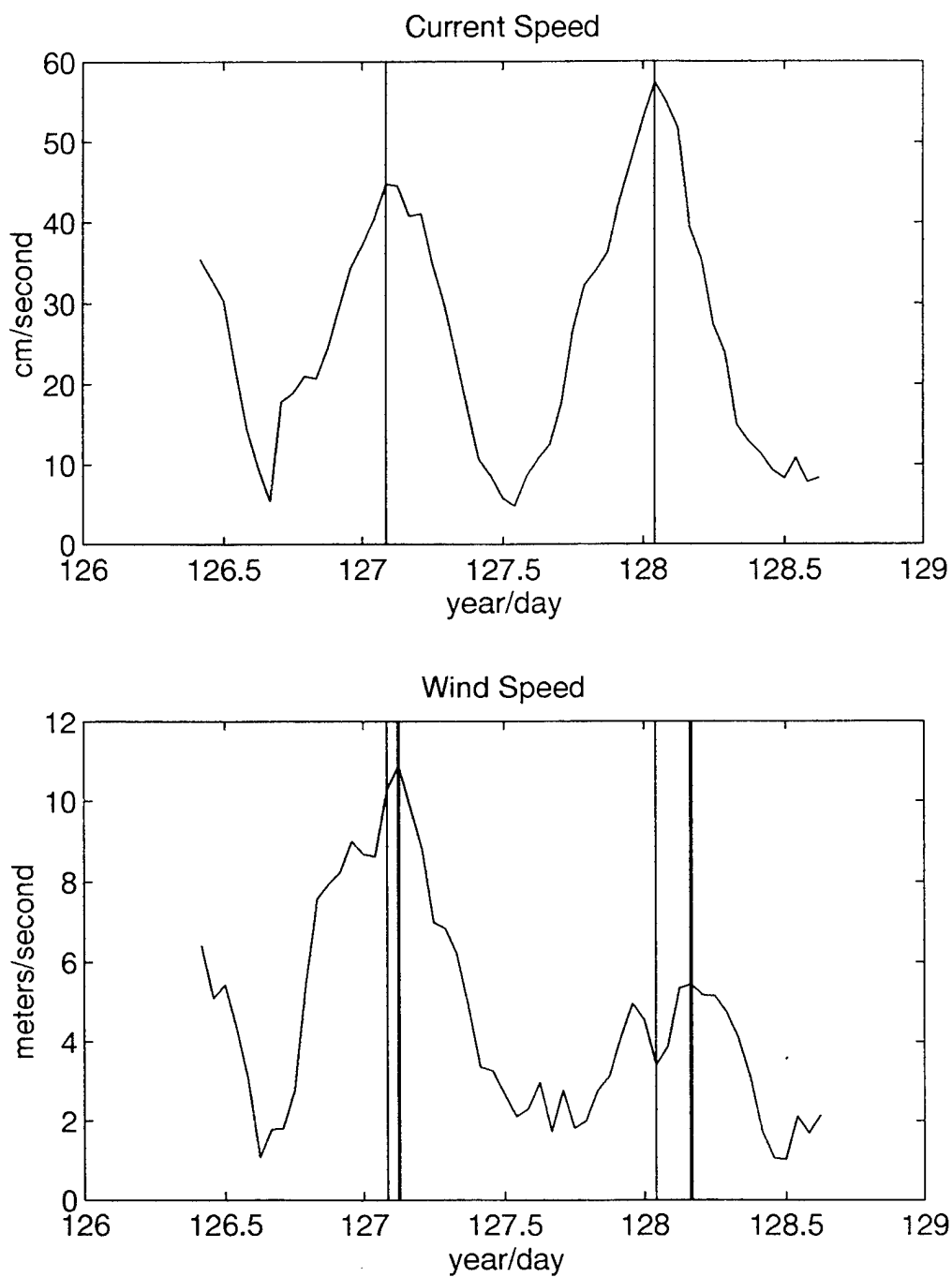


Figure 53. Speed of average current between the four surrounding OSCR gridpoints and of wind at MBARI M1 mooring with thin vertical lines on both wind and current plots at times of maximum current speed and thick vertical lines, on wind plot only, at times of maximum wind speed. Note that the current speed peak leads the wind speed peak.

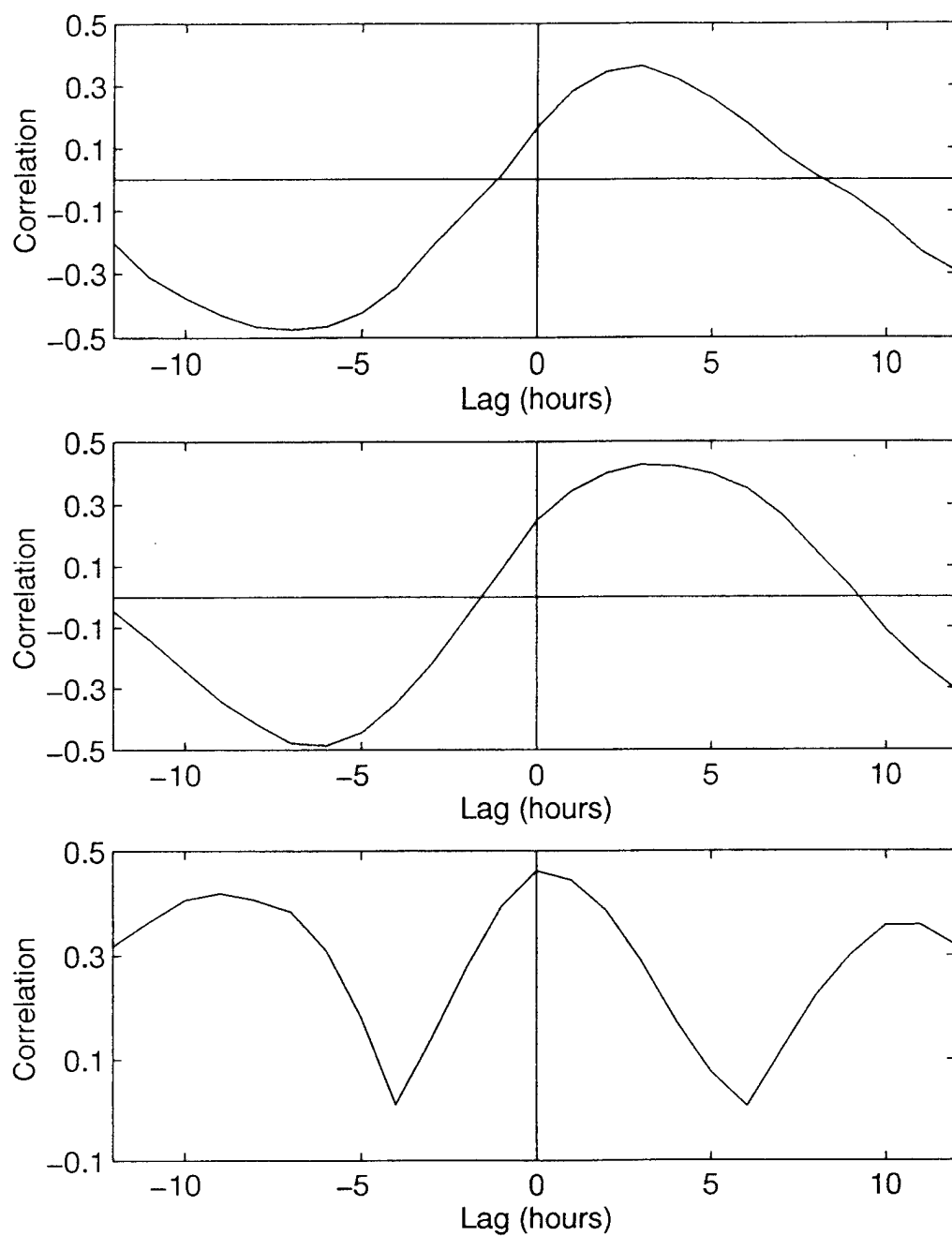


Figure 54. Magnitudes of lagged cross correlation between the u (upper) and v (middle) current and wind velocity components and the speed (lower) between wind at MBARI M1 and average current at the four surrounding OSCR gridpoints.

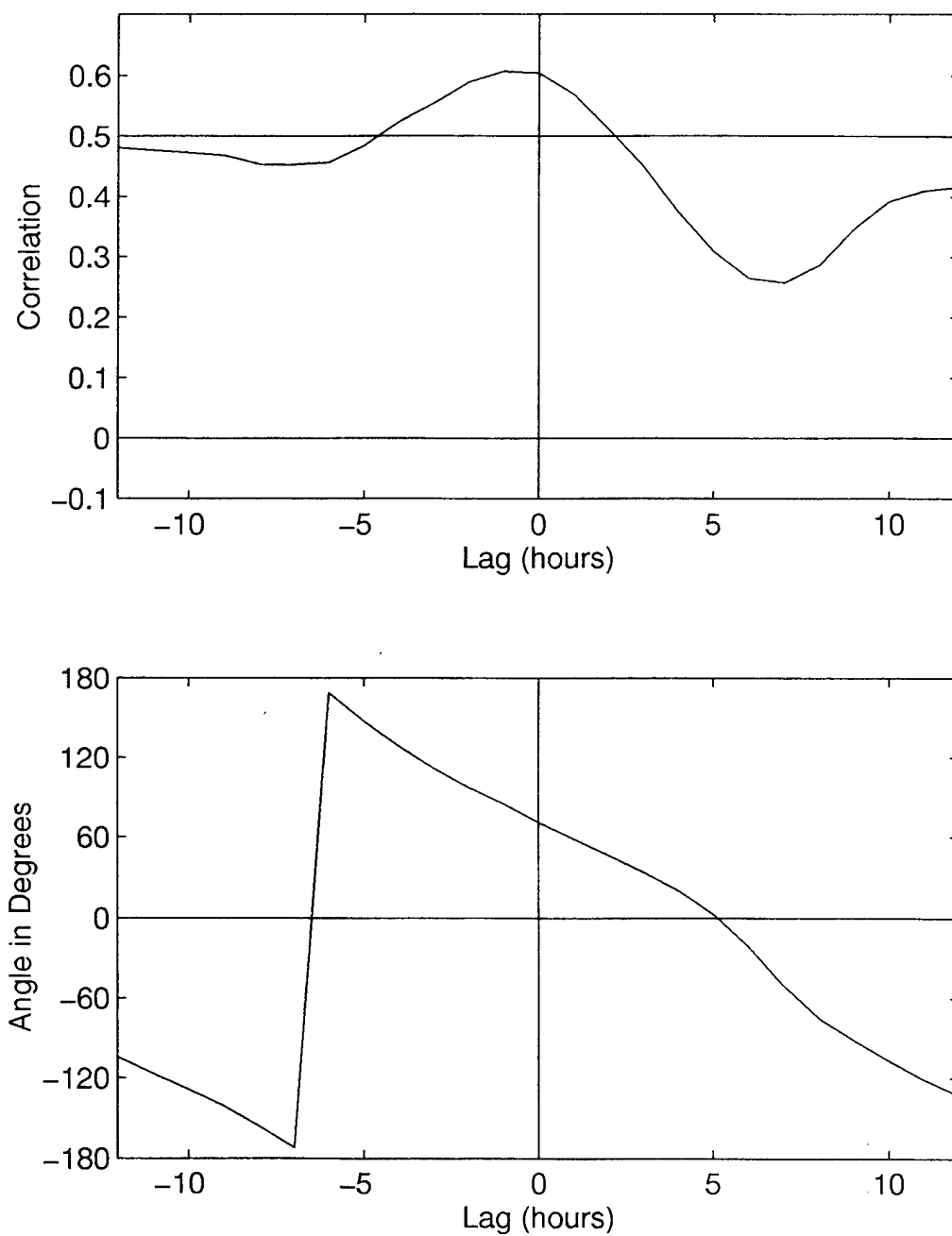


Figure 55. Magnitude (top) and direction (bottom) of lagged complex cross correlation between the wind at MBARI M1 and average current at the four surrounding OSCR gridpoints.

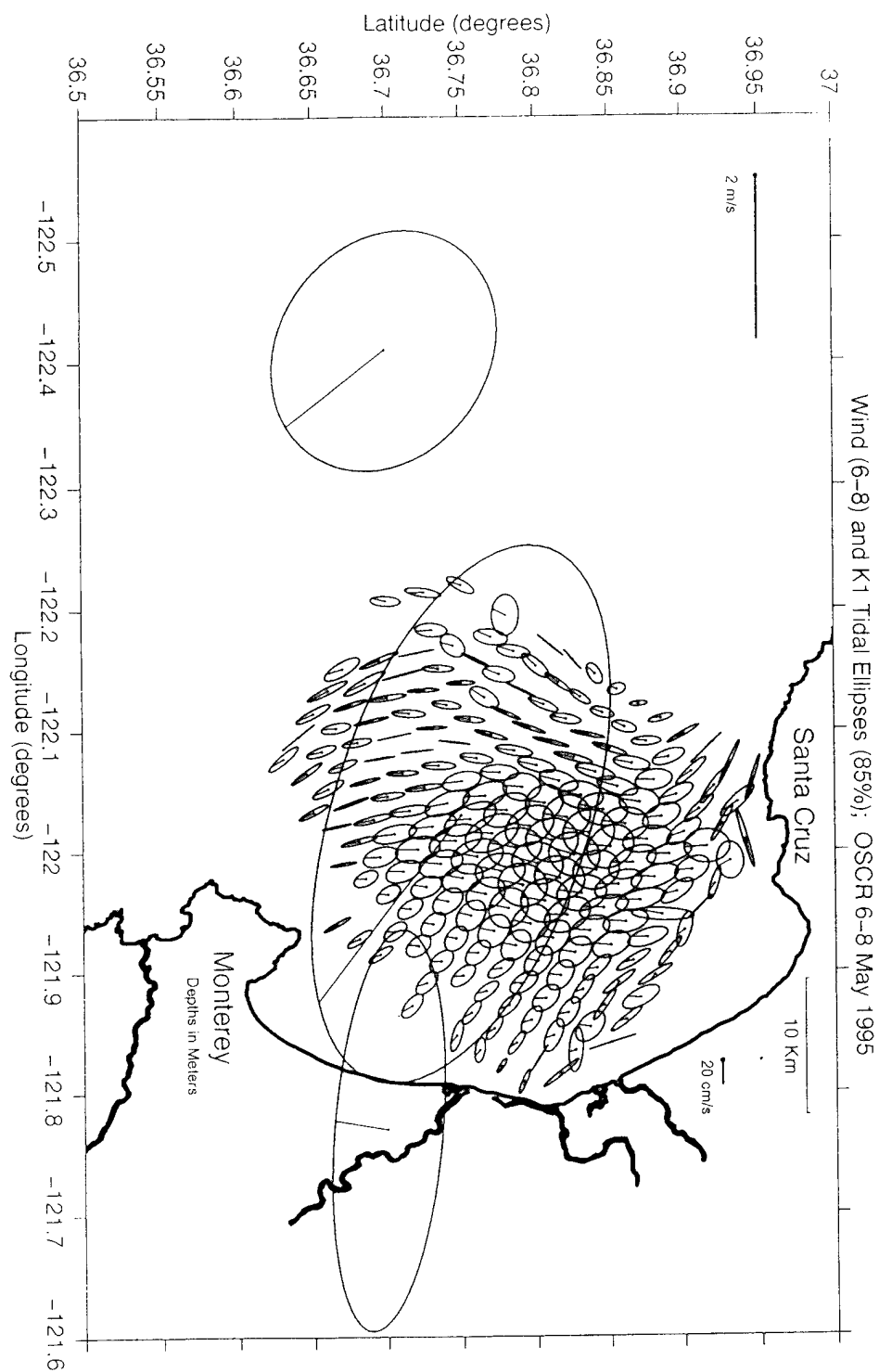


Figure 56. K1 tidal ellipse plot and wind K1 tidal-period ellipses for three wind stations for 6-8 May 1995.

V. CONCLUSIONS AND RECOMMENDATIONS

A. CONCLUSIONS

A 53-hour-long record of surface current data from the HF radar system OSCAR was gathered over Monterey Bay on 6-8 May, 1995. This system was deployed in order to compare it with CODAR, a system already established in its coverage of the Monterey Bay area. The OSCAR data was evaluated with regard to semidiurnal (M2) and diurnal (K1) tidal period fluctuations, the seabreeze, seabreeze influenced flow, and both standard and canonical mean flow patterns.

1. System Evaluation

Surface currents derived by OSCAR provide constructive tools for the study of total circulation characteristics in Monterey Bay. OSCAR coverage of over 1,100 km² produced data with a spatial resolution comparable to the CODAR system. Its temporal resolution of one measurement per 20 minutes is three times finer than that of the CODAR system. A substantial amount of information was able to be extracted from a relatively short time series, which indicates fairly stable OSCAR measurements. Although the temporal resolution helped in this study, in an operational system installment the data acquisition rate would need to be considered with regard to the objectives of the project and the temporal variation characteristics of the subject studied. For example, longer duration deployments may not require 20-minute sampling to resolve the important semidiurnal, diurnal and sub-tidal fluctuations along the coast.

With regard to the spatial resolution of OSCAR, Barrick (1996) discusses likely problems with phased-array HF radar systems that reflect the possible existence of oversized and distorted side lobes in the antenna's beam pattern. The data's directional information should be extracted using a well defined narrow beam. If not, an excessively smooth field of radial currents would be produced as a function of bearing. Results would tend to have a lower signal to noise ratio and a larger directional uncertainty causing radial maps that have lesser range, reduced velocities, and only broad or "smeared" features.

The only way to definitively determine the actual shape of the beam pattern is to take measurements in the coverage field. This was not done during the OSCAR deployment, nor has it been done for any documented deployment of that system. However, during the Monterey deployment, if there was distortion of the OSCAR beam patterns, which is likely to have occurred, the effect of this distortion was not so severe as to swamp the diurnal-

period signals. In particular, the semidiurnal current variations showed strong horizontal patterns correlated with the local bathymetry in a manner similar to prior CODAR observations. This M2 constituent displays evidence of interaction between the barotropic M2 tidal forcing and an internal wave produced by stratification as suggested by Petruncio (1993; 1996). The magnitudes were also in order with measurements taken with the independent CODAR systems.

The surface currents at Monterey Bay are strongly influenced by the seasonal sea-breeze wind cycle at nearly the same frequency as the K1 tidal constituent. As observed before (Foster, 1993; Petruncio, 1993; Paduan et al., 1995), the OSCR-derived K1 current fluctuations have larger spatial scales than the M2 constituents and the magnitudes are much greater than can be attributed to barotropic K1 tidal forcing. Evidence of the sea-breeze influence on the surface currents is also observed in the high degree of correlation between the wind measured at the MBARI M1 mooring and the surface currents measured at the four surrounding OSCR gridpoints. The average correlation of the four types of comparisons made (total magnitudes, complex magnitudes, u and v components) was above 0.5, while at 95% confidence interval, 0.27 would indicate a significant correlation (Bevington, 1969).

Operation of the CODAR system during the same period as OSCR caused contamination of the OSCR data. Significant contamination of both master and slave OSCR data occurred with the activation of the CODAR system because that station operates at the same frequency as OSCR. Contamination was also caused by the SeaSonde's activation, which operates at a lower frequency. This only appeared to affect the nearby master OSCR data.

B. RECOMMENDATIONS

Data record lengths used in future demonstrations and evaluations of OSCR should be at least five days. Of course, operational records for a number of months would be preferable, enabling distinctions between the various frequencies and associated forcing structures that contribute to ocean surface currents.

In order to definitively address the issues and concerns regarding the phased-array antenna beam pattern mentioned above, ship time needs to be utilized during OSCR operation to collect direct antenna calibration data using transponders within the radar coverage area. Also helpful would be to conduct a series of intentionally "faulty" deployments and

configurations with a coinciding monitoring of the resultant beam patterns, thus resulting in a post-facto trouble-shooting chart. This would aid in evaluating the validity of data gathered by antennas required to be deployed under less than ideal conditions. Much of this work could be accomplished via simulations of backscatter spectra under known wind and wave conditions combined with additional field measurements in controlled, well-instrumented vicinities, such as Monterey Bay.

LIST OF REFERENCES

- Barrick, D.E., "Impact of Distorted OSCAR Array Antenna Patterns on Current Mapping," Unpublished, 1996.
- Barrick, D.E., Evans, M.W., and Weber, B.L., "Ocean Currents Mapped by Radar," *Science*, 198, 138-144, 1977.
- Bevington, P.R., *Data Reduction and Error Analysis for the Physical Sciences*, 336 pp., McGraw-Hill, New York, 1969.
- Broenkow, W.W., and Smethie, W.M., Jr., "Surface Circulation and Replacement of Water in Monterey Bay," *Estuarine and Coastal Marine Science*, 6, 583-603, 1978.
- Chapman, R.D., Shay, L.K., Graber, H.C., Edson, J.B., Karachintsev, A., Trump, C.L., and Ross, D.B. "The Accuracy of HF Radar Current Measurements," *Journal of Geophysical Research*, In press, 1996.
- Fernandez, D.M., and Paduan, J.D., "Simultaneous CODAR and OSCAR Measurements of Ocean Surface Currents in Monterey Bay," *Proceedings, IEEE/IGARSS*, Lincoln, Nebraska, May, 1996.
- Foreman, M.G.G., *Manual for Tidal Currents Analysis and Prediction*, Institute of Ocean Sciences, Patricia Bay, Sidney, British Columbia, Canada, (1st ed. 1978; reprinted 1979, 1982, 1984.)
- Foster, M.D., *Evolution of Diurnal Surface Winds and Surface Currents for Monterey Bay*, Master's Thesis, Naval Postgraduate School, Monterey, California, 1993.
- Gill, A.E., *Atmosphere-Ocean Dynamics*, 662 pp., Academic Press, New York, 1982.
- Godin, G., *The Analysis of Tides*, University of Toronto Press, Toronto, 1972.
- Graber, H.C., Thompson, D.R., and Garande, R.E., "Ocean Surface Features and Currents Measured with Synthetic Aperture Radar Interferometry and HF Radar," *Journal of Geophysical Research*, 101, (C11), 25813-25832, 1996.
- Gurgel, K. W., "Shipborne Measurement of Surface Current Fields by HF Radar," *L'Onde Électrique*, 74, (5), 54-59, 1994.
- Iverson, R.M., "Product Summary Marconi Radar Systems: Ocean Surface Current Radar (OSCAR)," Ivy Inc., Technical product information, Unpublished, 3100 North Bay Rd, Miami Beach, FL., 1996.
- Kraus, E.B., and J.S. Turner, "A One-Dimensional Model of the Seasonal Thermocline: II, the General Theory and its Consequences," *Tellus*, 19, 98-106, 1967.

- Kundu, P.K., "Ekman Veering Observed near the Ocean Bottom," *Journal of Physical Oceanography*, 6, 238-242, 1976.
- Lipa, B.J., and Barrick, D.E., "Least-Squares Method for the Extraction of Surface Currents from CODAR Crossed-Loop Data: Application at ARSLOE," *IEEE Journal of Oceanic Engineering*, OE-8, 226-253, 1983.
- Melton, D.C., *Remote Sensing and Validation of Surface Currents from HF Radar*, Master's Thesis, Naval Postgraduate School, Monterey, California, 1995.
- Menke, W., *Geophysical Data Analysis: Discrete Inverse Theory*, 260 pp., Academic Press, New York, 1984.
- Munk, W., Snodgrass, F., and Wimbush, M., "Tides Offshore: Transition from California Coastal to Deep-Sea Waters," *Geophysical Fluid Dynamics*, 1, 161-235, 1970.
- Neal, T.C., *Analysis of Monterey Bay CODAR-Derived Surface Currents, March to May 1992*, Master's Thesis, Naval Postgraduate School, Monterey, California, 1992.
- Paduan, J.D., Barrick, D.E., Petruncio, E.T., and Lipa, B.J., "Surface Currents Within and Offshore of Monterey Bay as Mapped by a Multiple-Site HF Radar (CODAR) Network," *Proceedings, IEEE Fifth Working Conference on Current Measurement*, St. Petersburg, FL., 7-9 February, 1995.
- Paduan, D.J. and Rosenfeld, L.K., "Remotely Sensed Surface Currents in Monterey Bay from Shore-Based HF Radar (Coastal Ocean Dynamics Application Radar)," *Journal of Geophysical Research*, 101, (C9), 20669-20686, 1996.
- Petruncio, E.T., *Characterization of Tidal Currents in Monterey Bay from Remote and In-Situ Measurements*, Master's Thesis, Naval Postgraduate School, Monterey, California, 1993.
- Petruncio, E.T., *Observations and Modeling of the Internal Tide in a Submarine Canyon*, Doctoral Dissertation, Naval Postgraduate School, Monterey, California, 1996.
- Pickard, G.L. and Emery, W.J., *Descriptive Physical Oceanography, An Introduction*, 312 pp., Pergamon Press, New York 1990.
- Pollard, R.T., Rhines, R.B., and Thompson, R.O.R.Y., "The Deepening of the Wind Mixed Layer," *Geophysical Fluid Dynamics*, 3, 381-404, 1973.
- Sandstrom, H., "The Origin of Internal Tides (A Revisit)," *Tidal Hydrodynamics*, Bruce B. Parker, ed., 437-447, 1991.
- Shea, R.E., and Broenkow, W.W., "The Role of Internal Tides in the Nutrient Enrichment of Monterey Bay, California," *Estuarine, Coastal and Shelf Science*, 15, 57-66, 1982.

Stewart, R.H., and Joy, J.W., "HF Radio Measurement of Surface Currents," *Deep-Sea Research*, 21, 1039-1049, 1974.

Stull, R.B., *An Introduction to Boundary Layer Meteorology*, 593-595. Kluwer Academic Publishers, Dordrecht, The Netherlands, 1994.

Werner, F.E. "Tidal Hydrodynamics, Quantitative Aspects," *Encyclopedia of Earth System Science*, 4, 351-367, Academic Press, San Diego, 1992.

INITIAL DISTRIBUTION LIST

		No. Copies
1.	Defense Technical Information Center 8725 John J. Kingman Rd., STE 0944 Ft. Belvoir, VA 22060-6218	2
2.	Dudley Knox Library Naval Postgraduate School 411 Dyer Rd. Monterey, CA 93943-5101	2
3.	Library, Moss Landing Marine Laboratory P.O. Box 223 Moss Landing, CA 95039	1
4.	Harold A. Miller Library Hopkins Marine Station, Stanford University Cabrillo Point Pacific Grove, CA 93950	1
5.	Library, Scripps Institute of Oceanography Code C-075 University of California, San Diego La Jolla, CA 92093	1
6.	Research Coordinator Monterey Bay National Marine Sanctuary 299 Foam St., Suite D Monterey, CA 93940	1
7.	Commanding Officer U.S. Coast Guard Station 100 Lighthouse Ave. Monterey, CA 93940	1
8.	Commander Naval Meteorology and Oceanography Command 1020 Balch Blvd Stennis Space Center, MS 39529-5005	1
9.	Commanding Officer Naval Oceanographic Office 1002 Balch Blvd Stennis Space Ctr, MS 39522	1
10.	Director, Naval Oceanography Division Naval Observatory 34th and Massachusetts Avenue, NW Washington, D.C. 20390	1

- | | | |
|-----|--|---|
| 11. | Mr. Marshall Paige, Code N511
Naval Oceanographic Office, Bldg 8100
Stennis Space Ctr, MS 39522-5001 | 1 |
| 12. | Dr. Jeffrey D. Paduan
Department of Oceanography, Code OC/Pd
833 Dyer Rd Room 328
Monterey, CA 93943-5000 | 1 |
| 13. | Dr. Leslie K. Rosenfeld
Department of Oceanography, Code OC/Ro
833 Dyer Rd Room 328
Monterey, CA 93943-5000 | 1 |
| 14. | Dr. Daniel Fernandez
Baskin Center for Computer Engin. & Info. Sci.
University of California, Santa Cruz
Santa Cruz, CA 95064 | 1 |
| 15. | Dr. W.W. Broenkow
Moss Landing Marine Laboratory
P.O. Box 223
Moss Landing, CA 95039 | 1 |
| 16. | R.M. Iverson
P.O. Box 9008
Silver Spring, MD 20916 | 1 |
| 17. | Dr. Garry Mardell, Director, GOES
P.O. Box 740010
6100 Hillcroft (77081)
Houston, TX 77274 | 1 |
| 18. | Mr. Leigh Barnes
Marconi Radar Systems
Writtle Road, Chelmsford
Essex CM1 3BN
UNITED KINGDOM | 1 |